

# **DIVERSE SUBCELLULAR DISTRIBUTION PATTERNS OF PROTEINS AND THEIR FUNCTIONAL CONSEQUENCES AT MULTIPLE SPATIAL SCALES**

**Ph.D. thesis**

**Miklós Szoboszlay**

János Szentágothai Doctoral School of Neurosciences  
Semmelweis University



Supervisor: Zoltán Nusser DVM, DSc

Official reviewers:

Gergő Orbán, PhD

Gábor Petheő, MD, PhD

Head of the Final Examination Committee:

Miklós Geiszt MD, DSc

Members of the Final Examination Committee:

Csaba Barta MD, PhD

Zsolt Borhegyi PhD

Budapest, 2018

1 LIST OF ABBREVIATIONS .....	3
2 INTRODUCTION .....	7
2.1 General introduction.....	7
2.2 Hippocampus.....	8
2.3 Cerebellum .....	10
2.4 Multi-compartmental modelling .....	12
2.5 Pattern recognition techniques for spatial point patterns .....	15
3 OBJECTIVES.....	16
4 METHODS.....	17
4.1 Electrophysiology and two-photon imaging of cerebellar GoCs.....	17
4.2 Neurolucida reconstructions of GoCs and correlated EM .....	18
4.3 Computer simulations for cerebellar GoCs.....	18
4.4 Electrophysiology of hippocampal CA1 pyramidal neurons.....	20
4.5 Neurolucida reconstructions of CA1 pyramidal cells .....	21
4.6 Computer simulations for hippocampal CA1 pyramidal cells.....	22
4.7 Data analysis and visualization .....	22
4.8 Software for 2D spatial quantifications.....	22
4.9 Modelling and data analysis of spatial point patterns .....	23
4.10 Clustering of spatial point patterns.....	24
4.11 Statistical tests.....	26
5 RESULTS.....	27
5.1 Subcellular HCN and leak conductance distribution in hippocampal CA1 pyramidal cells.....	27
5.1.1 Technical outlook: dual somatic recordings to measure the impact of accurate pipette capacitance neutralization and bridge balance compensation.....	27
5.1.2 Dendritic nonuniformities of CA1 PCs.....	30
5.1.3 Stability of dendritic recordings.....	33
5.1.4 Rendering the dendritic cell membrane of CA1 PCs passive .....	34
5.1.5 Morphological reconstruction of recorded cells and identification of pipette location.....	36
5.1.6 Modelling <i>in vitro</i> recorded $V_m$ responses of individual CA1 PCs .....	37
5.1.7 Simultaneous fitting of $V_m$ responses of all recorded cells.....	39
5.2 Functional properties of dendritic gap junctions in cerebellar Golgi cells .....	42
5.2.1 Characterization of passive electrical properties of GoC dendrites .....	42

5.2.2 $C_m$ measurements of GoCs.....	45
5.2.3 Determining $R_a$ of GoC dendrites .....	47
5.2.4 Estimation of GJ plaque conductance by modelling GoC pairs embedded within an electrically interconnected syncytium.....	49
5.2.5 Factors contributing to the variability in the strength of electrical coupling between cerebellar GoCs.....	52
5.3 Objective quantification of nanoscale protein distribution patterns .....	54
5.3.1 Comparing different measures for distinguishing clustered patterns from random distributions.....	54
5.3.2 Performance of ACF and NND measures on uniform patterns .....	60
5.3.3 Performance evaluation of clustering algorithms.....	62
5.3.4 Clustering of localization point patterns .....	64
6 DISCUSSION.....	67
7 CONCLUSIONS .....	70
8 SUMMARY.....	71
9 ÖSSZEFOGLALÓ .....	72
10 BIBLIOGRAPHY .....	73
11 BIBLIOGRAPHY OF CANDIDATE'S PUBLICATIONS.....	79
12 ACKNOWLEDGEMENTS.....	80

## 1 LIST OF ABBREVIATIONS

4-AP – 4-aminopyridine

ACF – spatial autocorrelation function

ACSF – artificial cerebrospinal fluid

AHP – spike after-hyperpolarization

AMPA –  $\alpha$ -amino-3-hydroxy-5-methyl-4-isoxazolepropionic acid receptor

AP – affinity propagation clustering algorithm

ARS – adjusted Rand score

AZ – active zone

BB – bridge balance

BC – cerebellar basket cell (1)

BC – Bayesian clustering algorithm (2)

CA – cornu ammonis

CC – coupling coefficient

CF – climbing fibres of the cerebellum

$C_m$  – specific membrane resistance

CNS – central nervous system

$C_p$  – pipette capacitance

CV – coefficient of variation

CVODE – variable time step integration method

Cx36 – connexin 36

D-AP5 – D(-)-2-Amino-5-phosphonopentanoic acid

DAB – 3,3'-diaminobenzidine

DB – DBSCAN clustering algorithm

DCN – deep cerebellar nuclei

DG – dentate gyrus

EC – entorhinal cortex

$E_h$  – reversal potential of the HCN channels

$E_{leak}$  – reversal potential of the leak channels

EM – electron microscope

FFT – fast Fourier transform

$FFT^{-1}$  – inverse fast Fourier transform

GABA –  $\gamma$ -aminobutyric acid

GCL – granule cell layer of the cerebellum

GENESIS – GEneral NEural SIMulation System

$G_h$  – HCN channel conductance

$G_{leak}$  – leak conductance

$G_{GJ}$  – gap junctional conductance

GJ – gap junction

GoC – Golgi cell

GrC – cerebellar granule cell

GUI – graphical user interface

HCN – hyperpolarization-activated cyclic nucleotide-gated channel

I – binarized image

IN – interneuron

IO – inferior olivary nucleus of the cerebellum

IR-DIC – infrared differential interference contrast

L2/3 – cortical layer 2/3

L5 – cortical layer 5

LM – light microscope

M – binarized mask image

ML – molecular layer of the cerebellum

MS – mean shift clustering algorithm

NA – numerical aperture

NMDA – *N*-methyl-D-aspartate

NND – nearest neighbour distance

PB – phosphate buffer

PC – pyramidal cell

PCL – Purkinje cell layer of the cerebellum

PF – parallel fibres of the cerebellum

PP – perforant path of the hippocampus

$P_r$  – vesicular release probability

PSD – postsynaptic density

$R_a$  – axial or intracellular resistance

$R_{\text{access}}$  – access resistance of the patch pipette

$R_{\text{in}}$  – input resistance of the cell

$R_m$  – specific membrane resistance

$R_{\text{tip}}$  – tip resistance of the patch pipette

S – subiculum

SC – Schäffer collaterals of the hippocampus

SD – standard deviation

SDP – structure delineating polygon

SDS-FRL – SDS-digested freeze-fracture replica immunolabeling

SLM – stratum lacunosum-moleculare of the hippocampus

SO – stratum oriens of the hippocampus

SP – stratum pyramidale of the hippocampus

SR – stratum radiatum of the hippocampus

TTX – tetrodotoxin

VGCC – voltage-gated  $\text{Ca}^{2+}$  channels

$V_{\text{half}}$  – half activation voltage of voltage-gated ion channels

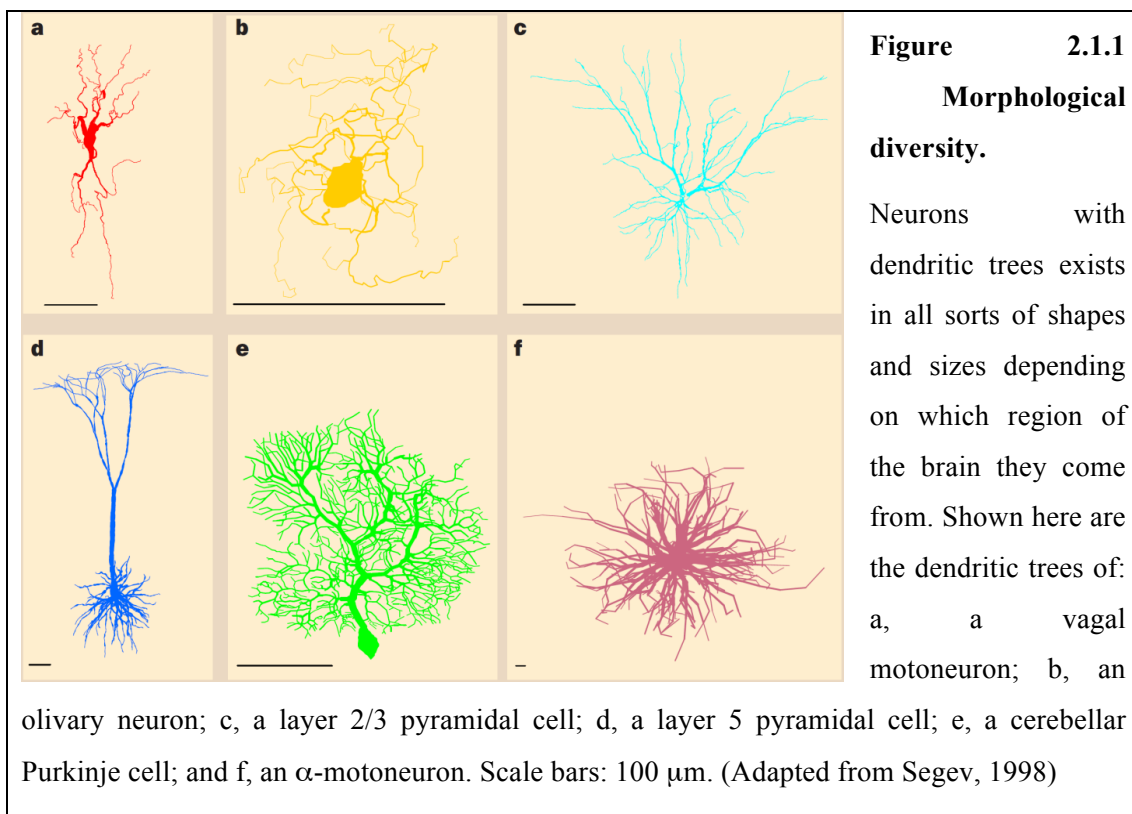
$V_m$  – membrane potential

WC – whole cell patch clamp configuration

## 2 INTRODUCTION

### 2.1 General introduction

The diversity of neurons in the central nervous system (CNS) originates from their distinct morphological build-up (the number, length and complexity of their dendrites and axon; Figure 2.1.1), the heterogeneity of voltage- and ligand-gated ion channels expressed in their cell membranes with different subcellular axo-somato-dendritic distributions (Golding et al., 2005; Kerti et al., 2012; Kirizis et al., 2014; Hu and Jonas, 2014) as well as their passive electrical properties. This diversity leads to substantial differences in the information processing capabilities of the distinct cell populations. Another level of complexity is introduced by the broad variety of synaptic plasticity mechanisms. At the nanoscale level, synaptic plasticity can be manifested by a spatial reorganization of synaptic proteins (Tang et al., 2016; Pennacchietti et al., 2017). For example, distribution of voltage-gated  $\text{Ca}^{2+}$  channels (VGCC) governing  $\text{Ca}^{2+}$  influx necessary for presynaptic vesicle fusion and their spatial arrangement in relation to the docked synaptic vesicles within the active zone (AZ) critically affects vesicular release probability ( $P_r$ ; Eggermann et al., 2012).



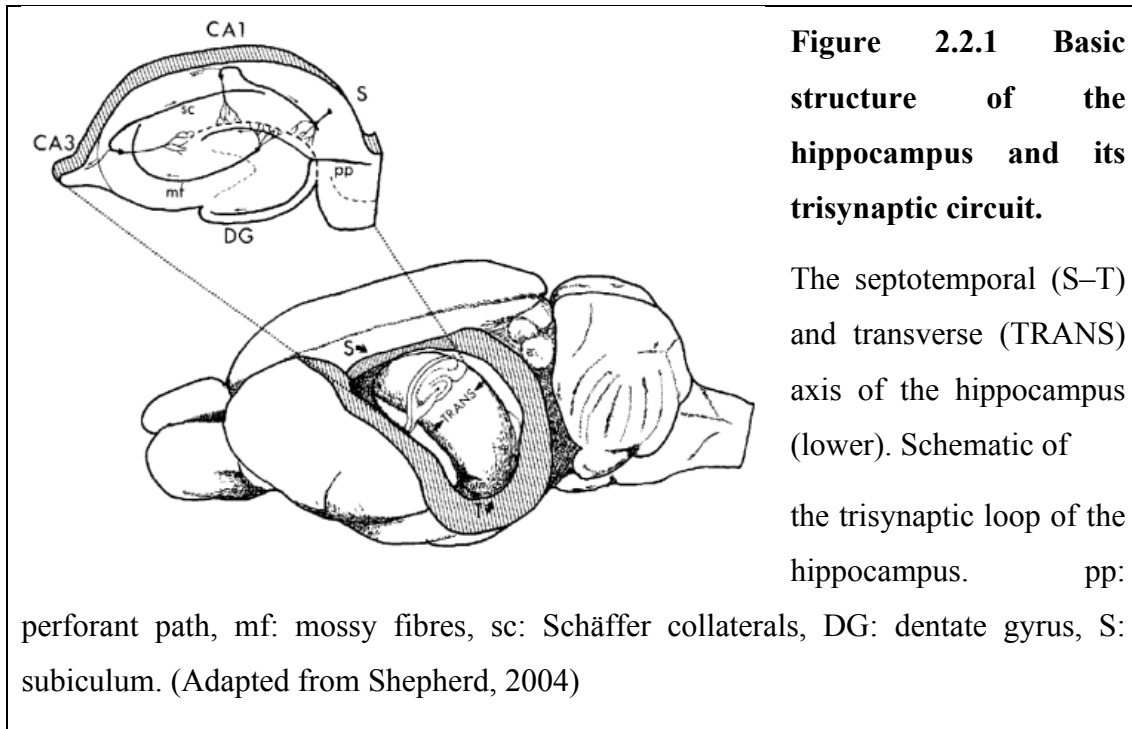


These features of the CNS inspired my doctoral work and prompted me to investigate the diverse protein distributions governing information processing both at subcellular and subsynaptic spatial scales with a combination of experimental and computational tools. First, I aimed to develop a combined method to determine subcellular distributions of various voltage- or ligand-gated ion channels in hippocampal CA1 pyramidal cells (PC; Section 5.1). I continued with uncovering functional properties of dendritic gap junctions in cerebellar Golgi cells (GoC; Section 5.2). The final project of my Ph.D. studies focused on pattern recognition techniques that can quantify nanoscale protein distributions in an objective manner (Section 5.3).

## **2.2 Hippocampus**

The hippocampus is an archecortical structure located in the temporal lobe of the brain (Figure 2.2.1). Its laminated and quite simple organization made it ideal to investigate both cellular and network functions, therefore the hippocampus has become one of the most intensely studied region of the mammalian CNS. The hippocampal formation has several parts: the dentate gyrus (DG), the three cornu ammonis (CA) subregions (CA1, CA2, CA3), the subiculum (S), the presubiculum, the parasubiculum and the entorhinal cortex (EC).

The laminar organization of the hippocampal formation is most apparent in the CA regions, with stereotypical, functionally well-segregated layers, historically termed strata. All CA subregions of the hippocampus include a cellular layer, where the cell bodies of most pyramidal cells are located (stratum pyramidale, SP). These are excitatory, glutamatergic principal cells with their apical dendritic trees spreading towards the DG, through the mostly acellular layers of strata radiatum (SR) and lacunosum-moleculare (SLM). The CA3 region also houses a unique layer, the stratum lucidum between SP and SR. Finally, the tip of the basal dendritic tree of the PCs delineates the stratum oriens (SO).



The basic synaptic circuit of the hippocampus is the trisynaptic loop (Andersen et al., 1971). Information arrives at the DG from layer II of the EC (through perforant path axons). In turn, axons of the DG granule cells (mossy fibres) excite hippocampal CA3 PCs. These neurons send their axons (Schäffer collaterals; SC) to CA1 PCs, which is considered the main output node of the hippocampus, projecting back to the EC. Although this is the main route of information flow through the hippocampus, there are other synaptic connections assisting network functions, such as auto-associative CA3 PC – CA3 PC synapses, supporting pattern completion (Guzman et al., 2016). Besides the excitatory pyramidal cells of the CA subregions there are various types of local, inhibitory, mostly  $\gamma$ -aminobutyric acid (GABA) secreting interneurons (IN; Freund and Buzsáki, 1996) controlling local excitation-inhibition ratio for proper functioning of the hippocampus. These cells are located mostly in the acellular layers (SO, SR, SLM) of the CA subregions.

Originating from its wiring properties and the autoassociative connections in multiple subregions, the hippocampus is highly vulnerable to excessive excitation if the inhibitory INs are malfunctioning, leading to epileptic seizures. The surgical removal of epileptic tissue shed light on the fact that the hippocampus also has a significant role in

memory formation (the case of the famous patient H. M.). Additionally, certain cells' spiking activity is influenced by the animal's spatial position (reviewed by Buzsáki and Moser, 2013).

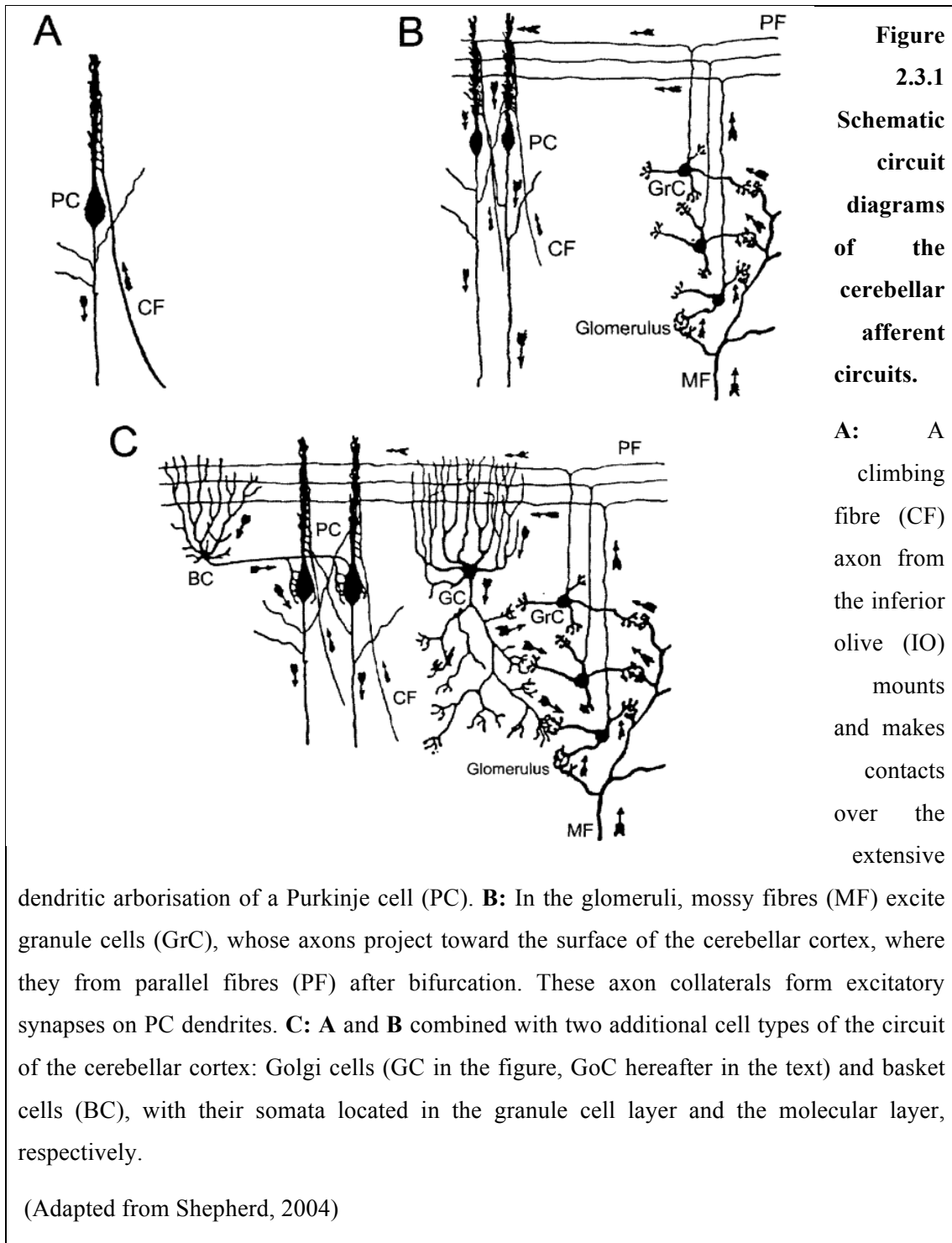
The CA1 subregion's PCs are ideally positioned and structured to study both subcellular ion channel distributions along their dendritic trees, given their tightly organized layout and reasonably thick apical trunk dendrites, and their dendritic integrative properties. Taking advantage of these properties of CA1 PCs, both anatomical (Lőrincz et al., 2002; Lőrincz and Nusser, 2010; Kerti et al., 2012; Kirizis et al., 2014) and electrophysiological (Magee and Johnston, 1995; Hoffman et al., 1997; Magee, 1998) investigations were carried out in order to determine subcellular distributions of distinct ion channels expressed in the cell membrane of these neurons. However, when direct measurements are not available for certain reasons (e.g. thin oblique dendrites for patch-clamp recordings, or lack of specific antibody for a given ion channel subunit), a combination of a technical arsenal could be used to tackle the problem (e.g. Golding et al., 2005).

This was my motivation to develop a framework able to determine subcellular distribution of different ion channels with *in vitro* dendritic patch-clamp recordings combined with pharmacological manipulations, morphological reconstruction of the recorded neurons and *in silico* computational modelling of the recorded membrane potential ( $V_m$ ) responses in order to shed light on the previously inaccessible details of ion channel distributions of CA1 pyramidal neurons.

## **2.3 Cerebellum**

The cerebellum is evolutionarily one of the most conserved structures of the brain. Its basic functional design supports the interaction between the cerebellar cortex and deep cerebellar nuclei (DCN). The cerebellar cortex receives afferent inputs from two sources, the climbing fibres and the mossy fibres, while its single output is the axons of Purkinje cells (Figure 2.3.1). Purkinje cells are organized into a single cellular layer (Purkinje cell layer, PCL), while the cerebellar cortex has two additional layers: the molecular layer (ML) is located peripheral to the PCL and the layer towards the

white matter is the granule cell layer (GCL). The DCN also receive collaterals from climbing and mossy fibres (Shinoda et al., 1992), as well as the Purkinje cells.



Besides chemical synapses (Figure 2.3.1), electrical synapses (gap junctions; GJ) are also present between GABAergic INs of the cerebellar cortex (Sotelo and

Llinás, 1972; Mann-Metzer and Yarom, 1999; Dugué et al., 2009; Alcamí and Marty, 2013). This connection between Golgi cells (GoC) is mediated by connexin36 (Cx36; Vervaeke et al., 2010) and shows large heterogeneity (Vervaeke et al., 2010). This variability of electrical synaptic connections between GABAergic INs are key determinants of spike desynchronization within the neuronal networks.

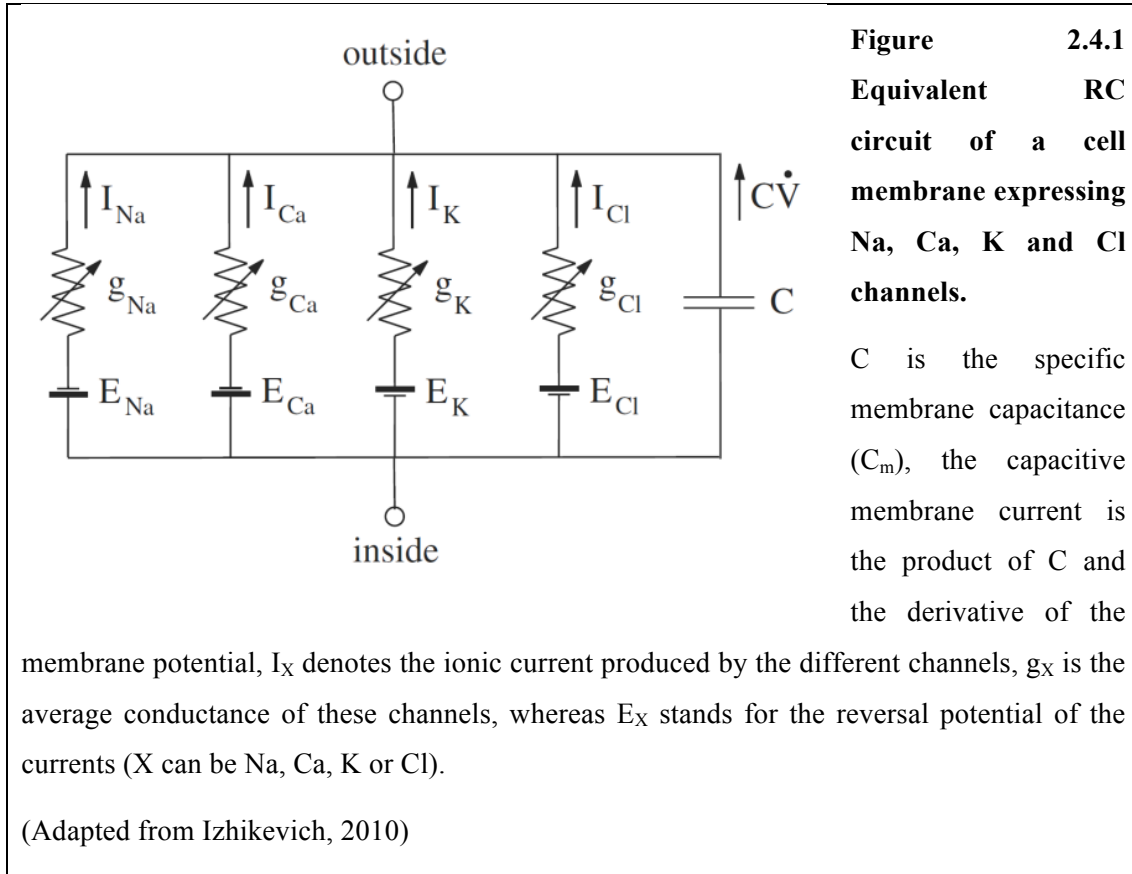
It has previously been demonstrated that slow inhibitory potentials after spikes (afterhyperpolarization, AHP) can more effectively spread among gap junction-coupled cells due to their lower frequency (Vervaeke et al., 2010). These inhibitory potentials can either synchronize or desynchronize GoC networks, depending on the timing of synaptic excitation in relation to the phase of the ongoing oscillation (Vervaeke et al., 2010). We therefore focused on determining the key factors regulating the strength of electrical coupling between cerebellar GoCs. We also aimed to quantify the functional properties of GJs and determine the contribution of passive dendritic properties to the coupling strength. We addressed these with a combination of *in vitro* dual somatodendritic and paired somatic patch-clamp recordings, light microscopic (LM) reconstruction of the recorded cells and electron microscopic (EM) quantification of the number and location of GJs together with multi-compartmental modelling to reveal the conductance of GJs ( $G_{GJ}$ ).

## 2.4 Multi-compartmental modelling

*In silico* multi-compartmental modelling is a side branch of computational neuroscience. It is considered a useful complementary field of experimental neuroscience. Its practicality becomes increasingly conspicuous in cases when the experimental tools are not available to measure a given quantity or the experimental arrangement would be extremely hard to accomplish (e.g. simultaneous patch-clamp recordings from multiple dendritic or axonal regions).

There are a couple of multi-compartmental modelling simulation environments available, the most popular ones being NEURON (Carnevale and Hines, 2006) and GENESIS (GEneral NEural SIMulation System; Bower and Beeman, 1994). Both of these simulators are based on cable theory (Rall, 1959), i.e. they build the morphology of a neuron from a set of cables, which are divided to equipotential, small compartments

and model the cell membrane as an equivalent RC circuit, having a specific membrane resistance ( $R_m$ ) and specific membrane capacitance ( $C_m$ ). The intracellular or axial resistance ( $R_a$ ), which connects the equivalent RC circuits of the sequential compartments in the model, and the  $R_m$  of the cell jointly determine the attenuation of the voltage flowing along the cables. These three parameters are the passive electrical properties of the neuron.



However, real neurons often have a plethora of ligand- and voltage-gated ion channels (e.g.  $\text{Na}^+$ ,  $\text{K}^+$ ,  $\text{Ca}^{2+}$  or  $\text{Cl}^-$  channels) expressed in their cell membranes. For such case, the equivalent RC circuit of a compartment looks like the one depicted in Figure 2.4.1. The total current flowing through a given part of the cell membrane,  $I$ , is equal to the sum of capacitive and ionic currents:

$$I = C_m \frac{dV}{dt} + I_{Na} + I_{Ca} + I_K + I_{Cl} \quad (2.1).$$

The traditional form of this equation is the following:

$$C_m \frac{dV}{dt} = I - I_{Na} - I_{Ca} - I_K - I_{Cl} \quad (2.2).$$

For any ionic currents,  $I_X$  is calculated by

$$I_X = g_X(V - E_X) \quad (2.3),$$

where  $g_X$  is the conductance of the ionic channel (which could be constant (leak conductance) or voltage dependent (e.g.  $g_{Na}$ ,  $g_{Ca}$ ,  $g_K$ , etc.)),  $V$  is the membrane potential and  $E_X$  is the reversal (or Nernst equilibrium) potential of the ion  $X$ . This equation is complicated further if there are other currents present in the model (which is often the case during realistic simulations), e.g. synaptic currents, currents injected via a patch-clamp electrode, or in classes of spatially expanded neurons (e.g. cortical L5 or hippocampal CA1 pyramidal neurons, cerebellar Purkinje cells), the contribution of the axial current can be substantial as well. Given the cable-like structure of dendritic and axonal processes, the partial differential equation to be solved to calculate  $V(x, t)$  (which depends on both space and time) for such spatially extended neurons is called the cable equation, which has the following form (Dayan and Abbott, 2001):

$$C_m \frac{\partial V}{\partial t} = -\frac{1}{2rR_a} \frac{\partial}{\partial x} \left( r^2 \frac{\partial V}{\partial x} \right) - i_m + i_e \quad (2.4),$$

where  $r$  is the radius of the compartment,  $i_e$  is the electrode current injected into the compartment and  $i_m$  is the current per unit area of the membrane.

These simple models on their own can provide useful insights about basic conceptual questions, e.g. how signal attenuation is manifested along different dendritic branches before reaching the cell body of the neuron where they are integrated or how the different passive electrical parameter triplets influence the signal attenuation along a single cable (dendrite). However, models have to be sufficiently well constrained in order to be able to give realistic, biologically plausible predictions. To achieve this, thorough experimental work is needed to fine-tune multi-compartmental models on relevant, sufficiently rich and well-controlled biological data. To this end, I carefully designed and performed *in vitro* patch-clamp recordings in passive conditions in order to achieve highest possible quality of experimental data with the aim of having a reasonably accurate model description of data with fewest possible model variables.

## 2.5 Pattern recognition techniques for spatial point patterns

Chemical synapses of the central nervous system substantially differ in their structural, molecular and functional properties (O'Rourke et al., 2012; Atwood and Karunanithi, 2002). Robust diversity is apparent among synapses made by distinct pre- and postsynaptic cell types, which is likely to be the consequence of their distinct molecular makeups. Remarkable functional diversity is also found among synapses made by molecularly and morphologically homogeneous pre- and postsynaptic cells (e.g. hippocampal CA3 PCs on CA1 PCs; Dobrunz and Stevens, 1997; Shepherd and Harris, 1998). A plausible explanation for this is that different numbers, densities or distinct nanoscale distributions of the same molecules underlie the functional diversity among these synapses. Moreover, it has been shown that the spatial arrangement of VGCCs and their relation to the  $\text{Ca}^{2+}$  sensors has substantial influence over the probability with which synaptic vesicles are released (Eggermann et al., 2012). It is therefore of great importance to determine the underlying distribution patterns of the synaptic proteins (i.e. whether it is random, uniform or clustered). Numerous ways of analysing spatial point patterns have been introduced recently (Baddeley and Turner, 2005; Jones et al., 2008; Veatch et al., 2012; Levet et al., 2015; Li et al., 2016), however, comparison of their data-dependent efficiency is not complete.

In order to test such metrics at sample sizes relevant to sub-AZ spatial scales (i.e. in the range of  $10^1$ – $10^2$  number of localization points), I implemented simple, distance-based and more complex measures (spatial autocorrelation function, ACF; Veatch et al., 2012) to quantify the nanoscale distribution of proteins. I probed the implemented measures on simulated datasets covering the localization point density range of experimental data ( $100$ – $1000 \mu\text{m}^{-2}$ ) to find the best performing ones that can be used to quantify the experimental data.



### **3 OBJECTIVES**

**3.1** Develop and validate a combined methodological approach to determine subcellular ion channel distributions of neurons. I used *in vitro* dendritic patch-clamp recordings from acute brain slices of male Wistar rats, morphological reconstruction of the recorded cells and *in silico* multi-compartmental modelling of the recorded  $V_m$  changes. To validate this combined approach, I aimed to replicate the known subcellular distribution of hyperpolarization-activated cyclic nucleotide-gated (HCN) ion channels in hippocampal CA1 pyramidal neurons.

**3.2** Determine the contributions of dendritic and gap junctional filtering to signal processing in electrically coupled cerebellar Golgi cell networks and the factors that diversify the strength of electrical coupling between these inhibitory interneurons.

**3.3** Find and implement methods that are able to quantify the distribution patterns of distinct pre- and postsynaptic proteins.

#### **Contributions**

The second project (section 5.2) was a joint effort of Dr Andrea Lőrincz (LM and EM experiments), Dr Frederic Lanore (*in vitro* electrophysiology) and myself. Dr Tekla Kirizs contributed to the experimental and to the explorative part (by drawing complex-shaped clusters) of the third project (section 5.3). She also performed a subset of the statistical tests.

## 4 METHODS

### 4.1 Electrophysiology and two-photon imaging of cerebellar GoCs

Sagittal slices (230  $\mu\text{m}$ ) of the cerebellar vermis were prepared from both male and female P23 – P29 C57BL/6 mice in accordance with UK Home Office guidelines. Slices were prepared in a solution containing (in mM) 2.5 KCl, 4 MgCl<sub>2</sub>, 0.5 CaCl<sub>2</sub>, 1.25 NaH<sub>2</sub>PO<sub>4</sub>, 24 NaHCO<sub>3</sub>, 25 glucose, 230 sucrose, bubbled with 95% O<sub>2</sub> and 5% CO<sub>2</sub>. Recordings were made at 32–36 °C from cerebellar slices perfused in ACSF containing (in mM) 125 NaCl, 2.5 KCl, 2 CaCl<sub>2</sub>, 1 MgCl<sub>2</sub>, 1.25 NaH<sub>2</sub>PO<sub>4</sub>, 26 NaHCO<sub>3</sub>, and 25 glucose, 0.001 TTX, 0.01 D-AP5, 0.01 NBQX, 0.01 SR95531, 0.0005 Strychnine, 0.01 ZD7288, 0.1 Ba<sup>2+</sup>, and in a subset of experiments, additional 0.01 4-AP and 0.025 mefloquine; pH = 7.3, equilibrated with 5% CO<sub>2</sub> and 95% O<sub>2</sub>. Data were recorded using the Neuromatic software ([www.neuromatic.thinkrandom.com](http://www.neuromatic.thinkrandom.com), written in IGOR, Wavemetrics) and analysed using Neuromatic and OriginPro (OriginLab). Membrane potentials are specified without correction for the liquid junction potential. Two-photon imaging was performed with a microscope consisting of a Mai-Tai laser (Spectra-Physics, tuned to 880 nm), a galvanometer-based scanhead (Ultima, Prairie technologies) and an Olympus BX51 microscope with a 60x water immersion objective (NA = 1). For two-photon targeted patching, GoCs were filled with 50  $\mu\text{M}$  Alexa594 (Invitrogen, Carlsbad, CA) through a somatic patch pipette containing (in mM) 120 K-gluconate, 20 KCl, 2 MgCl<sub>2</sub>, 10 EGTA, 10 HEPES and 2 ATP-Na<sub>2</sub>, titrated to pH = 7.3 with KOH, with 6 mM biocytin. A second patch pipette without Alexa594 and biocytin was used to patch one of the dendrites with the aid of an online overlay of the Ddtd contrast and the fluorescence images (Nevian et al., 2007). Pipettes were pulled from thick walled (outer diam.: 1.5 mm, inner diam.: 0.75 mm) borosilicate glass capillaries (Sutter Instruments) and had a resistance of 3–6 M $\Omega$  for somatic recordings and 9–20 M $\Omega$  for dendritic recordings. To minimize pipette capacitance, tips of the dendritic patch pipettes were coated with wax and the bath level was kept as low as possible. The access resistance ( $R_{\text{access}}$ ) was  $15 \pm 5$  M $\Omega$  for somatic and  $67 \pm 32$  M $\Omega$  for dendritic recordings. Pipette capacitance compensation and bridge-balance were applied and adjusted, when necessary, during the experiments. The  $R_{\text{in}}$  at the soma and the steady-

state voltage attenuation along the dendrites were measured by injecting 400 ms long hyperpolarizing current pulses of 50 pA (under control conditions) or 20 pA (in mefloquine). Voltage signals were recorded using a MultiClamp 700B amplifier (Molecular Devices), low-pass filtered at 10 kHz, digitized at 20–40 kHz. *All of these measurements were performed by Dr Frederic Lanore in Prof. Angus Silver's laboratory at University College London, London, UK.*

#### **4.2 NeuroLucida reconstructions of GoCs and correlated EM**

Slices containing recorded cells were placed in a fixative containing 4% paraformaldehyde and 1.25% glutaraldehyde in 0.1 M phosphate buffer (PB; pH=7.4). Slices were then cryoprotected in 10% and 20% sucrose solutions (in 0.1 M PB) for 45 min followed by rapid freezing and thawing in 0.1 M PB. After several washes in PB, slices were embedded in 1% agarose and re-sectioned at 60  $\mu\text{m}$  thickness. Biocytin was visualized using avidin–biotin–horseradish peroxidase complex and a diaminobenzidine reaction. Sections were then dehydrated and embedded in epoxy resin (Durcupan). Three-dimensional LM reconstructions of the cells were performed with the NeuroLucida system (MicroBrightField, Williston, VT) using a 100x oil-immersion objective (numerical aperture (NA) = 1.4). Light micrographs of each close apposition were used for guiding the EM identification of the GJs. Serial sections of 70 nm thickness were cut with an ultramicrotome. All close appositions between the filled dendrites were checked in the EM (Tamás et al., 2000; Vervaeke et al., 2010). *The EM investigations and a subset of the NeuroLucida reconstructions of GoCs were performed by Dr Andrea Lőrincz.*

#### **4.3 Computer simulations for cerebellar GoCs**

GoCs were filled with biocytin during the electrophysiological experiments through the recording pipette, and visualized later by a DAB reaction for detailed morphological reconstruction using the NeuroLucida software. GoC models were constructed in either neuroConstruct (Gleeson et al., 2007) or NEURON (Carnevale and Hines, 2006) and simulations were run in NEURON (version 7.3).

To determine the specific axial resistance ( $R_a$ ) of the cells, dual somato-dendritic recordings were performed from  $n = 29$  cells (15 control and 14 in mefloquine), of which 5 recorded cells from each condition were reconstructed and their morphologies were imported into NEURON. Since these GoCs fulfilled our criteria of passiveness (i.e. their current injection-evoked  $V_m$  responses were linear and symmetric), only a leak conductance was inserted into all of the compartments with a uniform density. Then the  $R_m$ ,  $R_a$  and  $C_m$  parameters of the cells were iterated simultaneously during the fitting procedure, to obtain the best fit to the somatic and dendritic current injection-evoked membrane voltage responses. Spatial discretization was applied as parameters changed according to the *d\_lambda* rule (Carnevale and Hines, 2006), with a value of 0.1. We used the voltage responses generated by somatic current injections because the electrode  $R_{\text{access}}$  was lower and pipette capacitance neutralization as well as bridge balance compensation was less prone to error than for the dendritic recordings. However, somatic voltage responses to dendritic current injections were used to cross-check the parameters obtained from the best fit to somatic current injections (Figure 5.2.2).

To determine how the distribution of GJs influences the estimate of  $R_a$ , we modelled the GoCs in syncytia (i.e. in electrically interconnected networks; Figure 5.2.4). The ‘central’ cell had 10 neighbouring cells, each coupled by 2 GJs (resulted in  $n = 20$  GJs) to the dedicated one. These GJs were randomly distributed on the dendritic tree of the neurons. We generated 10 of such random syncytia and then iterated the  $R_m$ ,  $C_m$  and  $R_a$  parameters on the somatic current injection-evoked somatic and dendritic membrane voltage responses. During the simulation, the average conductance of GJs ( $G_{GJ}$ ) was kept constant at 1 nS. The morphology of the cells was the same in each of the syncytia, as well as their passive electrical parameters.

To determine  $G_{GJ}$  based on our reconstructed GoC pairs ( $n = 4$ ), we followed the same strategy described above by inserting a leak conductance with a uniform density to all compartments of the neurons. Based on EM data, the exact locations of the GJs were set in the model with an accurate spatial discretization. First, we used the mean  $R_a$  value from our previous modelling and a  $C_m$  of  $1 \mu\text{F}/\text{cm}^2$  (a consensus value for biological membranes (Gentet et al., 2000; Larkum et al., 2009), and then fitted the  $R_m$  parameter of one of the GoCs of a pair to obtain the best fit to its own somatic current-evoked voltage response. Parallel with this, we fitted  $G_{GJ}$  on the coupled cell’s attenuated

voltage response. Then we moved on to the other cell and repeated the same procedure. As the changes in  $R_m$  from the initial values also influenced  $G_{GJ}$ , we iterated this process until the change in  $R_m$  and  $G_{GJ}$  was less than 5%. We determined  $G_{GJ}$  in both directions (from cell blue to red and red to blue) for the 4 cell pairs in 10 random syncytia ( $n = 80$ ). To explore the dependence of  $G_{GJ}$  on  $R_a$  as shown in Figure 5.2.6E, we followed the same fitting strategy described above fixing the  $R_a$  parameter of the cells at different values.

The fitting of the model to the experimental data was performed with NEURON's built-in Praxis fitting algorithm. Simulations were run on a desktop PC under Windows 7 using variable time step integration method 'CVODE'. Simulations used to estimate the variability in CC arising from the dendritic location, GJ number and GJ strength were performed with simulations of a cell pair. Syncytia were not used because they would have introduced additional variation depending on the specific configuration. For these simulations an  $R_m$  value of  $5 \text{ k}\Omega\cdot\text{cm}^2$  was chosen to match the average  $R_{in}$  of the modelled cells and the other passive properties were fixed at our measured values ( $R_a = 92 \text{ }\Omega\cdot\text{cm}$ ,  $C_m = 1 \text{ }\mu\text{F}/\text{cm}^2$ ). The CC was determined as the ratio of the post- and presynaptic steady-state voltage responses upon long current injections.

The GoC models with the electrophysiological data I used for parameter fitting could be found at ModelDB (accession number: 189186).

#### **4.4 Electrophysiology of hippocampal CA1 pyramidal neurons**

Horizontal slices (300  $\mu\text{m}$ ) of the ventral hippocampus were cut from male Wistar rats (16–22 days old). Rats were deeply anesthetized by isoflurane (Abbott Laboratories) and killed by decapitation, in accordance with the Hungarian Act of Animal Care and Experimentation (1998, XXVIII, section 243/1998) and with the ethical guidelines of the Institute of Experimental Medicine Protection of Research Subjects Committee. The brain was quickly removed and placed into an ice-cold cutting solution containing (in mM): sucrose, 205.2; KCl, 2.5;  $\text{NaHCO}_3$ , 26;  $\text{CaCl}_2$ , 0.5;  $\text{MgCl}_2$ , 5;  $\text{NaH}_2\text{PO}_4$ , 1.25; glucose, 10; saturated with 95%  $\text{O}_2$  and 5%  $\text{CO}_2$ . Hippocampal slices were prepared using a Leica vibratome (VT1200S; Leica Microsystems), incubated in submerged holding chamber in ACSF containing (in mM): NaCl, 126; KCl, 2.5;  $\text{NaHCO}_3$ , 26;  $\text{CaCl}_2$ , 2;  $\text{MgCl}_2$ , 2;  $\text{NaH}_2\text{PO}_4$ , 1.25; glucose, 10; saturated with 95%

O<sub>2</sub> and 5% CO<sub>2</sub> (pH = 7.2–7.4) at 34 °C that was then gradually cooled down to room temperature (~1 hour). Recordings were carried out in the same ACSF at 24 °C, slices were kept up to 5 hours in the holding and recording chambers.

Cells were visualized with a Nikon Eclipse FN-1 microscope using infrared differential interference contrast (IR-DIC) optics and a water immersion objective (40x, 0.8 NA, Nikon). Current clamp whole-cell recordings from the soma and apical dendrite of CA1 PCs were performed using a MultiClamp 700B amplifier (Molecular Devices). Traces were filtered at 10 kHz and digitized online at 50 kHz using a Digidata1440A interface (Molecular Devices). Patch pipettes were pulled (Zeitz Universal Puller; Zeitz-Instrumente Vertriebs or P-1000 Micropipette Puller, Sutter Instruments) from thick-walled borosilicate glass capillaries with an inner filament (1.5 mm outer diameter, 0.86 mm inner diameter; Sutter Instruments). Tip resistance was 4–7 MΩ for somatic and 8–14 MΩ for dendritic recordings when filled with intracellular solution containing 130 mM K-Gluconate, 5 mM KCl, 2 mM MgCl<sub>2</sub>, 0.05 mM EGTA, 10 mM HEPES, 2 mM NaATP, 1 mM NaGTP, 10 mM creatine phosphate titrated to pH = 7.3 with KOH, with 7 mM biocytin. Access resistance was < 15 MΩ for somatic and ≤ 62 MΩ for dendritic (range: 17–62 MΩ, average: 37 ± 13 MΩ, n = 22) recordings. CA1 PCs were held between –65 mV and –70 mV (baseline V<sub>m</sub>, without correction for the liquid junction potential), at both somatic and dendritic sites. For passive dendritic recordings, the standard ACSF contained additionally 3 mM kynurenic acid (Tocris), 20 μM SR95531, 50 μM Cd<sup>2+</sup>, 1 μM TTX (Tocris), 5 mM 4-AP (Tocris) and 40 μM ZD7288 (Tocris). All drugs were purchased from Sigma unless stated otherwise.

#### **4.5 NeuroLucida reconstructions of CA1 pyramidal cells**

The procedure was the same as detailed above for cerebellar GoCs except for the 3D light microscopic reconstructions of the CA1 PCs were performed with the NeuroLucida system (MicroBrightField, Williston, VT) using a 40x oil-immersion objective (NA = 1.3).

#### 4.6 Computer simulations for hippocampal CA1 pyramidal cells

CA1 PCs were filled with biocytin during the electrophysiological experiments through the recording pipette, and visualized by a DAB reaction for detailed morphological reconstruction using the NeuroLucida software. Multi-compartmental models were constructed in NEURON (Carnevale and Hines, 2006) and simulations were run in NEURON (version 7.4).

For fitting apical dendritic recordings of CA1 PCs individually, the  $R_a$  parameter was kept at  $150 \Omega \cdot \text{cm}$  (lower bound of the range determined by Golding et al., 2005), while the  $R_m$  and  $C_m$  parameters were iterated until NEURON's built-in Praxis fitting algorithm found the best fit of the experimental data. For simultaneous fitting of  $n = 6$  apical dendritic recordings of CA1 pyramidal neurons, NEURON's MulRunFitter was used as in the individual case, but the summed error of all cells was used as a feedback for the fitting algorithm. Spatial discretization was applied as parameters changed according to the  $d\_lambda$  rule (Carnevale and Hines, 2006), with a value of 0.1. Simulations were run on a desktop PC under Windows 10 using variable time step integration method 'CVODE'.

#### 4.7 Data analysis and visualization

Analysis of *in vitro* electrophysiology data was performed with custom written Python scripts (version 2.7, 64-bit) using numpy, scipy and matplotlib.

#### 4.8 Software for 2D spatial quantifications

A software (GoldExt) was developed in Python (version 2.7, 64-bit), with which performed the generation of uniform and clustered patterns; their comparisons to random distributions; and cluster analysis were performed. GoldExt uses the following dependencies: numpy, scipy, matplotlib, scikit-learn (Pedregosa et al., 2011), xlswriter, openpyxl and PyQt4 (the latter for graphical user interface (GUI), which was drawn using Qt Designer). GoldExt is developed, tested and ran on 64-bit Windows environment (Windows 10). The software is available at <https://github.com/nusserlab/GoldExt>.

#### 4.9 Modelling and data analysis of spatial point patterns

Four types of models were generated for testing different measures. First, models with different densities of multiple clusters within the structure delineating polygon (SDP) were created. Localization points were randomly distributed within circular areas with radii randomly chosen between 25 and 75 nm. The density of the clusters was either  $30 \mu\text{m}^{-2}$  or  $60 \mu\text{m}^{-2}$ . The density of localization points was calculated for the whole SDP area (from  $100 \mu\text{m}^{-2}$  to  $600 \mu\text{m}^{-2}$  with an increment of  $100 \mu\text{m}^{-2}$ , and  $1000 \mu\text{m}^{-2}$ ) and not for the clusters. Two additional types of models were also implemented: ring- and T-shaped models. These shapes were hand-drawn within the SDPs and localization points were randomly placed within them. For the construction of uniform models, we first positioned localization points homogeneously on the nodes of a squared, triangular or hexagonal mesh. Then, we randomized the positions of all the localization points with a 2D Gaussian, having a covariance matrix  $[(12^2, 0) (0, 12^2)]$ . The values of the diagonal represent the experimentally constrained variance of the x and y coordinates (in nm, Lőrincz et al., 2002). All models were constructed as a Poisson hardcore process within the above-defined constraints having an inhibition radius of 10 nm (i.e. any two localization points cannot be closer to each other than 10 nm). We categorize the distribution of a point pattern clustered if it is neither random nor uniform.

The following four distance-based measures were implemented to compare experimental data or artificially generated distributions to random distributions: nearest neighbour distance, all-to-all distance, distance from the centre of gravity of localization points, distance from the nearest edge of the SDP. Once these values were calculated for every localization point, their mean was compared to the mean values of random distributions (200 random distributions per SDP). For individual SDP level comparisons, we considered a localization point distribution different from random, if the mean value of the artificially generated model data was smaller than the 2.5% or larger than the 97.5% of that of the random data (corresponding to 5% significance level). An error rate was calculated as the percentage of SDPs that were not found to be different from their corresponding random distributions.

An additional, more complex measure was also implemented. A spatial autocorrelation function (sometimes referred to as pair autocorrelation function or radial



distribution function),  $g(r)$ , was computed based on Veatch et al., 2012. Briefly, the image (I) was binarized (only the pixels which contain localization points become 1, every other pixel has a value of 0) and an image mask (M, which has pixel values of 1 inside the measurement area and is also padded by an equal number of zeros) was created for the different SDPs as the smallest rectangle containing the whole SDP. Since normally the AZ covers only a minor fraction of the whole image, the normalization constant  $d$ , which is the overall localization density of the image, was calculated within the mask area. Then the  $g(r)$  function was computed as follows:

$$g(r) = \frac{FFT^{-1}(|FFT(I)|^2)}{d^2 FFT^{-1}(|FFT(M)|^2)} \quad (4.1).$$

FFT stands for Fast Fourier Transform and  $FFT^{-1}$  for inverse Fast Fourier Transform. Because of the nature of the  $g(r)$  function, it has a value of 1 in case of random distributions (Veatch et al., 2012; Tang et al., 2016). In the present case, the area of M is slightly bigger than the SDP area, therefore the localization density  $d$  becomes a bit lower than the real density inside the SDP, consequently  $g(r)$  is slightly higher than 1 in case of the random distributions within the SDP. As all SDPs had slightly different shapes, and the ratios of the area of the SDP and the area of the smallest rectangle containing the whole SDP determines the degree of deviation from 1 in every case, the absolute value of the  $g(r)$  was not used. Since this deviation is equally present in both the data and its corresponding randomizations, once the  $g(r)$  functions were computed for the experimental or artificially modelled data and the random distributions, the average values were calculated within the first 80 nm and these averages were compared to each other as detailed above to assess statistical significance. In case of the population-wise comparisons, a simulated dataset was declared clustered or uniform, if its  $\overline{g(r)}$  values were significantly larger or smaller, respectively, than that of its corresponding randomizations.

#### 4.10 Clustering of spatial point patterns

Once a given set of experimental or artificially generated data was found to be statistically different from random, the number of clusters within the data was determined. Clustering was performed with a subset of clustering algorithms implemented in the scikit-learn site-package (Pedregosa et al., 2011) of Python. Three

algorithms were built into GoldExt, namely DBSCAN (DB, Ester et al., 1996), which is a density-based clustering algorithm, affinity propagation (AP, Frey and Dueck, 2007) and mean shift method (MS, Comaniciu and Meer, 2002). We also tested our modelled clustered distributions with a Bayesian clustering algorithm (BC; Rubin-Delanchy et al., 2015; Figure 5.3.6H and 5.3.7). As suggested in the original publication (Rubin-Delanchy et al., 2015; Figure S11a, b), parameters ‘ $\alpha$ ’ and ‘pbackground’ were set to 20 and 0.5, respectively. We also set an extra 200-200 nm from the edges of the investigated SDPs, which increased the adjusted Rand score (ARS; Hubert and Arabie, 1985) of the algorithm’s output (Figure 5.3.5). For BC, we used the original code provided by the authors, written in R, and ran it in Python using the rpy2 site-package. These algorithms were chosen because the user does not have to determine the number of desired clusters *a priori*.

To evaluate the performance of clustering algorithms on simulated datasets, we computed the ARS, implemented in the scikit-learn Python site package (Pedregosa et al., 2011). Briefly, adjusted Rand score is the Rand score (Rand, 1971) adjusted for chance. Given  $N$  points,  $X_1, X_2, \dots, X_n$ , and two clusterings of them,  $Y$  and  $Y'$ , with arbitrary number of clusters in each clustering and  $n_{ij}$  is the number of points simultaneously in the  $i$ th cluster of  $Y$  and the  $j$ th cluster of  $Y'$ . The similarity between  $Y$  and  $Y'$  is:

$$c(Y, Y') = \frac{\left[ \binom{N}{2} - \frac{1}{2} \left\{ \sum_i (\sum_j n_{ij})^2 + \sum_j (\sum_i n_{ij})^2 \right\} - \sum \sum n_{ij}^2 \right]}{\binom{N}{2}} \quad (4.2).$$

Rand score is 0 when the two clusterings have no similarities and 1.0 for identical clustering.

Out of these four clustering algorithms, DB outperformed the others when tested on the artificially generated multiple-cluster models (quantified by the ARS; Figure 5.3.5 – 5.3.7) with the following user-dependent parameters:  $\varepsilon = 50$  nm, which is the maximum distance between two localization points to be assigned to the same cluster and each cluster has to have at least 3 members (DB); a ‘preference’ value of -30 (AP); and a minimum number of cluster-assigned localization points of 3 (MS).

#### 4.11 Statistical tests

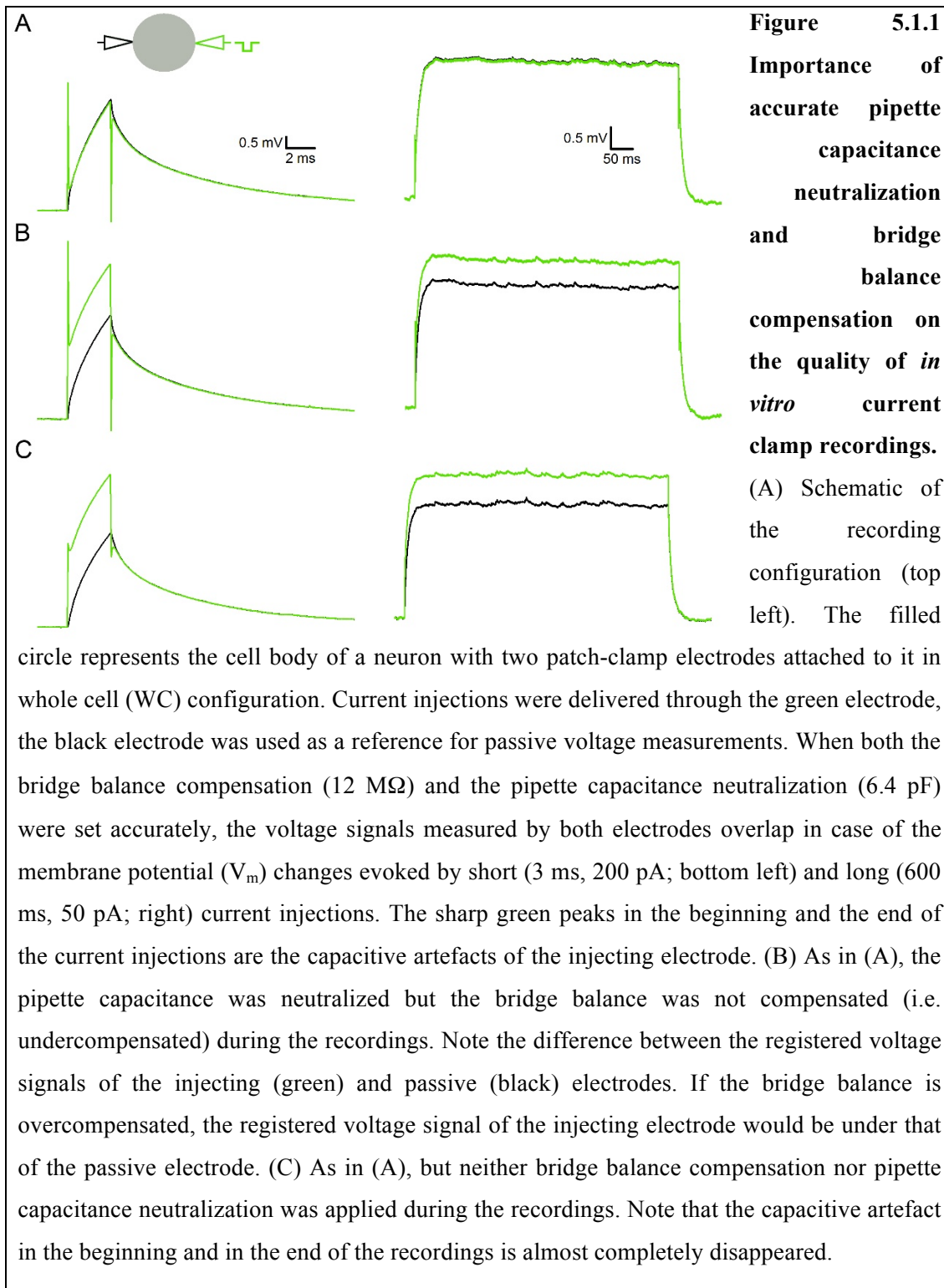
Statistical significance was either assessed with unpaired t test (Figure 5.2.3A) or the Wilcoxon signed-rank test (Figure 5.3.3B, 5.3.3D). For multiple comparisons, Kruskal-Wallis test was used, followed by Mann-Whitney U test with Bonferroni correction (Figure 5.3.3A, 5.3.3C and Figure 5.3.4D – 5.3.4F). Data are presented as mean  $\pm$  standard deviation (SD). *Dr. Tekla Kirizs performed a subset of statistical comparisons.*

## 5 RESULTS

### 5.1 Subcellular HCN and leak conductance distribution in hippocampal CA1 pyramidal cells

#### 5.1.1 Technical outlook: dual somatic recordings to measure the impact of accurate pipette capacitance neutralization and bridge balance compensation

The accuracy and limitations of any kind of techniques must be known in order to be able to precisely measure the quantity in question. It is always a significant introductory step in experimental work to have a good control over the precision of the applied technique. In *in vitro* patch-clamp electrophysiology, especially when the amplifier is in current clamp mode, robust measurement artefacts can be introduced when current is injected into the neuron held in whole-cell (WC) mode resulting from the injecting electrode's access resistance ( $R_{\text{access}}$ ) and capacitance ( $C_p$ ). It is therefore essential to apply accurate bridge balance (BB) compensation and  $C_p$  neutralization to eliminate measurement artefacts to a maximal possible extent. To this end, I thoroughly investigated how these parameters' settings influence the quality of the recordings with dual somatic patch-clamp recordings of hippocampal neurons (Figure 5.1.1). In this recording configuration, two electrodes were attached to the same cell body of the neuron in WC configuration: one is the current-injecting electrode, the other is the passive, reference electrode registering the 'true'  $V_m$  changes in the recorded neuron (Figure 5.1.1A). If the two signals are overlapping, the amplifier is tuned precisely and the measurement artefacts are minimal (Figure 5.1.1A).



I applied a stimulation protocol of short (3 ms, 200 pA) and long (600 ms, 50 pA) square current pulses to the cell and registered the resulting voltage changes at both the injecting (shown in green) and reference (black) electrodes. If both the BB

compensation and  $C_p$  neutralization parameters were set precisely (12 M $\Omega$  and 6.4 pF, respectively), the two registered signals were almost identical (Figure 5.1.1A). It is noteworthy that in the beginning and the end of the current injections, the injecting electrode's recorded signal has sharp, short duration peaks, which are produced by charging and subsequent discharging the  $C_p$ . If BB compensation is not applied on the recording electrode (i.e. it is set to 0 M $\Omega$ ), the amplitude of the recorded signal compared to the true voltage changes is increased (Figure 5.1.1B). This could lead to massively erroneous inferences about the recorded cell's physiological parameters (e.g. input resistance ( $R_{in}$ )). On the other hand, if the BB is overcompensated, the effect is the opposite: the recorded voltage signal is smaller than the 'true' voltage signal (data not shown). If neither the BB nor the  $C_p$  is set precisely (Figure 5.1.1C), the resulting voltage traces are similar to those shown in Figure 5.1.1B, but the rising and falling phases of the current injection-evoked voltage changes are slightly different (i.e.  $C_p$  neutralization-evoked sharp peaks are missing).

The importance of accurate BB compensation and  $C_p$  neutralization is even more pronounced when the recorded structure is small (e.g. subcellular compartments of neurons such as dendrites, axon terminals, axonal blebs, etc.). For such recordings, given the lower accessibility of the desired structure due to their smaller size, the tip diameter of the recording electrode has to be smaller than that of the traditional electrodes used to patch somatic compartments of neurons, consequently its tip resistance ( $R_{tip}$ ) is higher. Generally, dendritic recordings from neurons having different calibre dendrites (e.g. cerebellar Golgi cells having submicron-diameter dendrites compared to cortical L5 PCs with apical dendrites of  $\sim 2$   $\mu\text{m}$  in diameter) are performed with electrodes having  $R_{tip}$  between 7–18 M $\Omega$  (e.g. Stuart and Spruston, 1998; Magee, 1998; Roth and Häusser, 2001; Bittner et al., 2012; Sun et al., 2014; Delvendahl et al., 2015; Basu et al., 2016; Szoboszlay et al., 2016), but it could be as high as 40 – 50 M $\Omega$  (*in vitro* patch-clamp recordings from basal dendrites of cortical L5 pyramidal neurons; Nevian et al., 2007) while somatic electrodes are usually around 3–6 M $\Omega$ . The higher the  $R_{tip}$  of the electrode, the higher the  $R_{access}$  of the recording will be (ranging from 10 M $\Omega$  up to 200 M $\Omega$ ), therefore the introduced error by the injecting electrode can also increase drastically. Since patching a dendrite with two pipettes (injecting and reference) within isopotential distance is reasonably demanding (but see Williams and

Mitchell, 2008; Harnett et al., 2012), finding the appropriate experimental arrangement for the desired measurement is quintessential.

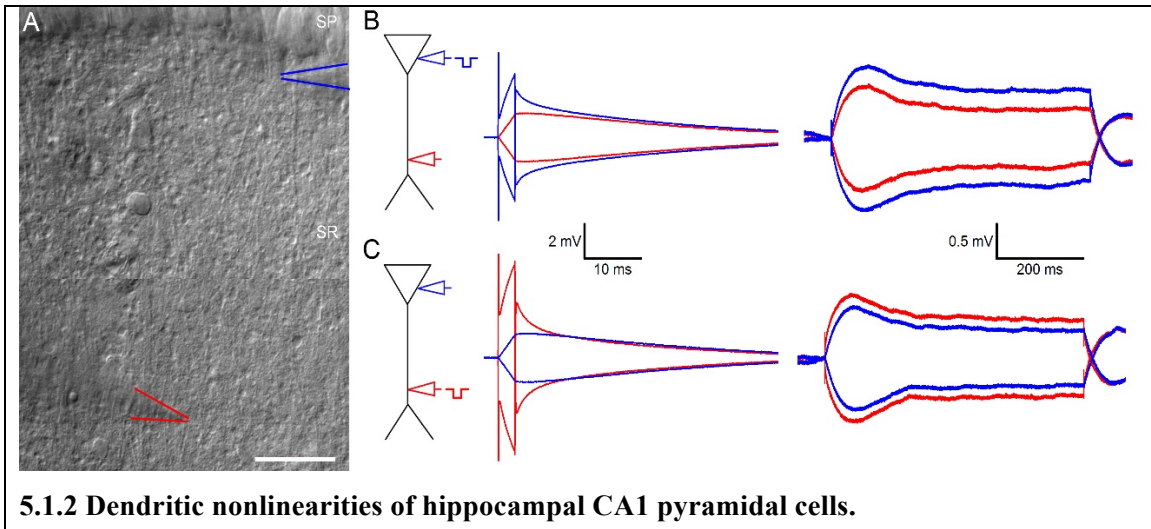
### 5.1.2 Dendritic nonuniformities of CA1 PCs

One of the most intensively studied cells in the CNS are the hippocampal CA1 PCs. Numerous studies investigated their subcellular ion channel distributions with either anatomical (Lőrincz et al., 2002; Lőrincz and Nusser, 2010; Kerti et al., 2012; Kirizs et al., 2014) or physiological (Magee and Johnston, 1995; Hoffman et al., 1997; Magee, 1998) methods, which contributed largely to the mechanistic understanding of main output node of the hippocampus at both cellular and network levels. Nonuniformities in dendritic ion channel distributions were uncovered by anatomical and physiological experiments, although their conclusions were sometimes different (e.g. Kerti et al., 2012 and Hoffman et al., 1997), indicating a further need of conceptual and technical refinements of such investigations.

Our idea was that instead of performing outside-outside patch-clamp recordings (like Hoffman et al., 1997: Kv4.2 (a subunit of the voltage-gated K<sup>+</sup> channel family); or Magee, 1998: HCN) or immunohistochemistry, to combine *in vitro* dendritic patch-clamp recordings with pharmacology, morphological reconstruction of the recorded neurons and computational modelling to reveal the subcellular distribution of ion channels. This multidisciplinary approach can be useful when the protein cannot be visualized with specific antibodies (e.g. leak K<sup>+</sup> channels) or when the investigated structure is too small for accurate patch-clamp measurements (e.g. oblique dendrites of CA1 PCs).

First, I performed dual soma-dendritic patch-clamp recordings from CA1 PCs in acute rat hippocampal slices to ensure that the nonuniformities observed in e.g. Magee, 1998 are present in my preparation as well (Figure 5.1.2). After selecting a seemingly healthy dendrite in the SR of the CA1 subregion of the hippocampus, which could be traced back to its somatic origin, the dendrite was patched (Figure 5.1.2A, red (Davie et al., 2006)), and WC configuration was obtained. A second pipette (Figure 5.1.2A, blue) was positioned either to the soma or to the origin of the apical dendritic trunk of the neuron (if the soma was inaccessible because of the tight arrangement of cell bodies of

PCs in SP). After establishing WC configuration at the somatic site as well, an alternating test pulse of 5 mV at 50 Hz (seal test) was applied at one electrode while the other was in ‘I = 0’ mode of the amplifier (passive electrode). If the attenuated version of the seal test signal could be detected at the passive electrode, both electrodes were attached to the same neuron (which was regularly not the case).



### 5.1.2 Dendritic nonlinearities of hippocampal CA1 pyramidal cells.

(A) Infrared differential interference contrast (IR-DIC) image of the hippocampal CA1 subregion of a P17 male Wistar rat. The blue lines highlight the somatic pipette at the apical dendritic trunk proximal to the somata of a CA1 pyramidal cell (PC) at the border of stratum pyramidale (SP) and stratum radiatum (SR), while the red lines represent the location of the dendritic pipette at  $\sim 200 \mu\text{m}$  from the cell body of the PC in the outer 2/3 of the SR. (B) Schematic of the experimental setup (left).  $V_m$  changes evoked by short (3 ms,  $\pm 200 \text{ pA}$ ; middle) and long (600 ms,  $\pm 10 \text{ pA}$ ; right) current injections delivered to the apical dendritic trunk of the neuron (blue traces). The propagated dendritic voltage signals were registered with the dendritic electrode (red traces). (C) The same stimulation protocol was applied through the dendritic electrode. Note that by injecting the same current into the dendrite, the evoked steady state voltage change (0.54 mV, red trace) is smaller than that of the soma at (0.69 mV, blue trace in (B)). Furthermore, the ratio of the propagated steady state voltage signal and the voltage change evoked locally at the injection site ( $\Delta V_{\text{propagated}}/\Delta V_{\text{local}}$ ) is larger in case of dendritic current injections ( $\Delta V_{\text{propagated}}/\Delta V_{\text{local}} = 0.74$ ) than when the current was injected into the cell body ( $\Delta V_{\text{propagated}}/\Delta V_{\text{local}} = 0.59$ ). These two observations are suggestive of a nonuniform dendritic conductance (either active or passive) distribution. The scale bar represents  $50 \mu\text{m}$  in (A).



After successfully establishing dual soma-dendritic patch-clamp recordings of a CA1 PC in WC configuration, short (3 ms,  $\pm 200$  pA) and long (600 ms,  $\pm 10$  pA) current injections were delivered to either the somatic (Figure 5.1.2B) or dendritic (Figure 5.1.2C) compartment of the cell and the  $V_m$  changes were monitored at both electrodes. Two signs of dendritic nonuniformities were observed at both somatic and dendritic  $V_m$  changes evoked by current injections at either site: (1) at the initial phase of the long pulse, a voltage dependent conductance is activated, which tries to repolarize the cell membrane to the resting  $V_m$ , resulting in a ‘sag’ potential (see also Figure 5.1.3) and (2) the asymmetric signal propagation of the long pulse in the centrifugal (soma-to-dendrite) and centripetal (dendrite-to-soma) directions. Uniform distribution of the total leak conductance (passive and active conductances together) of the cell membrane would have two consequences: (1) injecting a square pulse current with a given amplitude to a relatively small dendrite would result much larger  $V_m$  deflections than the same current would cause at the soma due to their different impedance profiles and (2) the centripetal signal attenuation would be more substantial than the centrifugal (see Figure 5.2.1C). I observed the contrary of these two aforementioned phenomena (in accordance with Magee, 1998), which suggested that nonuniformities are present in the dendritic cell membrane of CA1 PCs (London et al., 1999).

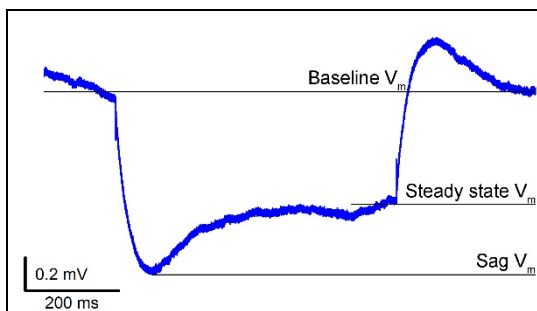


**Figure 5.1.3 Definition of sag ratio in current clamp recordings.** An example somatic current clamp recording of a hippocampal CA1 PC (the same as on Figure 5.1.2).

The sag ratio is defined as  $(\text{Sag } V_m - \text{Baseline } V_m) / (\text{Steady state } V_m - \text{Baseline } V_m)$ . Baseline  $V_m$  was determined by averaging the first 300 ms of the recordings, Steady state  $V_m$  was the average of the last 100 ms of the long (600 ms,  $\pm 10$  pA) current injections evoked  $V_m$  changes.

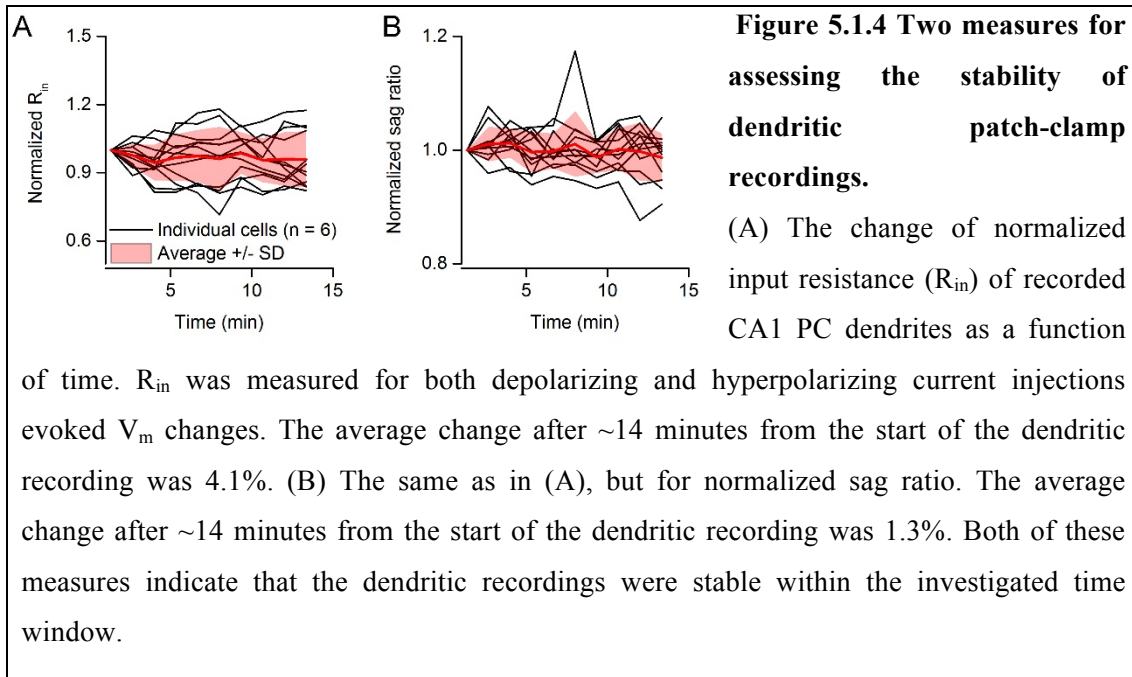
Since the signal attenuation in both directions is modest in control conditions in CA1 PCs, we reasoned that by applying a cocktail of antagonists and ion channel blockers to the control solution, the cell would be more compact, leading to even less pronounced signal attenuation along the dendrites. This prompted me to the omission of

the somatic electrode from the experimental arrangement for the remaining of the study and investigate the subcellular distribution of ion channels with a single dendritic electrode positioned on the recorded dendrites at different distances in the SP.

To test the hypothesis that this combined methodological approach is capable of determining subcellular ion channel distributions, I first sought to validate it with an ion channel whose subcellular distribution in CA1 PCs has been described before: HCN channels (Magee, 1998; Lőrincz et al., 2002). To this end, after establishing conditions under which the dendritic cell membrane fulfils the criteria of passiveness (see Methods and Section 5.1.4), I excluded the HCN channel blocker ZD7288 from the recording solution to investigate HCN channels effect on dendritic membrane properties in intact (control) and blocked (ZD7288) conditions (see sections 5.1.4 and 5.1.6) and infer their distributions along the main apical dendrite of CA1 PCs.

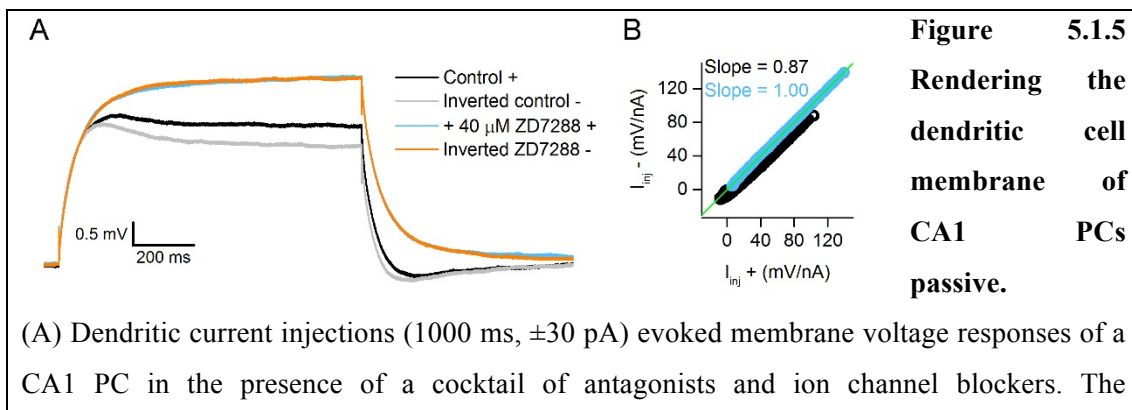
### 5.1.3 Stability of dendritic recordings

The designed approach is based on *in vitro* dendritic patch-clamp recordings with the application of pharmacological agents to block ion channels. It is therefore of great importance to maintain stable dendritic recordings long enough to acquire the voltage signal in control conditions and after drug application. I monitored the stability of the recordings by the  $R_{\text{access}}$  of the dendritic pipette ( $\leq 62 \text{ M}\Omega$ ) and two physiological parameters: the changes in sag ratio ( $\text{Sag } V_m - \text{Baseline } V_m / (\text{Steady state } V_m - \text{Baseline } V_m)$ ; Figure 5.1.3 and Figure 5.1.4B) and normalized  $R_{\text{in}}$  (measured at the last 100 ms of the long current pulse-evoked  $V_m$  responses; Figure 5.1.4A) as a function of time. The  $R_{\text{access}}$  was carefully monitored and adjusted throughout the duration of the recordings, if needed. The two measured physiological parameters changed on average by 4.1% (normalized  $R_{\text{in}}$ , SD = 0.124%) and 1.3% (normalized sag ratio, SD = 0.042%), indicating stable recording conditions within the monitored period. The recordings were maintained on average for ~14 minutes, because the applied drug for blocking HCN channels (ZD7288) exerted its maximal effect within ~8 minutes (indicated by disappearance of the 'sag' potential and stable baseline  $V_m$  without current injections) and the remaining ~6 minutes were enough to acquire control and drug condition voltage signals.



### 5.1.4 Rendering the dendritic cell membrane of CA1 PCs passive

In order to be able to model dendritic current injection-evoked  $V_m$  changes of hippocampal CA1 pyramidal neurons with the fewest possible variables, I included a set of antagonists and ion channel blockers in the ACSF to render the dendritic cell membrane passive. This cocktail included 3 mM kynurenic acid and 20  $\mu$ M SR95531 to block non-*N*-methyl-D-aspartate (NMDA)-type glutamatergic and GABA<sub>A</sub> receptor mediated neurotransmission, respectively (to eliminate synaptic noise and therefore increase signal-to-noise ratio of the recordings), 50  $\mu$ M Cd<sup>2+</sup> to block voltage-gated Ca<sup>2+</sup> channels, 1  $\mu$ M TTX and 5 mM 4-AP to block voltage-gated Na<sup>+</sup> and K<sup>+</sup> channels, respectively and 40  $\mu$ M ZD7288 to block HCN channels.



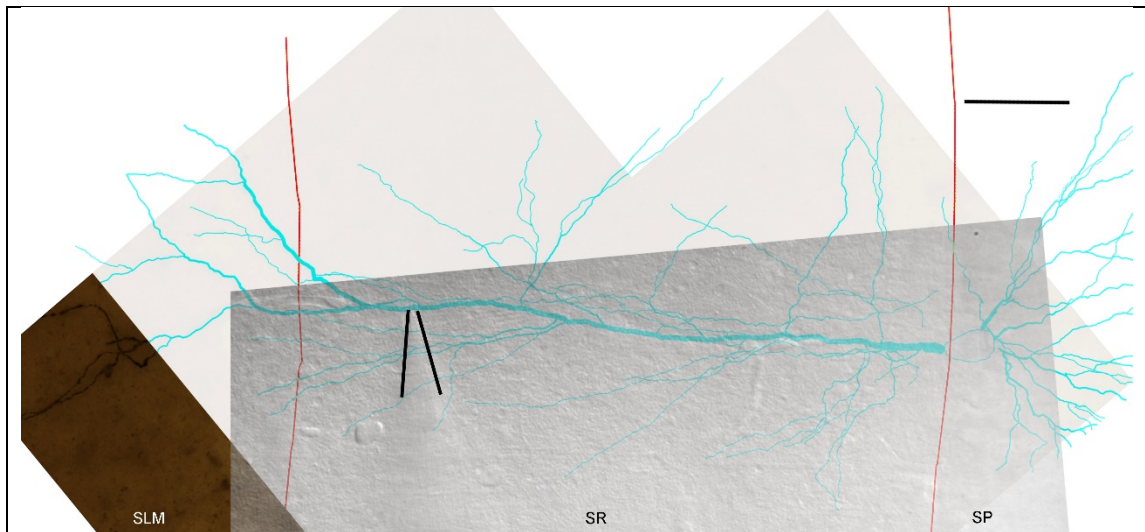
hyperpolarizing current injection evoked voltage traces were inverted for easier comparison with its depolarizing counterparts. The control solution lacks the HCN channel blocker ZD7288, but contains 3 mM kynurenic acid, 20  $\mu\text{M}$  SR95531, 50  $\mu\text{M}$   $\text{Cd}^{2+}$ , 1  $\mu\text{M}$  TTX and 5 mM 4-AP. After perfusion of the control solution with 40  $\mu\text{M}$  ZD7288, the dendritic cell membrane became passive (almost identical blue and orange traces without nonlinearities of the control traces). The baseline  $V_m$  was  $-65$  mV. (B) Linearity curves of the recorded voltage traces shown in (A). The membrane shows rectification under control conditions (black dots), while inclusion of 40  $\mu\text{M}$  ZD7288 in the control solution rendered the dendritic cell membrane passive (blue dots). The slopes of the linear fits were 0.87 and 1.00 for control and ZD7288 conditions, respectively.

Acute brain slices were bathed in normal ACSF including the aforementioned cocktail in the recording chamber, that allowed me to record the dendritic  $V_m$  changes in passive conditions, i.e. for a given square pulse current injection, the cell membrane responded in a symmetric and linear fashion (Figure 5.1.5A, blue and orange traces). Linear  $V_m$  responses lack the ‘sag’ potential in ZD7288 conditions (Figure 5.1.2 and 5.1.3). Symmetry is defined as following: the same square pulse current is injected into the cell with positive and negative amplitudes. Inverting the negative current injection-evoked  $V_m$  response of the cell should overlap with that of its depolarizing counterpart. For a quantitative investigation of these properties, I plotted the depolarizing and hyperpolarizing current injection-evoked  $V_m$  responses against each other. Passiveness of the cell membrane is confirmed if the slope of linear regression of these curves is close to one (Figure 5.1.5B, blue curve).

As described in the last paragraph of section 5.1.2, the control solution in which the cells were recorded lacked the HCN channel blocker ZD7288, and the same current was injected into the dendrite with positive and negative amplitudes (Figure 5.1.5A, black and grey traces). The representative example illustrates the voltage dependence of HCN channels.

### 5.1.5 Morphological reconstruction of recorded cells and identification of pipette location

During the *in vitro* electrophysiological experiments, the recorded cells were filled with biocytin for 3D morphological reconstruction with the NeuroLucida system (see Methods). To determine the exact location of the recording pipette on the patched apical dendrites of CA1 PCs, the IR-DIC image acquired during the recordings was superimposed to the reconstructed morphology of the neuron (Figure 5.1.6). After matching the curvature of the border of SP and SR on the two images (approximate border is shown by red line in Figure 5.1.6), the position of the dendritic pipette could be determined on the dendrite (which was  $\sim 300 \mu\text{m}$  away from the somata of the recorded cell shown in Figure 5.1.6; pipette contour is enhanced by black lines).



**5.1.6 Determining the absolute position of the recording pipette on the ‘blindly’ patched dendritic tree of CA1 PCs.** All recorded dendrites were filled with biocytin during the *in vitro* patch-clamp recordings and fixed for procession with DAB (bottom, brownish layer, see Methods). 3D morphological reconstruction of the whole neuron was performed with the NeuroLucida software (middle layer, the cell is visualized with blue, red lines represent the borders of stratum SLM, SR and SP). Overlaying the IR-DIC image acquired during the *in vitro* patch-clamp recordings and matching curvature of the border of SP and SR provides a good estimate of the dendritic pipette’s location on the dendritic tree of the recorded neuron. The path distance between the origin of the apical dendrite and the site of the dendritic recording is  $297 \mu\text{m}$  for the representative example. The scale bar represents  $50 \mu\text{m}$ .

### 5.1.6 Modelling *in vitro* recorded $V_m$ responses of individual CA1 PCs

Using the *in vitro* electrophysiological experiments and 3D morphological reconstructions of the recorded neurons, as the last step of the proposed combined approach, I sought to determine the distance-dependent subcellular distribution of HCN channels along the apical dendritic tree of CA1 PCs with multi-compartmental modelling. The 3D morphology and  $V_m$  traces of the cells were imported into the NEURON simulation environment to first determine the passive electrical properties ( $R_m$ ,  $C_m$  and  $R_a$ ) of individual neurons. To this end, I fitted the passive  $V_m$  responses (i.e. those recorded in ZD7288 conditions) of the cells with a purely passive model, which had a leak conductance ( $G_{leak}$ ) inserted into the cell membrane with a uniform density. The equation in this case is simplified to the following:

$$C_m \frac{dV}{dt} = I - G_{leak}(E_{leak} - V) \quad (5.1),$$

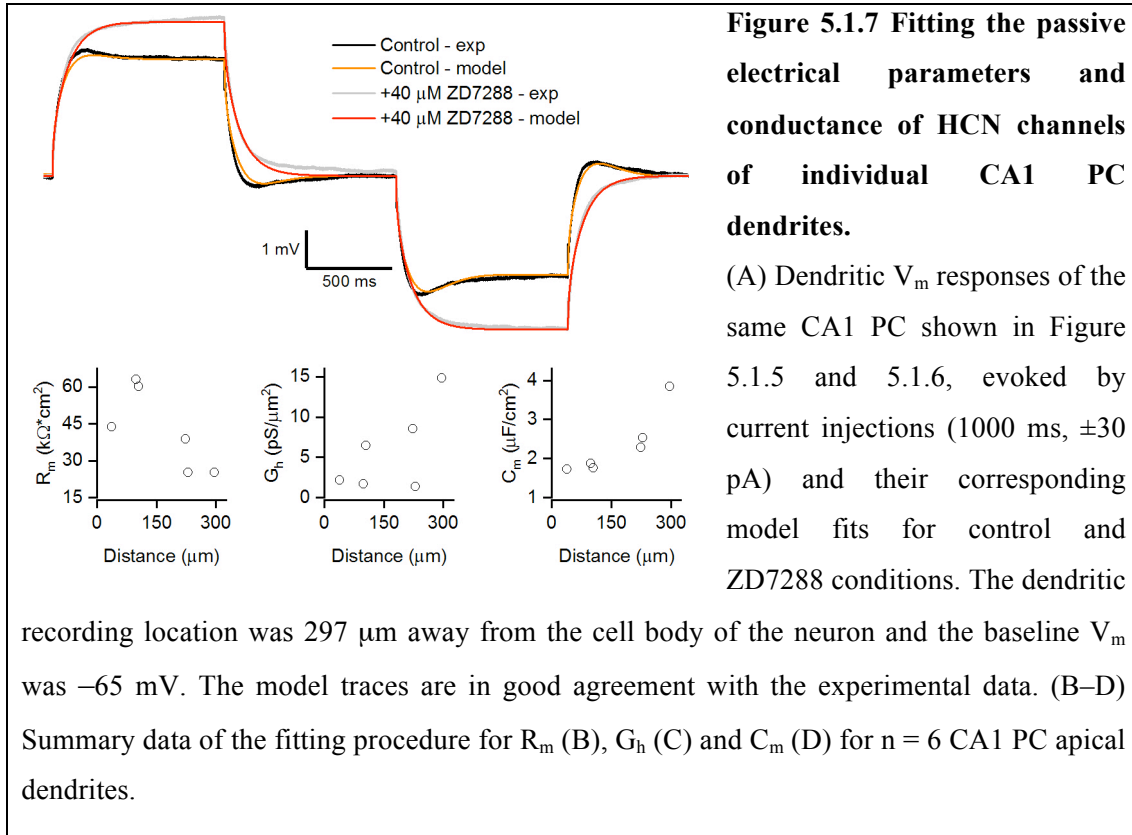
where  $G_{leak}$  is in reciprocal relationship with  $R_m$  ( $G_{leak} = 1/R_m$ ),  $E_{leak}$  is the reversal potential of the  $G_{leak}$  (set independently for all  $n = 6$  cells, as their recorded baseline  $V_m$ ) and  $V$  is the actual transmembrane voltage of the dendrite and  $I$  is the total transmembrane current. The  $R_a$  was  $150 \Omega \cdot \text{cm}$  for all simulations. I fitted the experimental data recorded in ZD7288 conditions with NEURON's built-in Praxis fitting algorithms by letting  $R_m$  and  $C_m$  iterating freely to obtain the best fit of the model to the data (Figure 5.1.7A, grey and red traces for experimental and model data, respectively). The representative example on Figure 5.1.7A shows that the experimental data in control conditions could be fitted properly with a passive model with a  $R_m$  of  $25.3 \text{ k}\Omega \cdot \text{cm}^2$  and  $C_m$  of  $3.85 \mu\text{F}/\text{cm}^2$ .

To estimate the local conductance of HCN channels ( $G_h$ ), I also fitted  $G_h$  on the experimental data recorded in control conditions. During this fitting procedure, the previously obtained values of  $R_m$  and  $C_m$  were fixed and only  $G_h$  was iterated, which was inserted into the model cell membrane with a uniform density. In this case, the equation had an extra expression compared to eq. 5.1:

$$C_m \frac{dV}{dt} = I - G_{leak}(E_{leak} - V) - G_h(E_h - V) \quad (5.2).$$

Additional small amounts of holding current was injected into the model if needed to set baseline  $V_m$  properly, to match that of the experimental data.  $G_h$  was modified as in

Golding et al., 2005:  $E_h$  was  $-35$  mV and the half activation voltage ( $V_{half}$ ) was  $-88$  mV (adapted from  $I_h$  measurements of Magee, 1998). The model fit was in good agreement with the experimental data (Figure 5.1.7A, black and orange traces for experimental and model data, respectively).



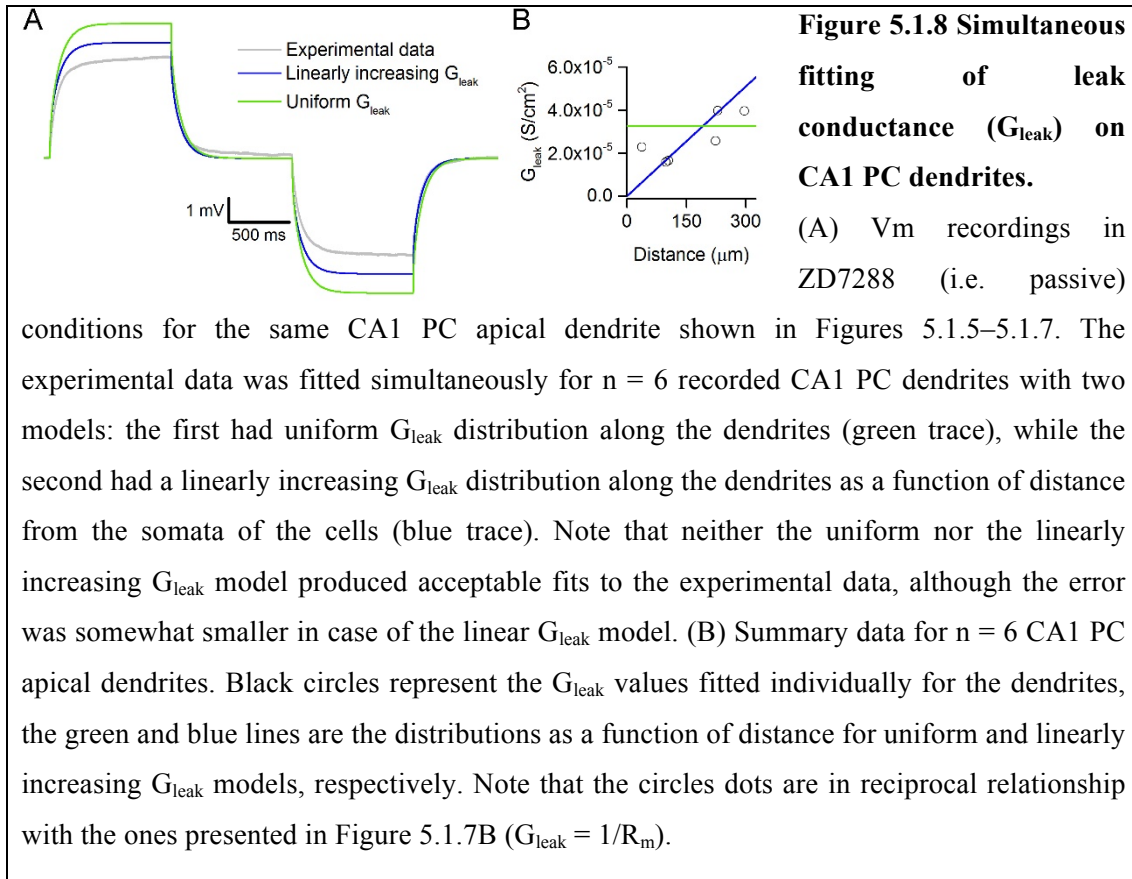
Fitting of six recorded and reconstructed cells revealed some interesting findings: the  $R_m$  of the cells shows a decrease as a function of distance from the soma (Figure 5.1.7B), which justified the hypothesised presence of nonuniformities in the  $G_{leak}$  distribution of the dendrites of these cells (see also section 5.1.2). Parallel with this, the  $C_m$  increases as a function of distance from the soma (Figure 5.1.7D). At this point, it has to be noted that the morphological reconstructions of the neurons do not include spines, which provide additional surface to the neurons. Instead of scaling uniformly with a spine factor of 1.5 (Golding et al., 2005), I let freely iterate the  $C_m$  parameter to obtain the best possible fit to experimental data. Although the value  $\sim 4 \mu\text{F}/\text{cm}^2$  obtained at  $\sim 300 \mu\text{m}$  away from the soma may seem high, anatomical investigations of spine density along the dendrites of CA1 PCs show a considerable

increase of spine density from the proximal to distal SR (0.03 and 6.98  $\mu\text{m}^{-2}$ , respectively; Megías et al., 2001). I do not argue that accurate scaling for the increasing spine density in the model would uniformize the distance dependence of  $C_m$  (and to some extent, that of  $R_m$  as well, since the theoretical membrane time constant  $\tau_m = R_m * C_m$ ; Dayan and Abbott, 2001), however, for explorative investigations, I decided to fit these parameters to obtain the best model fit to the data. The distribution of  $G_h$  was in good agreement with previously reported range (1–2 pS/ $\mu\text{m}^2$  in perisomatic regions and 8–10 pS/ $\mu\text{m}^2$  in distal dendrites (Magee, 1998)) as it also shows a distance-dependent increase from the cell body of the neurons towards the apical dendritic tuft (Figure 5.1.7C). These results strengthened my hypothesis that the above detailed combined approach could be applied to determine subcellular distribution of ion channels.

### **5.1.7 Simultaneous fitting of $V_m$ responses of all recorded cells**

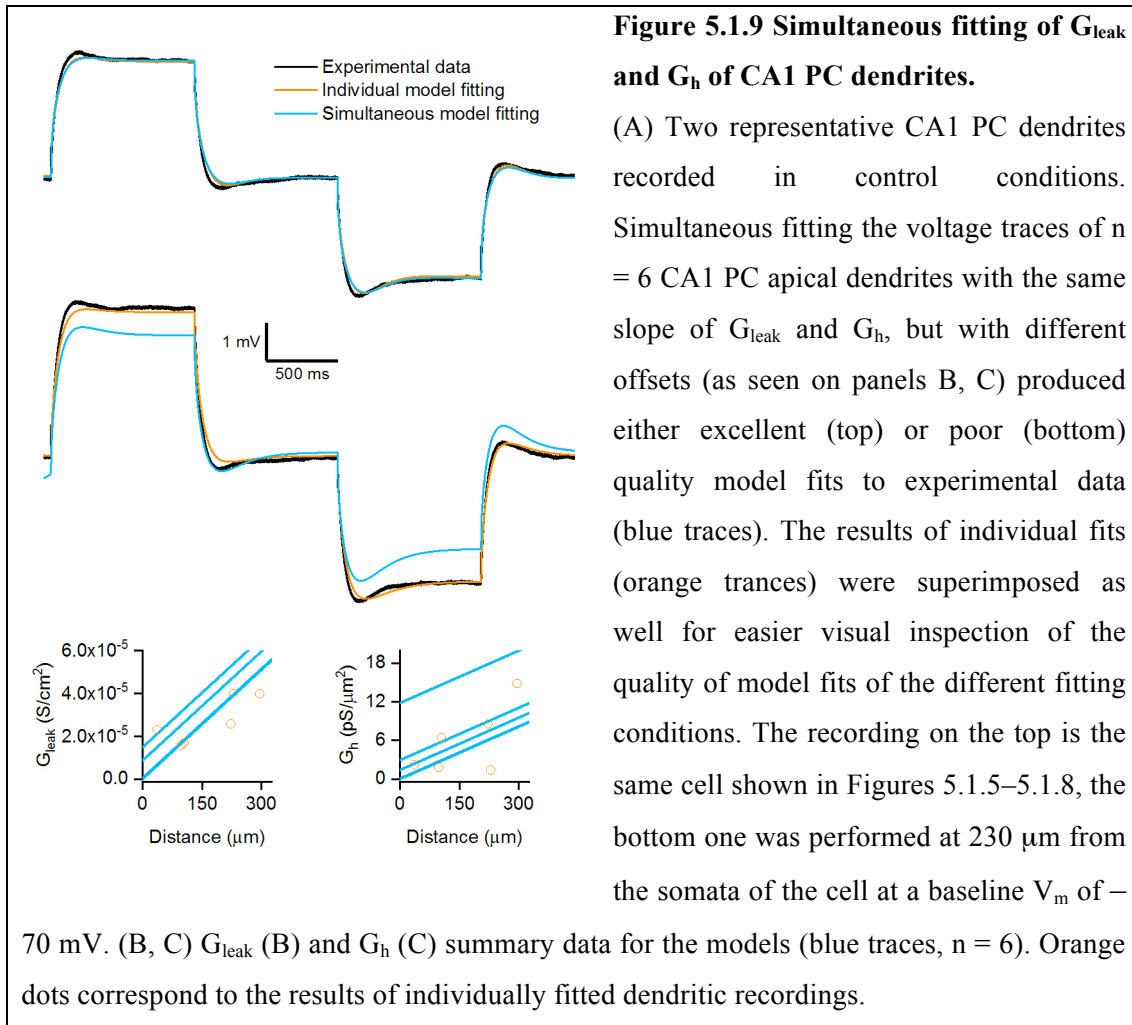
After being able to fit accurately single cells individually, I next tested whether simultaneous fitting of six recorded cells with a single  $G_{\text{leak}}$  distribution is possible. In my initial trials, after importing all the cells and their corresponding passive recordings into the NEURON simulation environment, I tested two scenarios: a uniform and a linearly increasing  $G_{\text{leak}}$  configuration (based on single cell modelling results; Figure 5.1.8). During these simulations, the total error of the six cells were minimized in order to find the best possible model fit to the experimental data. The representative example in Figure 5.1.8A shows that the linearly increasing  $G_{\text{leak}}$  model produced smaller error than its uniform counterpart (supporting the validity of the single cell modelling predictions; blue and green traces, respectively), but both models failed to reproduce the experimental data as accurately as the individually fitted ones (Figure 5.1.7A). The uniform models had a single parameter ( $G_{\text{leak}}$ ) to iterate during the fitting procedure, while the linear models had two parameters (initial  $G_{\text{leak}}$  and slope of its increase as a function of distance). Figure 5.1.8B shows the results of the simultaneous fitting procedure for uniform and linear  $G_{\text{leak}}$  models (green and blue curves, respectively).





The failure of recapitulating the experimental recordings with a single  $G_{leak}$  distribution in the models could be because the CA1 PCs are heterogeneous cell population (superficial and deep, dorsal and ventral differences in ion channel expressions (Maroso et al., 2016; Malik and Johnston, 2017)). To circumvent this possible source of error, the next set of simulations were performed with one more degree of freedom, that is I let the cells have a different baseline  $G_{leak}$ , only the slopes were the same with which the  $G_{leak}$  increased as a function of distance from the soma of the neurons (Figure 5.1.9B). A similar strategy was applied in case of the  $G_h$  (Figure 5.1.9C). In some cases, as the one depicted in Figure 5.1.9A, top, this fitting procedure resulted in models which could replicate the experimental data with great accuracy. These models are indistinguishable from the ones fitted individually (Figure 5.1.9A, top, blue (simultaneous fitting) and orange (individual fitting) traces). However, in another set of cells ( $n = 3$ ), simultaneous fitting resulted in models, which could not reproduce the experimental data (Figure 5.1.9A, bottom, summary of the fitted parameters on Figure 5.1.9B ( $G_{leak}$ ) and C ( $G_h$ )).

The diversity present among hippocampal CA1 PCs could be the reason why the simultaneous fitting of neurons failed to recapitulate experimental results (or just to a limited extent). However, single cell fitting was able to accurately reproduce the recorded  $V_m$  responses with a  $G_h$  distribution in accordance with previous published data (Magee, 1998).



## 5.2 Functional properties of dendritic gap junctions in cerebellar Golgi cells

### 5.2.1 Characterization of passive electrical properties of GoC dendrites

The coupling strength of electrical connections between cerebellar GoCs is highly variable and decreases as a function of distance between the two coupled cells' somata (Dugué et al., 2009; Vervaeke et al., 2010). However, prominent heterogeneity in coupling strength is also present among GoCs having similar intersomatic distances (Vervaeke et al., 2010). A possible explanation for this variance could be that the number of GJs between coupled GoCs was found to be substantially different (between 1 and 9; Vervaeke et al., 2010).

In this chapter, I aimed to determine the underlying mechanisms of the diversity observed in the electrical coupling between these inhibitory cerebellar INs. The strength of electrical coupling is quantifiable using the coupling coefficient (CC), which we determined with *in vitro* paired somatic patch-clamp recordings as the ratio of the post- and presynaptic voltage changes evoked by long (400 ms; 50 pA) current injections into the presynaptic cell. Since active conductances in the perisomatic region of GoCs (Vervaeke et al., 2012) can introduce voltage dependence in the CC (Dugué et al., 2009; Haas et al., 2011), the recordings were performed in the presence of a cocktail of antagonists and channel blockers (see Methods, referred to as passive conditions hereafter) rendering the GoCs' cell membrane passive.

In order to be able to determine the contribution of different factors (e.g. number of GJs between coupled cells, their distance from the cell bodies, their distribution and size along the dendrites) to the substantial variability observed in coupling strength between these neurons, we first aimed to dissect the filtering effect of GJs and dendrites. First, we characterized passive electrical properties ( $R_m$ ,  $C_m$ , and  $R_a$ ) of GoCs, since these parameters, together with the geometry of the cell shape the amplitude and waveform of postsynaptic potentials (review by Spruston, 2008). This process has been accomplished by *in vitro* two-photon targeted dual soma-dendritic patch-clamp recordings in passive conditions (Figure 5.2.1A; performed by Dr. Frederic Lanore in Prof. Angus Silver's laboratory at University College London, London, UK) combined

with the morphological reconstruction of the recorded neurons (Figure 5.2.1B) and *in silico* multi-compartmental modelling, as has been described in chapter 5.1.

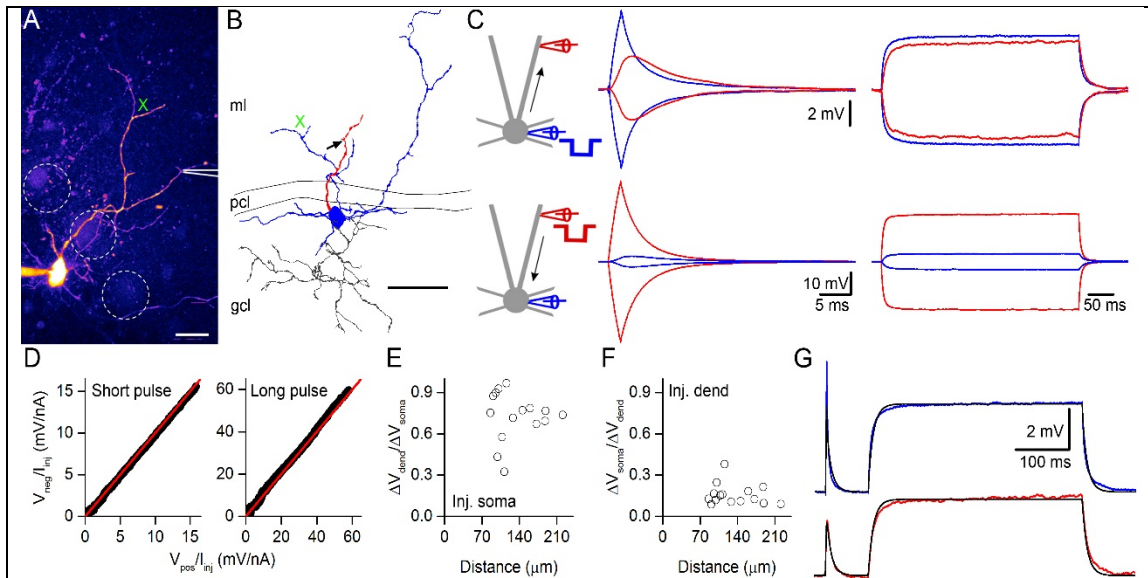


**Figure 5.2.1 Characterization of passive voltage propagation in Golgi cell (GoC) dendrites.**

(A) A two-photon maximum intensity projection image of an Alexa 594-filled GoC. A second pipette without Alexa 594 was used to simultaneously patch a dendrite (indicated by the cartoon). The dashed circles represent Purkinje cell somata. (B) Neurolucida reconstruction of the cell shown in (A) with dendrites coloured in blue and the axon in gray. The patched dendrite is red. The arrow indicates the site of dendritic recording. The green cross indicates a neighbouring dendritic branch and is present in both (A) and (B) for clarity. (C) Simultaneously recorded somatic (blue traces) and dendritic (red traces) voltage responses in the GoC shown in (A) evoked by somatic (top traces) and dendritic (bottom traces) short (left,  $\pm 200$  pA, 2 ms) and long (right,  $\pm 50$  pA, 400 ms) current injections in the presence of a cocktail of antagonists and channel blockers. (D) Linearity curves from the recorded voltage traces shown in (C), indicating no rectification of the somatic voltage responses to short (left) and long (right)

somatic current injections. The slopes of the linear fits were 0.96 for short and 1.04 for long pulses (identity line: red). (E, F) Summary of all control somato-dendritic recordings showing the normalized changes in the voltage responses to somatic (E) and dendritic (F) current injections as a function of distance of the dendritic pipettes from the soma. (G) Simultaneously recorded somatic (top, blue) and dendritic (bottom, red) voltage traces in response to somatic current injections from the cell shown in (A–C). The multi-compartmental model of the

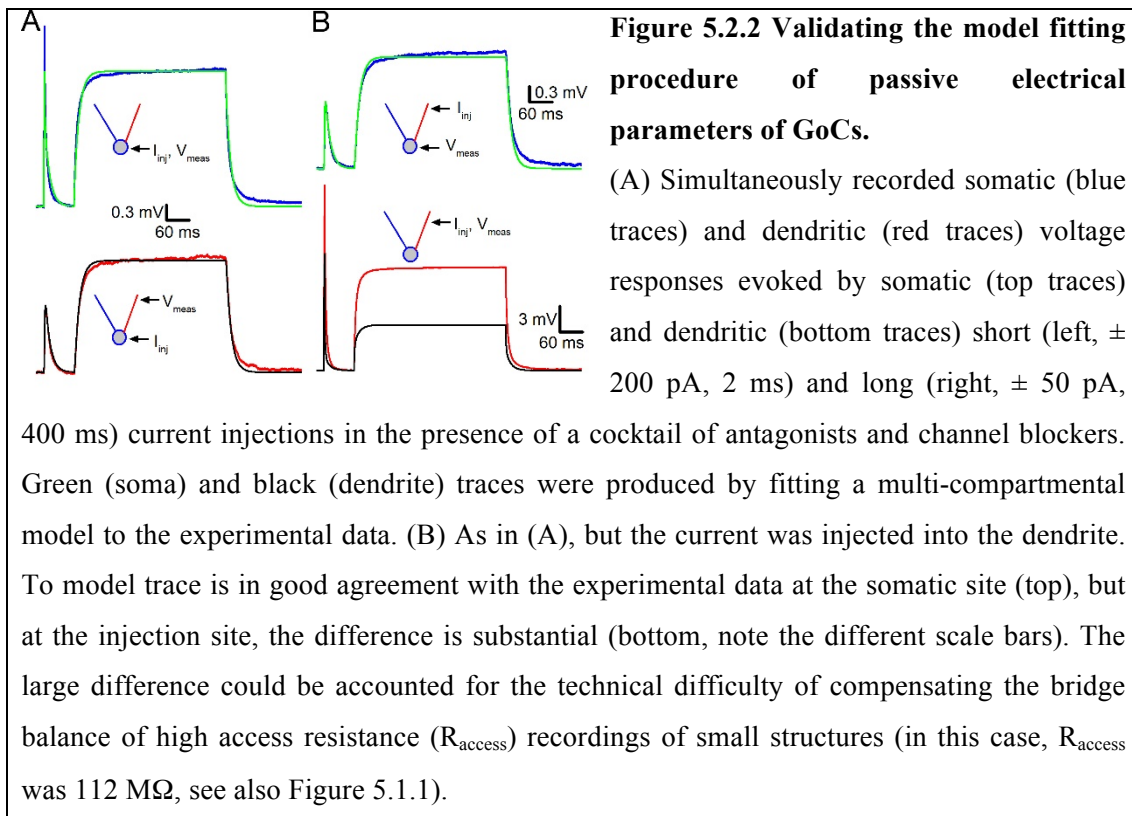
reconstructed cell was fitted (black traces) to the experimental traces. The best fit was obtained with a  $R_m$  of  $3.2 \text{ k}\Omega\cdot\text{cm}^2$ , a  $R_a$  of  $188.9 \text{ }\Omega\cdot\text{cm}$ , and a  $C_m$  of  $3.3 \text{ }\mu\text{F}/\text{cm}^2$  (Abbreviations: molecular layer, ml; Purkinje cell layer, pcl; and granule cell layer, gcl). The scale bars represent  $20 \text{ }\mu\text{m}$  in (A) and  $50 \text{ }\mu\text{m}$  in (B).

Simultaneous somatic and dendritic voltage responses were recorded during short ( $2 \text{ ms}$ ,  $\pm 200 \text{ pA}$ ) and long ( $400 \text{ ms}$ ,  $\pm 50 \text{ pA}$ ) current injections (Figure 5.2.1C). The symmetry of the depolarizing and hyperpolarizing responses to either somatic or dendritic current injections indicated that the membrane was linear (Figure 5.2.1C). Moreover, the slopes of linear regression to short and long current injection-evoked voltage responses were close to one ( $0.96$  and  $1.04$ ; Figure 5.2.1D). The steady-state dendritic signal attenuation was then quantified by plotting the relative changes in the voltage at somatic and dendritic sites as a function of distance. Unlike in CA1 PCs, centripetal attenuation was substantially larger than centrifugal attenuation as expected from the impedance mismatch between the large soma and fine dendrites (Figures 5.2.1E and 5.2.1F). This observation also suggests a uniform  $G_{\text{leak}}$  distribution throughout the dendritic tree of these neurons.

To determine passive electrical properties of GoCs, we carried out *post hoc* LM reconstructions of those cells where the morphology was sufficiently preserved (Figure 5.2.1B) and built multi-compartmental models of the recorded cells in the NEURON simulation environment to fit the model to the electrophysiological data. As these neurons fulfilled the criteria of passiveness, a single  $G_{\text{leak}}$  was inserted into the model cells' membrane with a uniform density, since the results of dual soma-dendritic patch-clamp recordings are consistent with a uniform distribution. I iterated freely the  $R_m$ ,  $C_m$  and  $R_a$  parameters to obtain the best fit of the experimental data (Figure 5.2.1G), resulting in an  $R_m$  of  $5.5 \pm 2.3 \text{ k}\Omega\cdot\text{cm}^2$ , an  $R_a$  of  $206 \pm 81 \text{ }\Omega\cdot\text{cm}$  and a  $C_m$  of  $2.7 \pm 0.7 \text{ }\mu\text{F}/\text{cm}^2$  ( $n = 5$ ).

Because of the small calibre dendrites (often less than  $1 \text{ }\mu\text{m}$  in diameter) of GoCs, the relatively high  $R_{\text{access}}$  (mean:  $67 \text{ M}\Omega$ ) of the dendritic recordings could potentially introduce additional errors of the recordings (see section 5.1.1), I only used the somatic current injection-evoked  $V_m$  traces during the fitting procedure to obtain

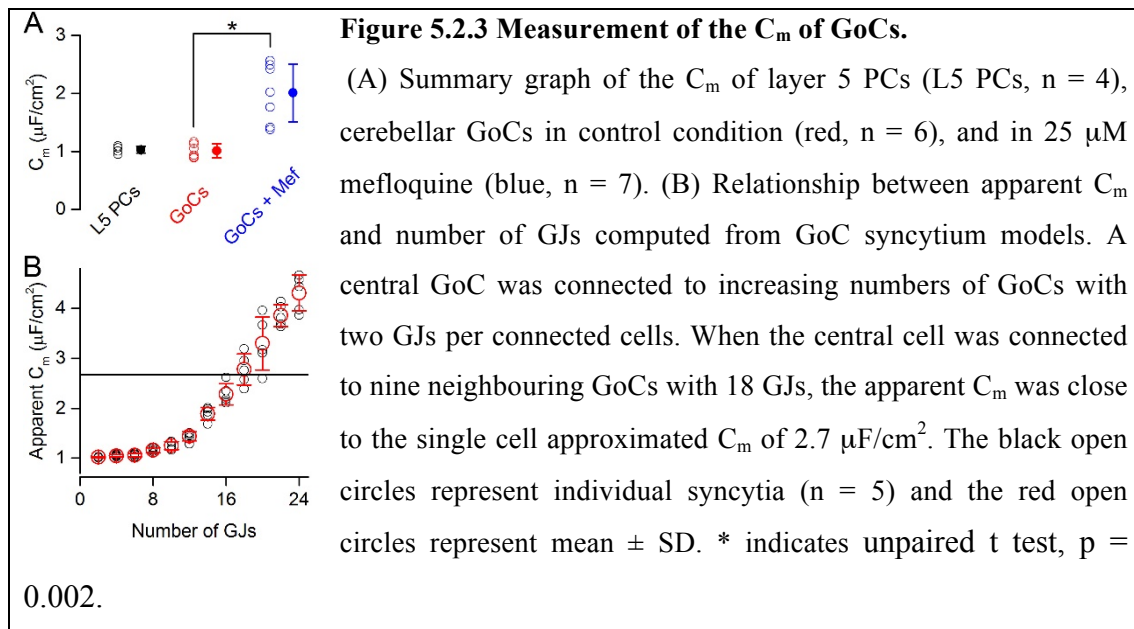
passive electrical parameters (Figures 5.2.1G and 5.2.2A). However, to crosscheck the passive electrical parameters obtained by this fitting procedure, I also used the dendritic current injection-evoked somatic  $V_m$  responses (Figure 5.2.2B). With the same set of  $R_m$ ,  $C_m$  and  $R_a$ , when current is injected into the dendrite, the local voltage change of the model substantially underestimates the experimental data (Figure 5.2.2B, bottom), whereas the  $V_m$  traces recorded by the reference electrode at the soma, which is not prone to the error caused by the high  $R_{\text{access}}$ , shows excellent agreement with the model (Figure 5.2.2B, top). This observation strengthened our notion, that the high  $R_{\text{access}}$  dendritic recordings should be omitted from the fitting procedure, but the somatic recordings could be used as a reference to check the quality of the fit when current is injected into the dendrite.



### 5.2.2 $C_m$ measurements of GoCs

These values of  $R_a$  and  $C_m$  are considerably larger than those obtained from other neurons (Stuart and Spruston, 1998; Roth and Häusser, 2001; Norenberg et al., 2010), suggesting that either GoC passive properties are different or that these

properties are influenced by the electrically coupled syncytium within which the GoCs are embedded (Alcami and Marty, 2013). To distinguish between these possibilities, GoC membrane properties were directly examined by Dr. Frederic Lanore using a method described by Gentet et al., 2000. As a reference, cortical L5 PCs were also tested and similar values were obtained ( $1.03 \pm 0.06 \mu\text{F}/\text{cm}^2$  ( $n = 4$ ) compared to  $0.9 \mu\text{F}/\text{cm}^2$  (Gentet et al., 2000) and  $1.2 \mu\text{F}/\text{cm}^2$  (Larkum et al., 2009)). Repeating these experiments in GoCs yielded a  $C_m$  of  $1.01 \pm 0.12 \mu\text{F}/\text{cm}^2$  (Figure 5.2.3A;  $n = 6$ ). These results demonstrate that the  $C_m$  of GoCs are similar to that of other central neurons.

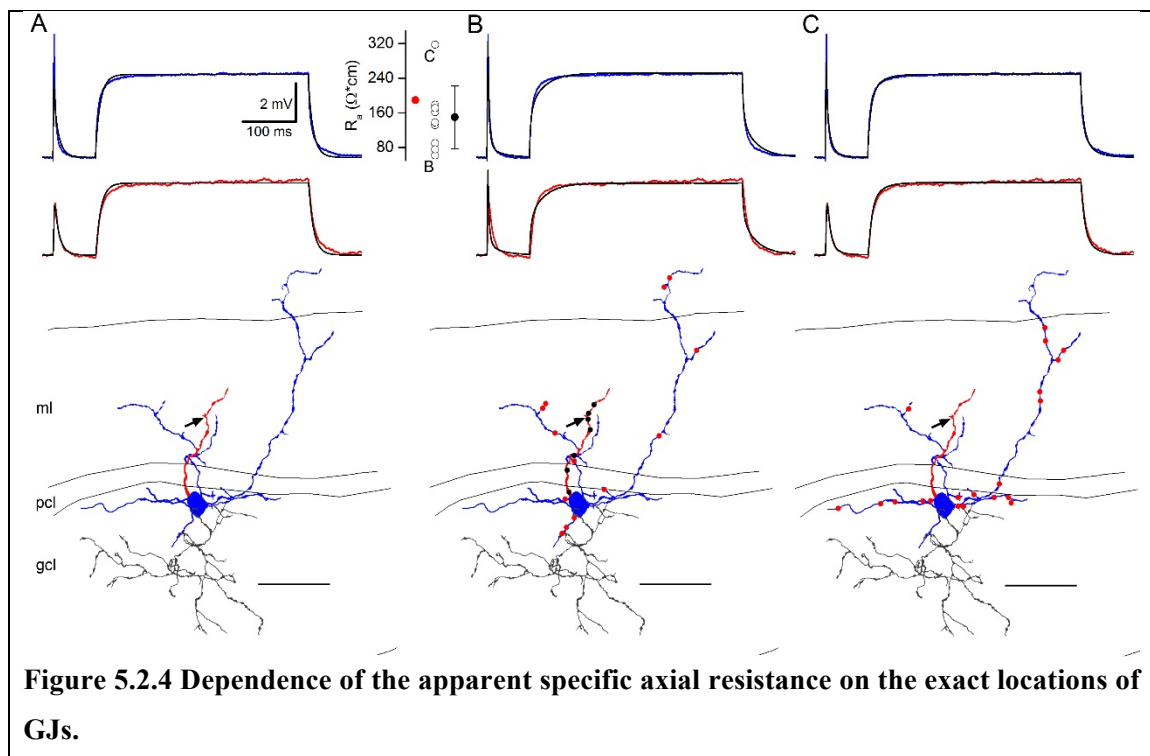


To examine the effect of syncytium on the ‘apparent  $C_m$ ’, I simulated networks with 1 to 12 cells coupled to a central GoCs by two GJs, each having a conductance of 1 nS. I fixed  $C_m$  to  $1 \mu\text{F}/\text{cm}^2$  and the  $R_{in}$  to  $120 \text{M}\Omega$  in all GoCs based on the population average of control cells. Current was injected into the central neuron and the resulting voltage trace was recorded. Next, I determined the apparent  $C_m$  of the central neuron following its disconnection from the electrical syncytium by setting the  $G_{GJ}$  to 0 nS. This was achieved by letting  $R_m$  and  $C_m$  values iterating freely during the fitting procedure until the central neuron’s voltage response matched that obtained when it was embedded within the syncytium. The apparent  $C_m$  increased monotonically as a function of GoC syncytium size and, when nine GoCs were connected to the central neuron via 18 GJs, the apparent  $C_m$  matched the value obtained experimentally ( $2.7 \mu\text{F}/\text{cm}^2$ , Figure

5.2.3B). These results demonstrate that the large apparent  $C_m$  could arise from the electrical coupling to the GoC syncytium and suggest that well established methods for estimating neuronal passive electrical properties are not directly applicable to electrically interconnected networks.

### 5.2.3 Determining $R_a$ of GoC dendrites

I next examined whether the presence of electrical synapses on GoC dendrites could also influence the estimate of  $R_a$ . To do this, I generated ten electrically coupled GoC syncytia, each modelled as a central cell with ten neighbouring cells coupled by two GJs of 1 nS each, randomly placed over the dendritic tree. I then iterated  $R_m$ ,  $C_m$  and  $R_a$  to fit the somatic and dendritic  $V_m$  responses evoked by somatic current injections. Different GJ distributions resulted in a large variability in the estimate  $R_a$  values (Figure 5.2.4). Four GJs in the vicinity of the dendritic recording pipette resulted in the lowest  $R_a$  ( $62 \Omega \cdot \text{cm}$ ; Figure 5.2.4B), whereas the highest  $R_a$  ( $318 \Omega \cdot \text{cm}$ ) was obtained from a syncytium in which not a single GJ was present on the recorded dendrite (Figure 5.2.4C). These results illustrate that the dendritic location of GJs have a profound influence on the estimated  $R_a$ .





(A) Top: Simultaneously recorded somatic (blue traces) and dendritic (red traces) voltage traces in response to somatic current injections from the cell shown below. Multi-compartmental model of the reconstructed cell was fitted (black traces) to the experimental voltage traces. The best fit was obtained with a specific membrane resistance ( $R_m$ ) of 3.2  $k\Omega \cdot \text{cm}^2$ , a specific axial resistance ( $R_a$ ) of 188.9  $\Omega \cdot \text{cm}$  and a specific membrane capacitance ( $C_m$ ) of 3.3  $\mu\text{F}/\text{cm}^2$ . Inset: The estimated  $R_a$  from the 10 syncytia (black open circles are individual syncytia; filled circle is mean  $\pm$  SD) revealed that randomly distributed gap junctions on the dendritic tree of GoCs strongly influence the estimated  $R_a$ . The  $R_a$  estimate of the single cell fitting is shown in red. Bottom: Neurolucida reconstruction of the GoC. The dendrite targeted by the dendritic patch pipette is shown in red, the other dendrites and the soma are in blue, the truncated axon is in gray. The arrow indicates the location of the dendritic patch pipette. (B, C) Top traces are the best fits obtained with 2 syncytia (out of 10 random syncytia) that produced the lowest (B) and highest (C)  $R_a$  estimates. GJ conductance ( $G_{GJ}$ ) was kept constant at 1 nS in all simulations (20 GJs, connecting 10 other cells). Dots indicate the locations of GJs on the dendritic tree (black dots on the red dendrite targeted by the dendritic patch pipette (arrow), red dots on the remaining part of the dendritic tree shown in blue). Scale bars: 50  $\mu\text{m}$  in (A–C).

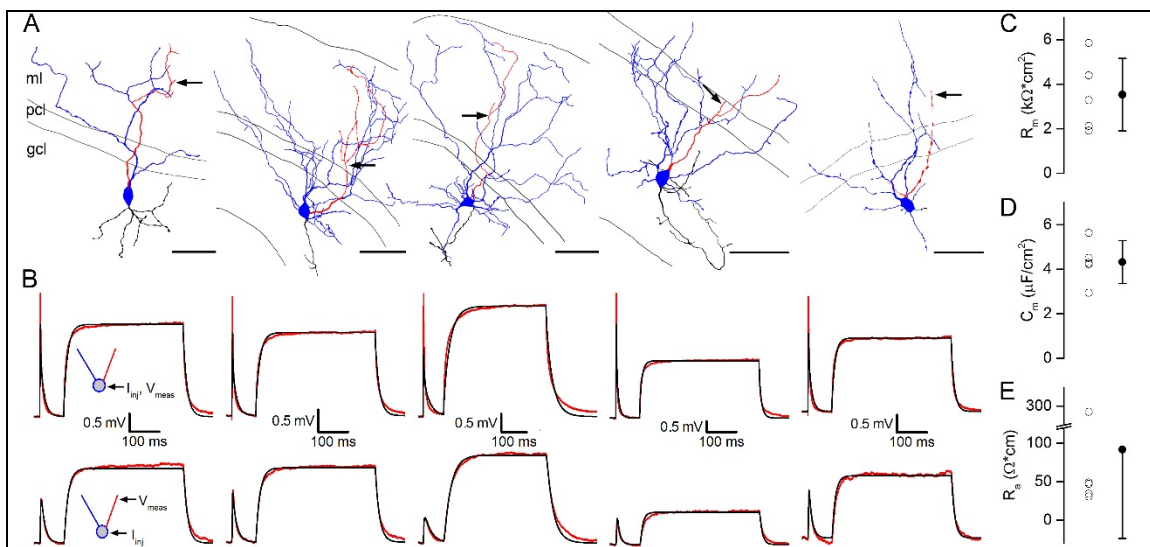


**Figure 5.2.5 Estimation of the  $R_a$  of GoC dendrites.**

(A) Neurolucida reconstruction of five recorded and biocytin filled GoCs with partially reconstructed axons (blue: soma and dendrites; red: patch pipette targeted dendrites; and black: truncated axons). Dual somato-dendritic recordings were performed in the presence of a cocktail of antagonists and channel blockers plus 25  $\mu\text{M}$  mefloquine and 10  $\mu\text{M}$  4-AP. The

arrows indicate the position of the dendritic patch pipettes. (B) Somatic (top) and dendritic (bottom) voltage traces (red) in response to somatic current injections (100 pA, 2 ms and 20 pA, 400 ms) recorded from the cells shown in (A).  $R_m$ ,  $R_a$ , and  $C_m$  were fitted (black). (C–E) Values of  $R_m$  (C),  $C_m$  (D) and  $R_a$  (E) obtained from fitting models of the 5 GoCs shown in (A) and (B). Filled symbols are means  $\pm$  SD. The scale bars represent 50  $\mu\text{m}$  in (A).

Because we could not determine the exact location and strength of each GJ on the recorded and reconstructed GoCs, we estimated  $R_a$  following the pharmacological blockage of GJs with 25  $\mu\text{M}$  mefloquine, (Cruikshank et al., 2004; Vervaeke et al., 2010). Similarly to control conditions, two-photon targeted dual soma-dendritic patch-clamp recordings were performed from GoCs (by Dr. Frederic Lanore). Five of the recorded cells were then *post hoc* reconstructed morphologically and were used for modelling (Figure 5.2.5A). In these models, the  $R_m$ ,  $C_m$  and  $R_a$  were iterated to obtain the best fit to the somatically and dendritically recorded traces upon somatic current injections (Figure 5.2.5B), resulting in an  $R_m$  of  $3.5 \pm 1.6 \text{ k}\Omega\cdot\text{cm}^2$ , a  $C_m$  of  $4.3 \pm 1 \mu\text{F}/\text{cm}^2$  and an  $R_a$  of  $92 \pm 115 \Omega\cdot\text{cm}$  (Figures 5.2.5C – 5.2.5E). Interestingly, even though the majority of Cx36 channels were blocked by mefloquine ( $\sim 80\%$ ), the  $C_m$  estimate remained high (Figure 5.2.5D). To investigate this unexpected result, nucleated patch-clamp recordings were performed by Dr. Frederic Lanore from GoCs preincubated in 25  $\mu\text{M}$  mefloquine (Figure 5.2.3B). These experiments revealed that in the presence of mefloquine, the  $C_m$  was  $2.01 \pm 0.5 \mu\text{F}/\text{cm}^2$  ( $n = 7$ ), significantly higher than obtained under control conditions ( $p = 0.002$ , unpaired t test). This suggests that mefloquine binds to the membrane and increases  $C_m$ , consistent with a previous study showing that mefloquine indeed binds to membrane phospholipids (Chevli and Fitch, 1982).

#### **5.2.4 Estimation of GJ plaque conductance by modelling GoC pairs embedded within an electrically interconnected syncytium**

Classical methods of estimating  $G_{GJ}$  from experimentally measured  $R_{in}$  and CCs are based on single compartmental models connected by a resistor to represent the electrical synapse (Bennett, 1966; Devor and Yarom, 2002; Fortier and Bagna, 2006).

This approach lumps together the voltage attenuation along the dendrites and through the GJs into a single value. To directly address their individual contributions and to estimate  $G_{GJ}$ , I constructed multi-compartmental models of the reconstructed cell pairs (*in vitro* paired somatic patch-clamp recording by Dr. Frederic Lanore, *post hoc* LM and EM reconstructions by Dr. Andrea Lőrincz) using the experimentally determined GJ locations (Vervaeke et al., 2010 and Figure 5.2.6),  $R_a$  ( $92 \Omega \cdot \text{cm}$ , Figure 5.2.5) and  $C_m$  values ( $1 \mu\text{F}/\text{cm}^2$ ; Figure 5.2.4) and embedded them into two syncytia with each central cell being connected to ten other GoCs through 20 GJs randomly distributed on their dendritic tree (Figure 5.2.6A). I generated ten syncytia for the four reconstructed pairs. I then fitted the  $R_m$  in one of the cells to match its somatic voltage and the  $G_{GJ}$  to obtain the best fit of the membrane response in the connected cell (Figures 5.2.6B and 5.2.6C). The sequential fitting of  $R_m$  and  $G_{GJ}$  was iterated until their values changed by less than 5%. This approach resulted in a mean  $R_m$  of  $32 \pm 7 \text{ k}\Omega \cdot \text{cm}^2$  (Figure 5.2.6D, top) and a mean  $G_{GJ}$  of  $0.94 \pm 0.35 \text{ nS}$  (Figure 5.2.6D, bottom;  $n = 4$  reconstructed GoC pairs).

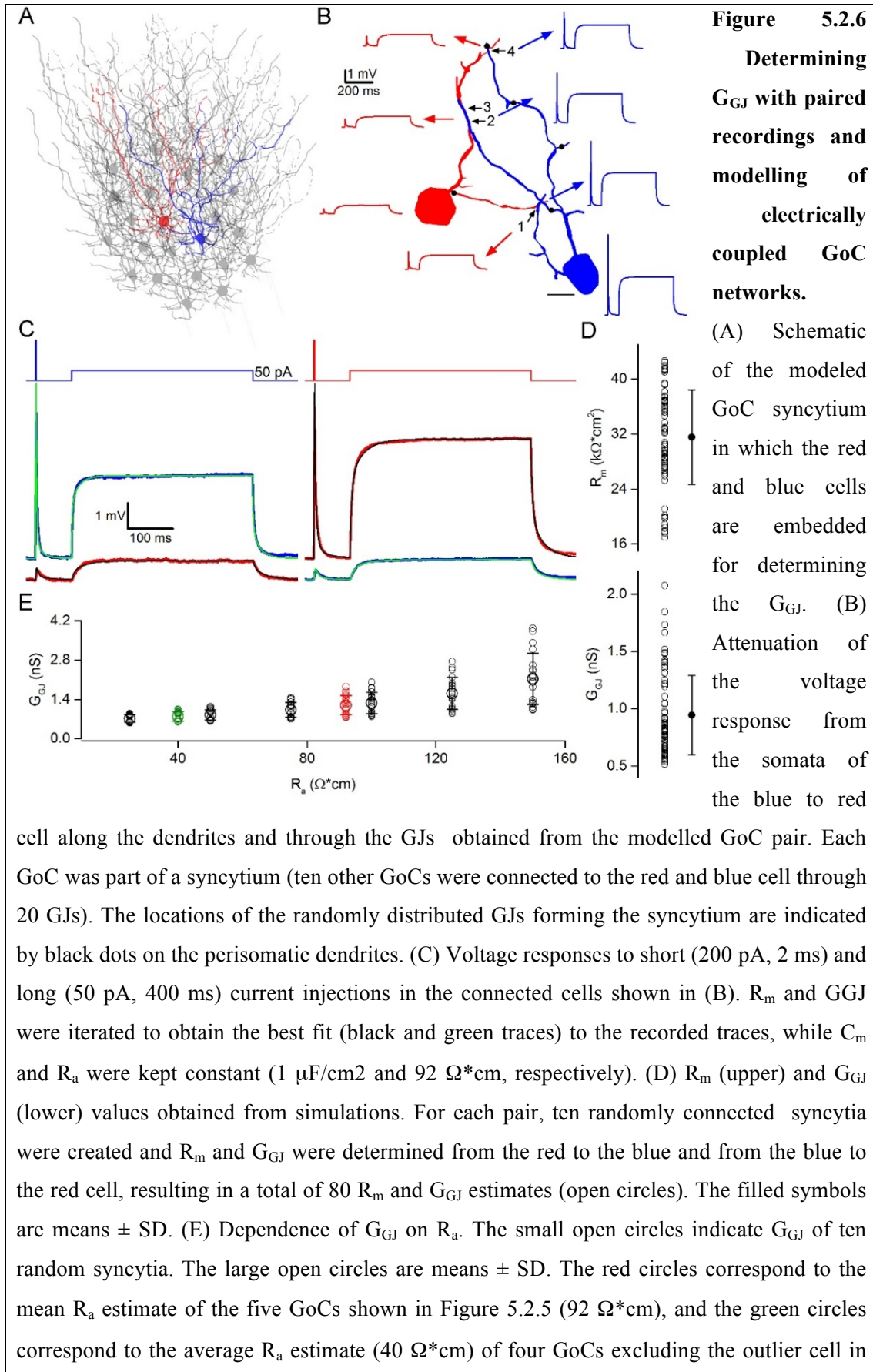


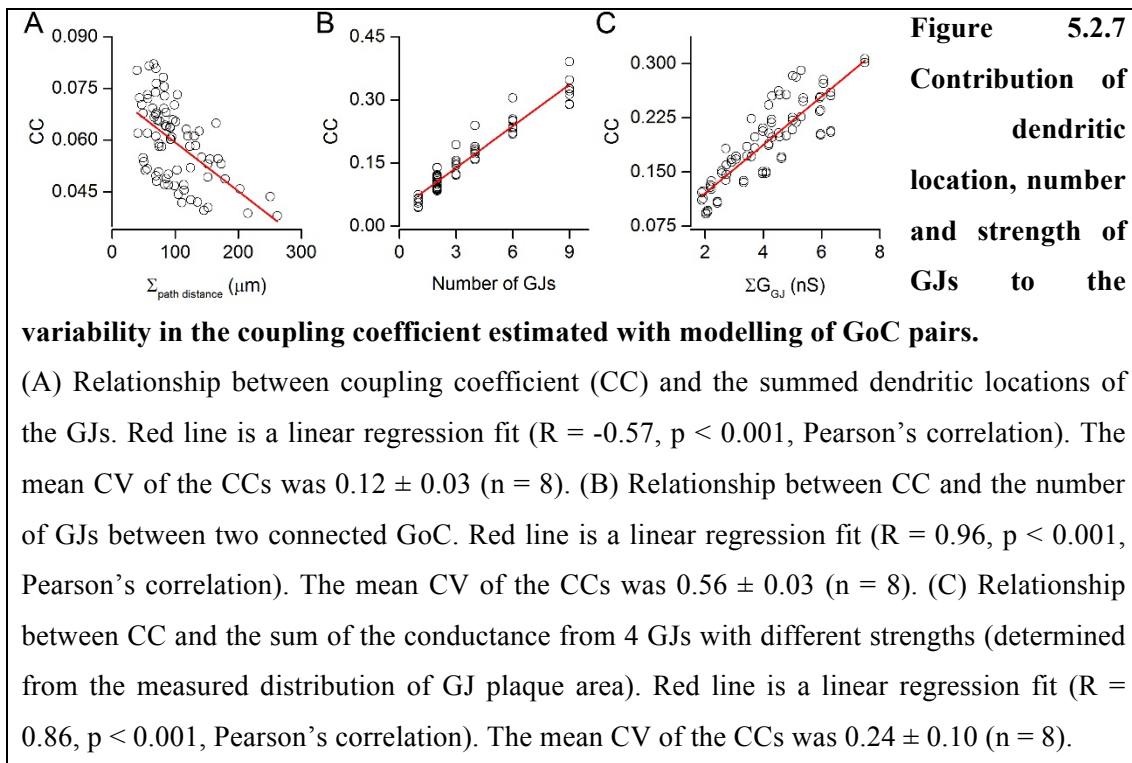
Figure 5.2.5E. The scale bar represents 10  $\mu\text{m}$  in (B).

To determine the robustness of our estimate of  $G_{GJ}$ , I also tested the dependence of  $G_{GJ}$  on the  $R_a$  parameter using the fitting procedure detailed above (Figure 5.2.6E). These simulations showed that within a biologically plausible range of  $R_a$  values,  $G_{GJ}$  showed a systematic, yet relatively small change. When I compared the  $G_{GJ}$  estimates obtained with an  $R_a$  of 92  $\Omega\cdot\text{cm}$  (mean of the five soma-dendritically recorded GoCs; Figure 5.2.5E) versus 40  $\Omega\cdot\text{cm}$  (average  $R_a$  value of these cells without one outlier cell), only a 34% reduction in  $G_{GJ}$  was found (Figure 5.2.6E, red and green symbols, respectively).

### **5.2.5 Factors contributing to the variability in the strength of electrical coupling between cerebellar GoCs**

Data from Vervaeke et al., 2010 and our present study establish that the number (1–9, CV = 0.74) and size (0.009–0.065  $\mu\text{m}^2$ , CV = 0.68) of GJs, as well as their dendritic locations (9–152  $\mu\text{m}$ , CV = 0.57) are highly variable in electrically coupled GoCs. To estimate the relative contributions of these factors to the variability in the CC, I modelled GoC pairs, keeping their passive electrical parameters constant (Figure 5.2.7). First, I randomly selected a distance from the EM identified GJ distances ( $51.3 \pm 29 \mu\text{m}$ ,  $n = 58$  distances from 29 GJs in 8 GoC pairs; Vervaeke et al., 2010 and our present study) and placed a GJ with a 1 nS conductance into a randomly selected dendrite of a GoC at this distance. The CC was then measured in both directions and the simulation was repeated ten times for each of the four GoC pairs, resulting in a mean coefficient of variation (CV) of the CC of  $0.12 \pm 0.03$  ( $n = 8$ ; Figure 5.2.7A). Next, I tested the variability in CC due to different number of GJs between GoC pairs. The number of GJs between the eight EM analysed GoC pairs range from one to nine, with a mean of  $3.6 \pm 2.7$  (Vervaeke et al., 2010 and our present study). In these simulations, I placed different number of GJs (all with a  $G_{GJ}$  of 1 nS) at  $\sim 50 \mu\text{m}$  distance from the cell bodies of both neurons and calculated the CC for each pair. The mean CV of the CC was  $0.56 \pm 0.03$  ( $n = 8$ ; Figure 5.2.7B). Finally, I tested how the variability in  $G_{GJ}$

affects variations in the CC. Here, I placed four GJs (rounded from the mean GJ number of the eight EM analysed GoC pair from Vervaeke et al., 2010 and our present study) at  $\sim 50 \mu\text{m}$  distance from the somata on random selected dendrites (one dendrite on GJ) and randomly selected four  $G_{GJ}$  values from a population that was created from the distribution of GJ sizes. The mean GJ size distribution was normalized to the mean  $G_{GJ}$ , resulting in a distribution of  $G_{GJ}$ s that had a shape and variance of the distribution of the GJ areas with a mean of 0.94 nS. Ten repetitions of each simulation resulted in a mean CV of the CC of  $0.24 \pm 0.10$  ( $n = 8$ ; Figure 5.2.7C). Assuming that these three parameters are independent,  $CV^2$  should add linearly, allowing calculation of their contributions to the total variation in the CC. Calculating the relative contributions of the  $CV^2$  due to the different dendritic locations, numbers and sizes of GJs resulted in 4%, 81% and 15% contributions, respectively.



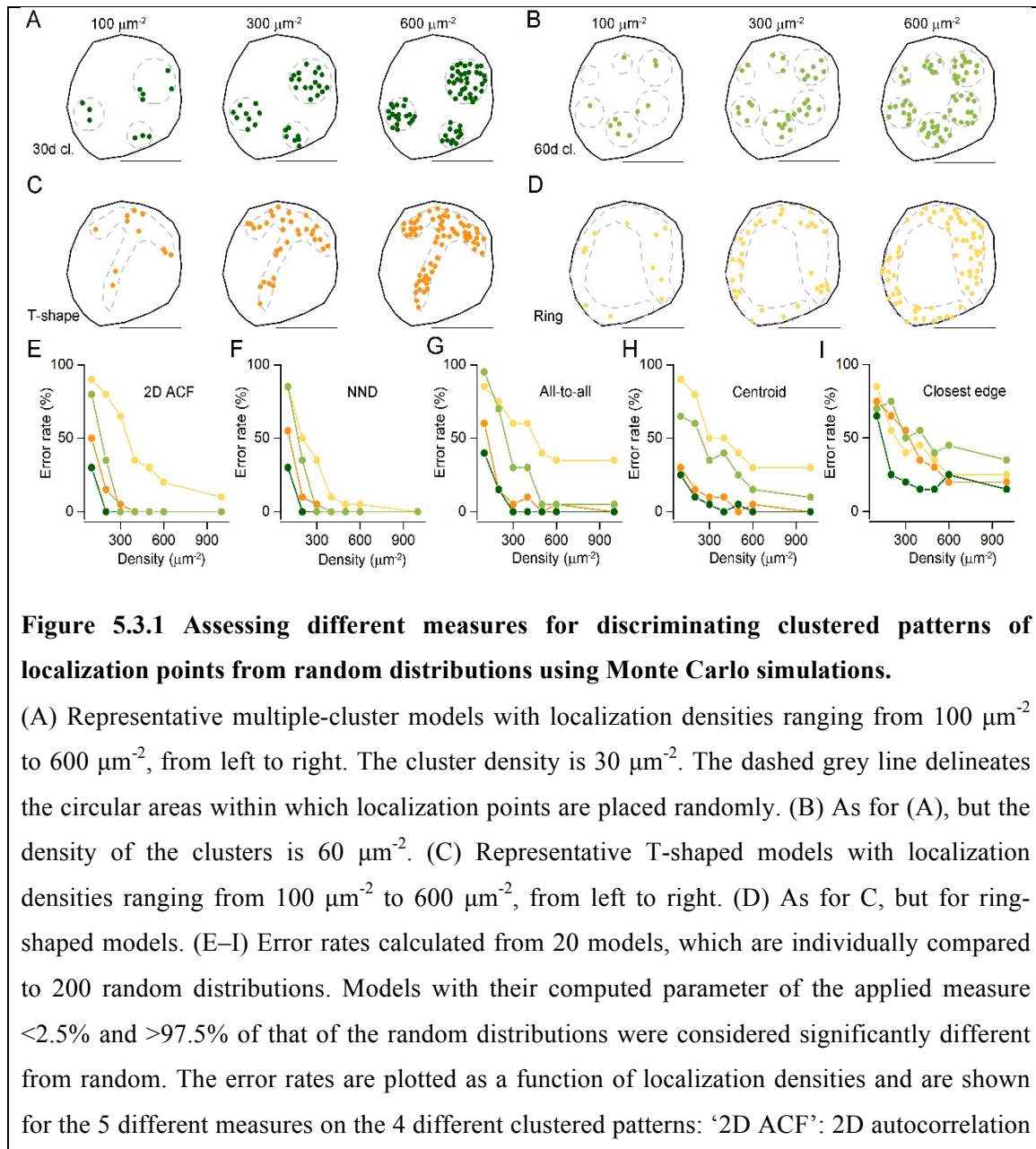
## 5.3 Objective quantification of nanoscale protein distribution patterns

### 5.3.1 Comparing different measures for distinguishing clustered patterns from random distributions

The nanoscale organizational principles of proteins in small subcellular compartments (e.g. AZ or postsynaptic density (PSD)) of neurons are of major interest of synaptic neuroscience. It has previously been shown that the distribution of voltage-gated  $\text{Ca}^{2+}$  channels (VGCC) compared to  $\text{Ca}^{2+}$  sensors substantially influences the probability of vesicular release ( $P_r$ ; reviewed by Eggermann et al., 2012). It has also been demonstrated that the Cav2.1 subunit of VGCCs are not randomly distributed within hippocampal (Althof et al., 2015; Holderith et al., 2012) and cerebellar (Indriati et al., 2013; Baur et al., 2015) synapses and subtle alterations in their sub-AZ localizations is sufficient to induce robust changes in synaptic transmission (Grauel et al., 2016). Similarly, in inhibitory synapses, nanoscale reorganization of gephyrin is a determinant of GABAergic synaptic potentiation (Pennacchietti et al., 2017). It is therefore of great importance to quantify the distribution (whether it is random, clustered or uniform) of synaptic proteins in an objective manner. These observations prompted me to search for appropriate metrics for such purposes.

To this end, I started to investigate the efficacy of five different measures in distinguishing clustered patterns of localization points from random distributions. Because many proteins have apparently clustered distributions in the PSD or the AZ (Althof et al., 2015; Tang et al., 2016), I generated clustered distributions of localization points at two different cluster densities ( $30 \mu\text{m}^{-2}$ : Figure 5.3.1A; and  $60 \mu\text{m}^{-2}$ : Figure 5.3.1B) by randomly placing circular areas (randomly selected radii within the range of 25–75 nm) within structure delineating polygons (SDPs) and randomly distributing the localization points within these circular areas (referred to as ‘multiple-cluster’ hereafter). With a mean SDP area of  $\sim 0.1 \mu\text{m}^2$ , these cluster densities resulted in an average of 3 or 6 clusters per SDPs. Visual inspections of hundreds of electron micrographs of presynaptic AZs immunolabelled for VGCCs or AZ-associated proteins revealed many complex labelling patterns, some of which looked like the letter T or a ring. To mimic such patterns, T- (Figure 5.3.1C) and ring-shaped (Figure 5.3.1D) areas

were drawn within the SDPs (by Dr Tekla Kirizs) and localization points were distributed within these areas at different densities. In all four cases, twenty SDPs with somewhat different shapes and sizes were used (mimicking variability of synapses), for which the overall density of localization points (densities are calculated for the whole SDP areas) were varied from  $100 \mu\text{m}^{-2}$  to  $600 \mu\text{m}^{-2}$ , with an increment of  $100 \mu\text{m}^{-2}$ , and  $1000 \mu\text{m}^{-2}$ , covering the range of immunogold densities for synaptic proteins as visualized with SDS-digested freeze-fracture replica immunolabeling (SDS-FRL; performed by Dr. Tekla Kirizs).





function (E); ‘NND’: nearest neighbour distances (F), ‘all-to-all’: distance of all localization points to all other localization points (G); ‘centroid’: distance of each point from the center of mass of the localization points (H); ‘closest edge’: distance of each point from the closest edge of the structure delineating polygon (SDP, I). Scale bars represent 200 nm in (A–D).

For each of the 560 models (4 patterns, 20 SDPs each, 7 different localization point densities), I performed Monte Carlo simulations by creating 200 corresponding randomizations of localization points and computed five different measures at the level of individual SDPs. Spatial autocorrelation function ( $g(r)$ ; Figure 5.3.1E; Veatch et al., 2012) quantifies the probability of finding additional localization points at a certain radius ( $r$ ) from a given localization point.  $g(r)$  values close to 1 indicate random distribution of points, (see Methods and Tang et al., 2016; Veatch et al., 2012; Figure 5.3.2). Since the shapes of the AZs are highly variable, I did not use absolute values of the  $g(r)$  functions to determine the underlying distribution of the point pattern, because randoms can still have a different value than 1 (see Methods). To this end, I compared each population of models to their corresponding randomizations to determine whether they are clustered or not (i.e. their mean  $g(r)$  ( $\overline{g(r)}$ ) values are higher than that of the randoms).

Four distance-based measures were also probed: nearest neighbour distance (‘NND’, Figure 5.3.1F), all-to-all distances (‘all-to-all’, Figure 5.3.1G), the distance of each point from the centre of gravity of the point pattern (‘centroid’, Figure 5.3.1H) and the distance of each point from the closest edge of the SDP (‘closest edge’, Figure 5.3.1I). The proportion of the 20 SDPs not identified as different from random was then calculated (defined as the error rate; see Methods and Figure 5.3.1). From these five measures, ACF and NND outperformed the others, resulting in an error rate of 0% at all localization point densities above  $300 \mu\text{m}^{-2}$  in case of the multiple clusters. Their performance was also remarkably good for the T- and ring-shaped patterns above the localization point density of  $400 \mu\text{m}^{-2}$ . Taken together, these data demonstrate that both ACF and NND measures are ideal for distinguishing between random and clustered patterns at the level of individual SDP.

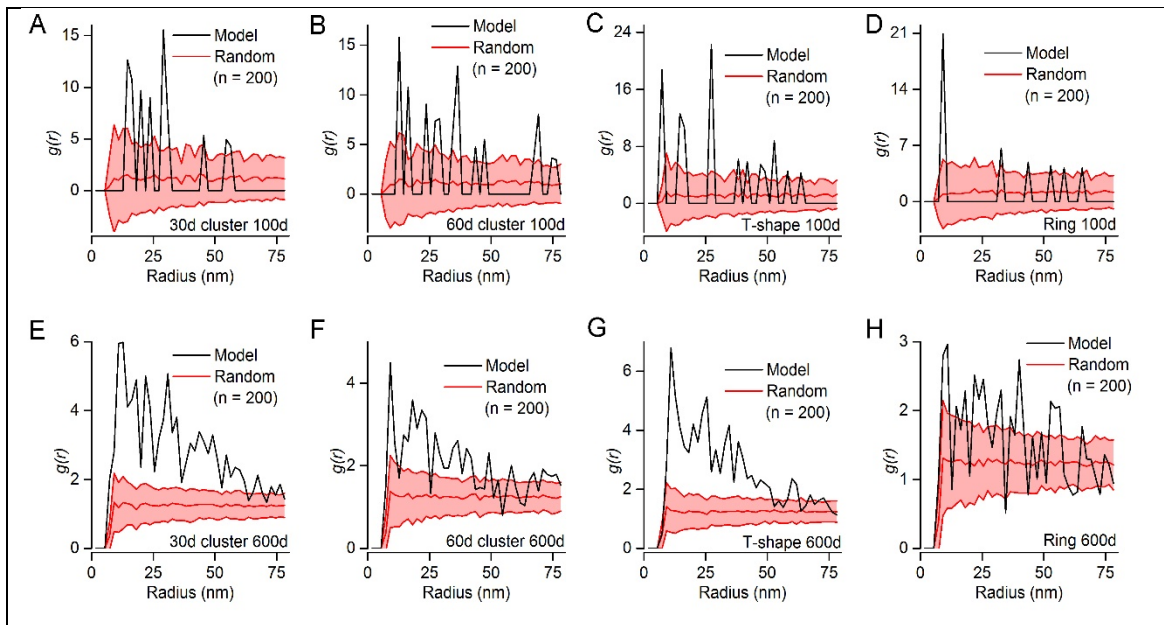


**Figure 5.3.2  $g(r)$  functions of individual models presented in Figure 1 and that of their corresponding random distributions ( $n = 200$ ).**

(A, B) Multiple-cluster models with a localization point density of  $100 \mu\text{m}^{-2}$  and cluster densities of  $30 \mu\text{m}^{-2}$  (A) and  $60 \mu\text{m}^{-2}$  (B). (C, D) T-shaped (C) and ring-shaped (D) models with a localization density of  $100 \mu\text{m}^{-2}$ . (E–H) Same as in A–D, but with a localization point density of  $600 \mu\text{m}^{-2}$ . At the localization point density of  $100 \mu\text{m}^{-2}$  (A–D) the  $g(r)$  function often drops back to zero (i.e. the probability of finding another localization point at such distance is zero) with high intermittent peaks. In contrast, the  $g(r)$  function of models with higher localization densities (e.g.  $600 \mu\text{m}^{-2}$ ; E–H) shows smaller, but more frequent peaks. In all cases, the average  $g(r)$  functions of random distributions are around one. Data of the random distributions are presented as mean  $\pm$  SD.

I also performed population-wise comparisons of the simulated datasets with the corresponding random distributions (see Methods) and found highly significant differences ( $p < 0.001$ , Kruskal-Wallis test followed by Mann-Whitney *U post hoc* test with Bonferroni-corrected  $p$  values) between the  $\overline{g(r)}$  and mean NNDs ( $\overline{\text{NND}}$ ) of the simulated data and that of the 200 random distributions even at the lowest tested localization point density of  $100 \mu\text{m}^{-2}$  (Figure 5.3.3 and Table 5.3.1). I found that population-wise comparisons are more powerful in detecting differences at low localization point densities than individual SDP level analysis.

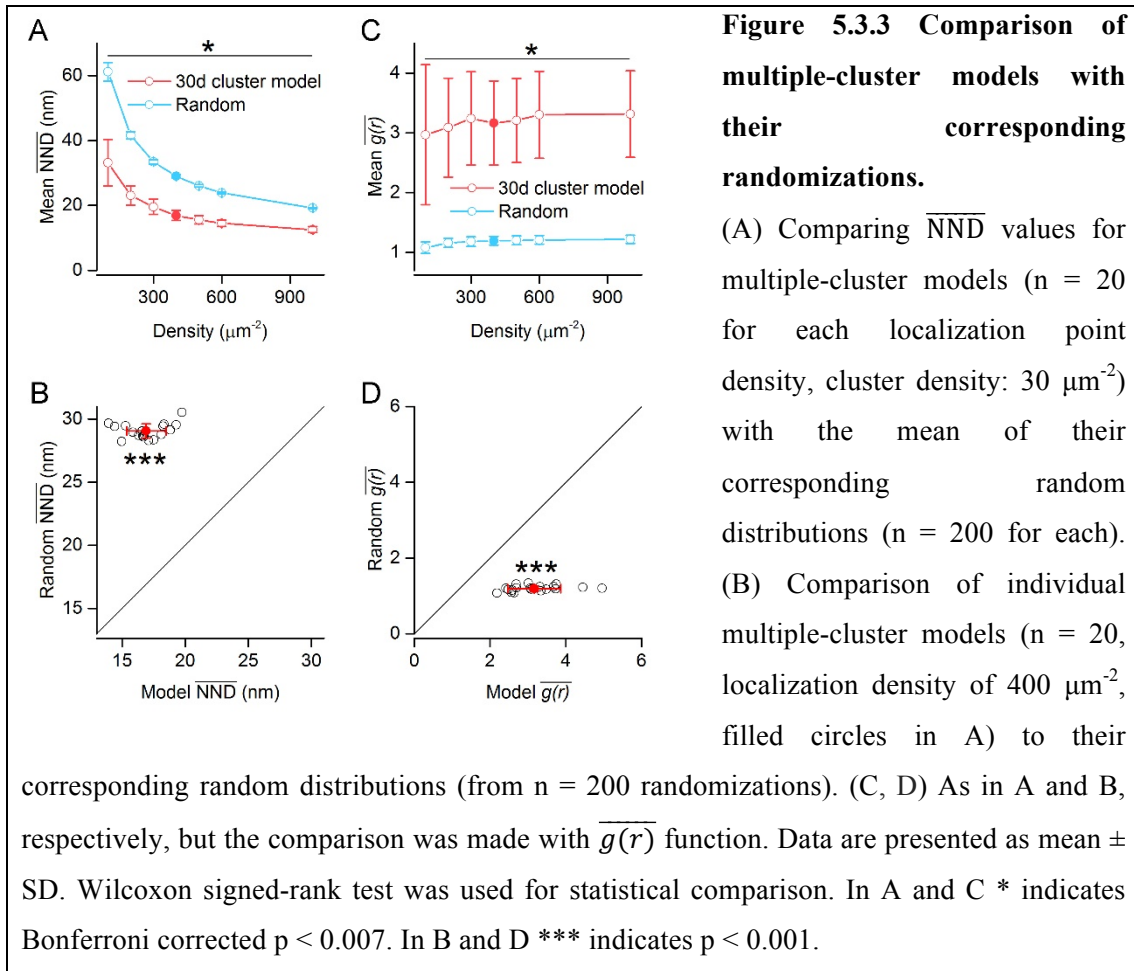


**Table S1. Population level statistical comparisons of simulated data with random distributions.**

Kruskal-Wallis test (5 independent groups) was used to test for significant differences between random and clustered distributions in case of the seven densities and five measures. In case of  $p < 0.05$  (shown with bold), *post hoc* Mann-Whitney *U* test was applied to compare the four clustered distributions to the random distribution. Red indicates Bonferroni corrected  $p < 0.0125$ . (Continued on next page.)

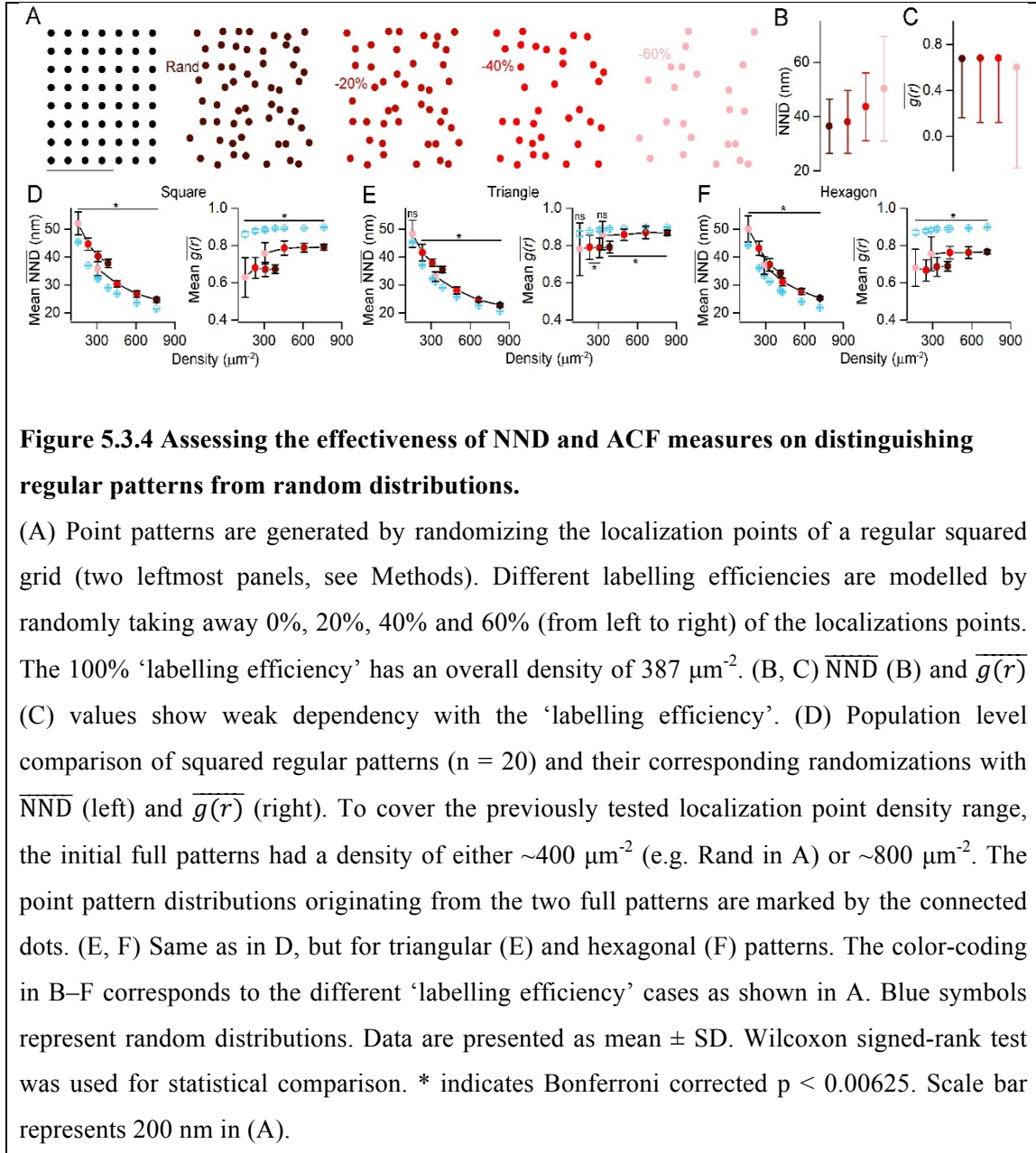
	Density ( $\mu\text{m}^{-2}$ )	Kruskal-Wallis test p values	Mann-Whitney <i>U</i> test p values			
			30d cl.	60d cl.	Ring	T-shape
2D ACF	100	<b>0.000000002</b>	0.0000003	0.0012300	0.3104000	0.0000086
	200	<b>0.000000000</b>	0.0000001	0.0000001	0.0025600	0.0000001
	300	<b>0.000000000</b>	0.0000001	0.0000001	0.0000059	0.0000001
	400	<b>0.000000000</b>	0.0000001	0.0000001	0.0000012	0.0000001
	500	<b>0.000000000</b>	0.0000001	0.0000001	0.0000021	0.0000001
	600	<b>0.000000000</b>	0.0000001	0.0000001	0.0000005	0.0000001
	1000	<b>0.000000238</b>	0.0000001	0.0000001	0.0000003	0.0000001
NND	100	<b>0.000000001</b>	0.0000001	0.0002469	0.0029200	0.0000097
	200	<b>0.000000000</b>	0.0000001	0.0000001	0.0000003	0.0000001
	300	<b>0.000000062</b>	0.0000001	0.0000001	0.0000001	0.0000001
	400	<b>0.000000000</b>	0.0000001	0.0000001	0.0000001	0.0000001
	500	<b>0.000000000</b>	0.0000001	0.0000001	0.0000001	0.0000001
	600	<b>0.000000000</b>	0.0000001	0.0000001	0.0000001	0.0000001
	1000	<b>0.000000000</b>	0.0000001	0.0000001	0.0000001	0.0000001
All-to-all	100	<b>0.000000024</b>	0.0000230	0.0083500	0.0858500	0.0001037
	200	<b>0.000000002</b>	0.0000204	0.0123400	0.1404200	0.0000059
	300	<b>0.000000002</b>	0.0000170	0.0123400	0.1135500	0.0000067
	400	<b>0.000000003</b>	0.0000230	0.0192900	0.2976800	0.0000052
	500	<b>0.000000002</b>	0.0000181	0.0105800	0.2732900	0.0000076
	600	<b>0.000000006</b>	0.0000204	0.0143600	0.3234800	0.0000097
	1000	<b>0.000000001</b>	0.0000141	0.0128200	0.3234800	0.0000045
Centroid	100	<b>0.000000001</b>	0.0000008	0.0000525	0.7149800	0.0000001
	200	<b>0.000000001</b>	0.0000104	0.0036400	0.2393200	0.0000016
	300	<b>0.000000001</b>	0.0000181	0.0071100	0.0909100	0.0000040
	400	<b>0.000000001</b>	0.0000230	0.0123400	0.1719300	0.0000035
	500	<b>0.000000001</b>	0.0000141	0.0090500	0.1264300	0.0000040
	600	<b>0.000000003</b>	0.0000181	0.0055600	0.2393200	0.0000035
	1000	<b>0.000000001</b>	0.0000181	0.0105800	0.1719300	0.0000031

Closest edge	100	<b>0.000052190</b>	<b>0.0047000</b>	0.0638900	<b>0.0060400</b>	0.1805800
	200	<b>0.000009368</b>	<b>0.0039700</b>	0.1332800	<b>0.0065600</b>	0.0810300
	300	<b>0.000006415</b>	<b>0.0047000</b>	0.1516500	<b>0.0033400</b>	0.0764300
	400	<b>0.000020388</b>	<b>0.0055600</b>	0.1636000	<b>0.0071100</b>	0.0531000
	500	<b>0.000014837</b>	<b>0.0051200</b>	0.0909100	<b>0.0105800</b>	0.0638900
	600	<b>0.000012603</b>	<b>0.0083500</b>	0.1198600	<b>0.0055600</b>	0.0438800
	1000	<b>0.000015151</b>	<b>0.0071100</b>	0.1135500	<b>0.0080200</b>	0.0294400

### 5.3.2 Performance of ACF and NND measures on uniform patterns

ACF and NND seem to be the most powerful measures to differentiate between clustered patterns and random distributions at both single SDP and population levels. Next, I tested how these measures perform when uniform patterns need to be distinguished from random distributions (Figure 5.3.4). I started by simulating one of the most basic uniform patterns, where the localization points are generated by randomizing the location of the nodes of a square grid with a 2D Gaussian having a covariance matrix of  $[(12^2, 0) (0, 12^2)]$  (see Methods, Figure 5.3.4A). Motivated by the fact that in immunoreactions, the labelling efficiency is rarely 100%, I tested the metrics on uniform patterns from which 0%, 20%, 40% or 60% of the localizations points were randomly removed (Figure 5.3.4A;  $n = 20$  for each ‘labelling efficiency’) and the  $\overline{\text{NND}}$  (Figure 5.3.4B) and  $\overline{g(r)}$  (Figure 5.3.4C) values were then computed. My results revealed that the  $\overline{\text{NND}}$  and  $\overline{g(r)}$  values were not too sensitive to decreasing the ‘labelling efficiency’ (full pattern:  $\overline{\text{NND}} = 36.5$  nm, -60%:  $\overline{\text{NND}} = 50.3$  nm, Figure 5.3.4B; full pattern:  $\overline{g(r)} = 0.68$ , -60%:  $\overline{g(r)} = 0.60$ , Figure 5.3.4C). Population-level comparison showed that  $\overline{\text{NND}}$  values of the uniform patterns are significantly larger than those obtained from random distributions (Figure 5.3.4D) for localization point densities ranging from  $\sim 100 \mu\text{m}^{-2}$  to  $\sim 800 \mu\text{m}^{-2}$ , irrespective whether 20%, 40% or 60% of the localization points were removed or not. I also obtained similar findings for triangular (Figure 5.3.4E) and hexagonal (Figure 5.3.4F) patterns. Furthermore, the  $\overline{\text{NND}}$  values of the clustered distributions are consistently smaller for the entire tested localization point density range than those of random distributions (Figures 5.3.3A and 5.3.3B). As described previously (Veatch et al., 2012; Tang et al., 2016) and shown in my simulations, the  $\overline{g(r)}$  values are close to 1 for random patterns and significantly

smaller than 1 for uniform patterns (Figure 5.3.4D–5.3.4F). For clustered patterns, the individual  $\overline{g(r)}$  values are substantially higher than 1 (Figure 5.3.3D), and when statistically analysed at the population level, they are significantly larger than those computed from random distributions (Figure 5.3.3C).



### 5.3.3 Performance evaluation of clustering algorithms

After analysing the localization point distribution patterns based on the methods detailed above, an obvious expectation is to investigate whether clusters could be identified or not in clustered distributions. Numerous clustering algorithms have been developed, out of which I applied four, in which the number of expected clusters does not need to be pre-defined: DBSCAN (DB; Ester et al., 1996), affinity propagation (AP; Frey and Dueck, 2007), mean shift (MS; Comaniciu and Meer, 2002) and a recently published algorithm based on Bayesian statistics (Bayesian clustering (BC); (Rubin-Delanchy et al., 2015)). In all of these methods, however, there are user-defined parameters; therefore I started by exploring the parameter space using the above described simulated clustered distributions (Figure 5.3.5). To evaluate the performance of these algorithms on the aforementioned dataset of multiple-cluster models, I calculated the adjusted Rand score (ARS; Hubert and Arabie, 1985), which computes similarity measures between two clusterings element-wise. ARS values close to 0 indicate random cluster assignments, whereas an ARS value of 1.0 indicates identical cluster assignments. The whole range of localization point densities of the models was explored, and the data at density of  $400 \mu\text{m}^{-2}$  is highlighted (Figure 5.3.5), because that represents the average density of Rim1/2 and Neurexin-1 $\alpha$  labelling (data from Dr Tekla Kiriz).

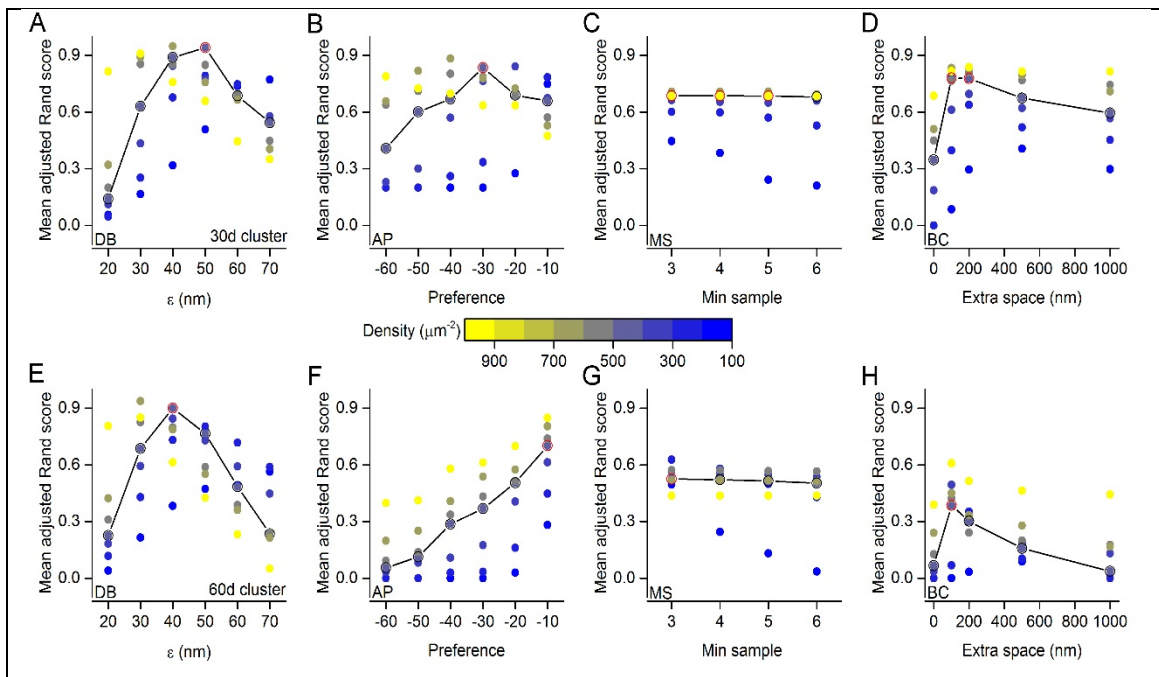


**Figure 5.3.5: Exploring user-defined variables of different clustering algorithms.**

(A) DBSCAN (DB): mean adjusted Rand scores (ARS) as a function of  $\epsilon$  (in nm), which is the maximum distance between two localization points to be assigned to the same cluster. Dots are color-coded based on the densities of the corresponding models (mean of  $n = 20$  SDPs). The line highlights the localization point density of  $400 \mu\text{m}^{-2}$ . Red open symbol indicates the maximum mean ARS (0.94) at  $\epsilon = 50$  nm. The cluster density is  $30 \mu\text{m}^{-2}$ . (B) Mean adjusted Rand scores as a function of the ‘preference’ value of the affinity propagation (AP) clustering algorithm. The maximum mean ARS (0.83) occurs at ‘preference’ value of  $-30$  (red open symbol). (C) The number of minimum localization points within a single cluster has relatively little effect on the maximum ARS (0.69 (3–5), 0.68 (6), red open symbols) using the mean shift (MS) clustering algorithm. Based on this finding, the same criterion ( $n = 3$  as minimum localization point) was used in case of the DB method as well. (D) For Bayesian clustering (BC), multiple user-defined parameters are available, however, we only explored the dependence of the mean ARS on the x-y spatial dimensions of the region of interest (ROI), since the authors of the original publication (Rubin-Delanchy et al., 2015) detailed the dependence of the number of detected clusters on parameters ‘ $\alpha$ ’ and ‘pbackground’ (see figure S11a–b of the original publication), which were set to 20 and 0.5, respectively in this study as suggested by Rubin-Delanchy et al. (2015). In the original paper, the analyzed ROIs were  $3000 * 3000$  nm. In our preparations, the ROIs were an order of magnitude smaller, so we systematically increased the ROI with additional distances of 0, 100, 200, 500 and 1000 nm outside the SDP borders to explore the dependence of ARS on the size of the ROI. We found that with an extra distance 100 and 200 nm, the mean ARS peaked at 0.78. 200 nm extra space was used for the clustering of experimental data for this algorithm. (E–H) Same as in A–D, with a cluster density of  $60 \mu\text{m}^{-2}$ . Note that the performance of the algorithms, excluding DB, drops substantially, when the cluster density in the models was doubled.

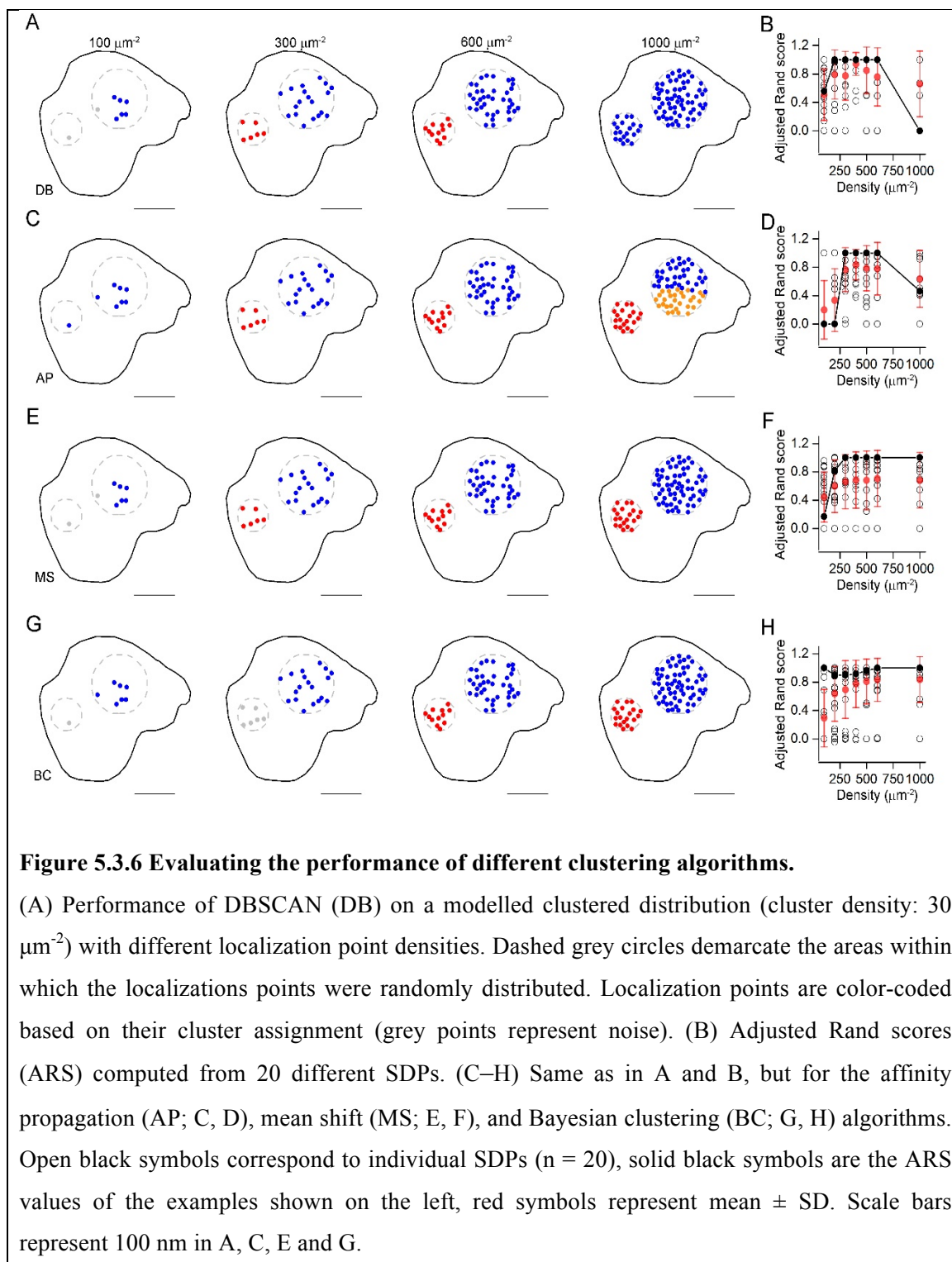
Using the MS method, the ARS has a flat relationship with the minimum number of localization points of the cluster (Figure 5.3.5C) and therefore I applied a minimum number of points of three not only for the MS, but also for the DB. In addition to the minimum number of localization points, DB has another user-dependent parameter:  $\epsilon$ , which is the maximal distance between two localization points to be considered in the same cluster. The  $\epsilon$  vs. ARS curve peaked at 50 nm with a value of 0.94 (indicating almost perfect performance) at the cluster density of  $30 \mu\text{m}^{-2}$  (Figure 5.3.5A), therefore I used an  $\epsilon$  of 50 nm throughout the study. AP produced the highest

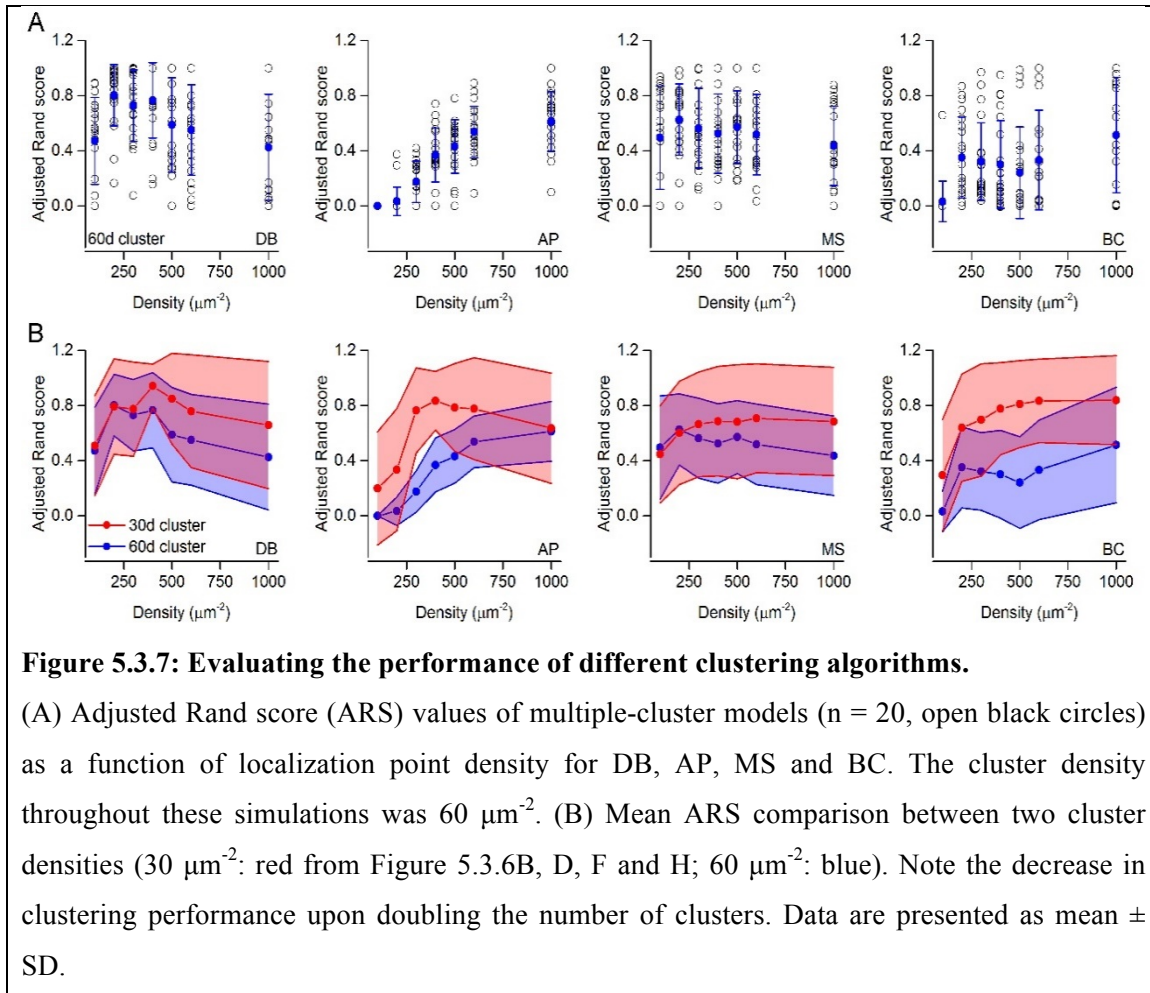


ARS value (0.83) at a ‘preference’ value of -30 (Figure 5.3.5B). For BC, the ARS heavily depends on the parameter ‘extra space’ peaking around 200 nm (Figure 5.3.5D), therefore I added 200 nm extra space to the edges of the SDPs. I also investigated these parameters in multiple-cluster models with a cluster density of  $60 \mu\text{m}^{-2}$  (Figure 5.3.5E–5.3.5H), and found that the performance of all algorithms, but DB, substantially dropped.

### 5.3.4 Clustering of localization point patterns

The four clustering algorithms with user-defined parameters producing highest ARSs were tested on simulated multiple-cluster distributions and their performances were compared first at a cluster density of  $30 \mu\text{m}^{-2}$  (Figure 5.3.6). Representative example of the same SDP with localization point densities ranging from  $100 \mu\text{m}^{-2}$  to  $1000 \mu\text{m}^{-2}$  is shown from left to right for DB, AP, MS and BC in Figure 5.3.6 with their corresponding ARS values (Figures 5.3.6B, 5.3.6D, 5.3.6F and 5.3.6H for DB, AP, MS and BC, respectively). In case of the representative example, for DB and AP, the performance of the clustering algorithms showed an inverted U shape; the ARS values were low at high and low localization point densities and peaked at localization point densities between 300 and  $600 \mu\text{m}^{-2}$  (Figure 5.3.6, second and third columns). The performance of MS peaked at  $300 \mu\text{m}^{-2}$  and remained high for higher localization point densities and the BC produced consistently high ARS throughout the whole density range tested (Figures 5.3.6F Figure 5.3.6H). I continued by repeating the same analysis on the artificial multiple-cluster models with a higher cluster density ( $60 \mu\text{m}^{-2}$ ; Figure 5.3.7), with the same user-defined parameters detailed above. Here, there were more clusters for the same SDP areas resulting in less cluster separation. As expected, the performance of most clustering algorithms dropped with the exception of DB and MS at low localization point densities ( $<300 \mu\text{m}^{-2}$ ; Figures 5.3.7A and 5.3.7B). The highest ARS value was obtained with DB at localization point densities of  $200 \mu\text{m}^{-2}$  ( $\sim 0.8$ ), but this was still considerably lower than that obtained with cluster density of  $30 \mu\text{m}^{-2}$ .





## 6 DISCUSSION

I have detailed the three main projects I have participated in during my Ph.D. studies, which are all related to a one- (Sections 5.1 and 5.2) or two-dimensional (Section 5.3) distribution of proteins at the subcellular (Sections 5.1 and 5.2) or sub-AZ (Section 5.3) levels. In Section 5.1, I aimed to develop a combined approach to determine subcellular ion channel distributions in CA1 PCs by performing *in vitro* dendritic patch-clamp recordings with pharmacological manipulations, morphological reconstruction of the recorded neurons and *in silico* multi-compartmental modelling.

At first, I tested the approach with an ion channel with previously described subcellular distribution, the HCN channels (Magee, 1998; Lőrincz et al., 2002; Golding et al., 2005). In individual cells, I was able to reproduce the formerly published results of HCN channel density along the apical dendrite of CA1 PCs (Magee, 1998) with remarkably accurate model fits, indicating that both the experimental paradigm, the quality of the experimental data and the model fitting strategy was well designed and suitable for such purposes. However, at the population level, I failed to reproduce experimental data with simultaneous model fitting approach, which could be the consequence the highly heterogeneous CA1 PC cell population. A higher number of recording locations on neurons and a further constrained fitting procedure could solve this issue, indicating that the proposed method is applicable to determine subcellular ion channel distributions on the neuronal surface.

Furthermore, in a joint effort with Dr Andrea Lőrincz and Dr Frederic Lanore, we sought out determine the functional properties of dendritic gap junctions in an electrically coupled cerebellar IN network formed by GoCs (Section 5.2). During this project, we discovered that the size of the GJs are independent of their dendritic location (corresponding to a uniform distribution over the dendritic tree as a function of distance from the soma), however, their strengths are highly variable. With a combination of *in vitro* dual soma-dendritic and paired somatic patch-clamp recordings, LM reconstruction of the recorded neurons combined with EM identification of the dendritic location of GJs, computational modelling determined that the main factor determining the highly variable coupling strength among these inhibitory INs is the number of GJs between a coupled GoC pair. In addition, we revealed that the mean conductance of a

GJ plaque mediated by Cx36 is 0.94 nS, dendritic GJs have 340 Cx36 channels on average, from which only 18% are open at a given time point assuming a single channel conductance of 16 pS. These results also shed light to the fact that voltage attenuation through the small diameter dendrites of GoCs is more pronounced than that occurring through GJs.

My third project aimed to find, test and implement pattern recognition algorithms in order to quantify nanoscale protein distributions (Section 5.3). With an extended set of Monte Carlo simulations covering the whole density range ( $100 - 1000 \mu\text{m}^{-2}$ ) of the experimental results of Dr Tekla Kirizis, it turned out that from the tested metrics, ACF and NND are the best performing ones at the individual synapse level. At the population level, these two statistics can efficiently distinguish between random, uniform and clustered patterns with a simple rule: if the mean NND of a given point pattern of a protein is smaller (or larger) than that of the corresponding random distributions, the sampled point pattern of the protein is clustered (or uniform). In case of the ACF, the opposite was true, i.e. if the mean ACF of a given point pattern of a protein is smaller (or larger) than that of the corresponding random distributions, the sampled point pattern of the protein is uniform (or clustered).

Once a point pattern is determined to be clustered, I applied a set of clustering algorithms (DBSCAN, affinity propagation, mean shift, and Bayesian clustering), which have a common property that the number of clusters is not a parameter has to be set *a priori*. After fine tuning their user-dependent parameters on the previously mentioned clustered models, I observed that DBSCAN was the most efficient algorithm, with on average 94% correct cluster assignments, determined by the adjusted Rand score of twenty simulated synapses at all tested localization point densities. These algorithms were then applied to experimental data, which is not part of the current dissertation, but results can be found in Szoboszlay et al., 2017. Finally yet importantly, all of the above listed algorithms were implemented in an open source Python software with a user-friendly GUI (<https://github.com/nusserlab/GoldExt>), which helps the potential naïve users to investigate their own protein of interest.

Determining the sub-AZ spatial distribution of different proteins could also help to develop and tweak computational models investigating synaptic functions such as

vesicle priming, vesicle docking and releasing, and the factors contributing to these events, which can provide experimentally testable predictions. Combining experimental and theoretical tools at multiple spatial scales can lead to exceptional insights to brain function. A simple example is how the nanoscale spatial rearrangement of protein molecules evoked by a biological stimulus leading to some kind of potentiation in a set of synapses could alter the cellular or even the network functions. It has been shown that GABAergic synaptic potentiation is altered by the nanoscale molecular reorganization of the inhibitory PSD (Pennacchietti et al., 2017). The mutual coenrichment of key proteins in the presynaptic AZ mediating vesicle priming and fusion has also been demonstrated (Tang et al., 2016), further supporting the significance of nanoscale protein reorganization. Determining the behaviour of a given protein at the nanoscale level to potentiating stimuli (e.g. high frequency spike train-evoked clustering) could then be easily incorporated into a multi-compartmental model of an *in vitro* recorded, synaptically connected neuron pair. Instead of modelling the change of synaptic connections with simply increasing or decreasing vesicular release probability, direct evidence of molecular reorganization could be linked to synaptic remodelling manifested at cellular level. With the recent development and availability of high-performance cluster computers, computational modelling at such precision can bridge the gap between molecular, cellular and network functions. Such detailed and experimentally constrained simulations could help to identify protein-protein interactions or protein reorganizational rules that promote e.g. memory formation, information processing or development of neurodegenerative characteristics within a reasonably short time.

## 7 CONCLUSIONS

To conclude, I would like to emphasize the unprecedented details and possibilities of the investigated phenomena provided by the combination of the applied techniques, i.e. *in vitro* physiological, pharmacological, anatomical and *in silico* computational tools. This led us to compute the mean  $G_{GJ}$  of a GJ plaque (0.94 nS), the average fraction of open Cx36 channels (18%) in a GJ plaque between cerebellar GoCs, as well as the fact that dendritic filtering is more substantial than that of the GJs in these electrically coupled cerebellar INs. We also determined that the main source of the large variability in the coupling strength is the different number of GJs occurring between GoCs.

The same technical arsenal allowed me to determine the subcellular HCN channel distribution along the main apical dendrite of hippocampal CA1 PCs, which is in accordance with previous electrophysiological (Magee, 1998) and anatomical (Lőrincz et al., 2002) results. However, at the population level, I failed to reproduce the experimental data with high quality model fits, such as those produced by fitting the data individually in each cell. This could be accounted for the pronounced diversity present in the hippocampal CA1 PC population. However, fine-tuning the fitting procedure or measuring from multiple locations from the same neuron (e.g. with voltage imaging) could improve the model quality population-wise.

Finally, with finding, implementing and testing pattern recognition algorithms, I was able to quantify nanoscale distribution of point patterns (i.e. proteins). With two simple measures, ACF and NND, both of which are computationally efficient, I could distinguish random, uniform and clustered point patterns from each other. These observations could lead to *in silico* modelling investigations of synaptic functions with the known organizational principles of synaptically relevant proteins (such as VGCCs,  $Ca^{2+}$  sensors,  $\alpha$ -amino-3-hydroxy-5-methyl-4-isoxazolepropionic acid (AMPA) receptors, etc.). Furthermore, these metrics, along with clustering algorithms to further dissect the underlying organizational principles of clustered protein distributions were implemented in an open source Python software to provide an integrated surface for proteins distribution analysis for the wider neuroscience community.

## 8 SUMMARY

I have been participated in three main projects during my Ph.D. studies. All three have a common property that a multidisciplinary approach was applied to tackle the questions. The first project aimed to develop a method with which the subcellular distribution of ion channels could be determined. It is based on *in vitro* dendritic patch-clamp recordings combined with pharmacological manipulations of the ion channels of interest, morphological reconstruction of the recorded neurons and *in silico* multi-compartmental modelling of the recorded membrane voltage responses. To validate the hypothesis, I tested this method against the subcellular distribution of HCN channels in the apical dendritic region of hippocampal CA1 pyramidal neurons. The results showed similar distribution as has previously been reported (Magee, 1998; Lőrincz et al., 2002), and the models with linearly increasing  $G_h$  were in good agreement with the experimental data.

During the second project, we determined the GJ plaque conductance (0.94 nS), open channel probability of a GJ plaque (18%) and the number of GJs between coupled GoC pairs as the main source of variability observed in coupling strength in a joint effort with Dr Andrea Lőrincz and Dr Frederic Lanore. We have also determined that signal attenuation is more severe along the dendrites than through GJs. These investigations implied the collective need of physiological, anatomical and computational tools as well.

A third project was about to find and test (on simulated datasets) pattern recognition algorithms that can objectively quantify the nanoscale distribution patterns of proteins. Two simple metrics, spatial autocorrelation function and the nearest neighbour distance distribution of the sample were able to distinguish between random, uniform and clustered patterns. Four clustering algorithms were also tested on clustered patterns to further investigate the organizational principles of the protein in question. I have implemented these algorithms in an open source Python software to provide an integrated surface for protein distribution analysis to a wider neuroscience community.



## 9 ÖSSZEFOGLALÓ

Doktori munkám során három kutatási programba kapcsolódtam be. Mindhárom megegyezett abban, hogy multidiszciplináris megközelítést követeltek meg a felvetődő kérdések megválaszolására. Elsőként egy módszert kívántam kifejleszteni, melynek alkalmazásával különböző ioncsatornák sejt felszíni eloszlását lehet meghatározni. *In vitro* túlélő patkány agyszeletben végzett, dendritikus patch-clamp elektrofiziológiai elvezetéseket kombinálva a megfelelő farmakológiai ágensek alkalmazásával, az elvezetett idegsejtek háromdimenziós morfológiai rekonstrukciójával majd a kísérleti membránválaszok számítógépes modellezésével sikerült hippocampális CA1 piramis sejtek HCN csatorna eloszlását meghatározni, amely összhangban volt korábban publikált eredményekkel (Magee, 1998; Lőrincz és mtsai., 2002). Egyedi sejtek esetén a modellek megfelelően leírták a kísérleti adatokat.

A második kutatási feladat során Dr Lőrincz Andrea és Dr Frederic Lanore munkatársaimmal sikerült meghatározunk kisagyi Golgi interneuronok közötti elektromos szinapszisok konduktanciáját (0.94 nS), ezen idegsejtek közötti elektromos szinapszisok csatornáinak nyitási valószínűségét (18%), valamint a Golgi sejtek közötti rendkívül változatos elektromos kapcsolati erősség elsődleges forrásaként azonosítottuk a kapcsolt idegsejtek között fellelhető elektromos szinapszisok számát. Az említett munkafolyamatok során élettani, anatómiai és számítógépes módszerek kombinált alkalmazásával nyertük eredményeinket.

A harmadik munkafázis során mintázatfelismerő algoritmusok kutatása és alkalmazása volt a feladatom abból a célból, hogy különböző szinaptikus fehérjék nanoskálájú szerveződését objektív módon tudjuk jellemezni. Két egyszerű eljárás, egy térbeli autokorrelációs függvény illetve a legközelebbi szomszédtól való távolság eloszlása képes volt különbséget tenni véletlenszerű, egyenletes és csoportosult ponteloszlások között. Négy csoportosító algoritmussal további betekintést nyerhetünk a csoportosult eloszlást mutató fehérjék szerveződési elveibe. Az összes kipróbált algoritmus egy nyílt forráskódú, Python alapú program formájában került megvalósításra.

## 10 BIBLIOGRAPHY

Alcami, P., and Marty, A. (2013). Estimating functional connectivity in an electrically coupled interneuron network. *Proc. Natl. Acad. Sci.* *110*, E4798–E4807.

Althof, D., Baehrens, D., Watanabe, M., Suzuki, N., Fakler, B., and Kulik, Á. (2015). Inhibitory and excitatory axon terminals share a common nano-architecture of their Cav2.1 (P/Q-type) Ca<sup>2+</sup> channels. *Front. Cell. Neurosci.* *9*.

Andersen, P., Bliss, T.V., and Skrede, K.K. (1971). Lamellar organization of hippocampal pathways. *Exp. Brain Res.* *13*, 222–238.

Atwood, H.L., and Karunanithi, S. (2002). Diversification of synaptic strength: presynaptic elements. *Nat. Rev. Neurosci.* *3*, nrn876.

Baddeley, A., and Turner, R. (2005). spatstat: An R Package for Analyzing Spatial Point Patterns. *J. Stat. Softw.* *12*, 42.

Basu, J., Zaremba, J.D., Cheung, S.K., Hitti, F.L., Zemelman, B.V., Losonczy, A., and Siegelbaum, S.A. (2016). Gating of hippocampal activity, plasticity, and memory by entorhinal cortex long-range inhibition. *Science* *351*, aaa5694-aaa5694.

Baur, D., Bornschein, G., Althof, D., Watanabe, M., Kulik, A., Eilers, J., and Schmidt, H. (2015). Developmental Tightening of Cerebellar Cortical Synaptic Influx-Release Coupling. *J. Neurosci.* *35*, 1858–1871.

Bennett, M.V. (1966). Physiology of electrotonic junctions. *Ann. N. Y. Acad. Sci.* *137*, 509–539.

Bittner, K.C., Andrasfalvy, B.K., and Magee, J.C. (2012). Ion Channel Gradients in the Apical Tuft Region of CA1 Pyramidal Neurons. *PLoS ONE* *7*, e46652.

Bower, J., and Beeman, D. (1994). *The Book of GENESIS: Exploring Realistic Neural Models with the GEneral NEural SIMulations System* (New York: Springer).

Buzsáki, G., and Moser, E.I. (2013). Memory, navigation and theta rhythm in the hippocampal-entorhinal system. *Nat. Neurosci.* *16*, 130–138.

Carnevale, N.T., and Hines, M.L. (2006). *The NEURON Book* (New York, NY, USA: Cambridge University Press).

Chevli, R., and Fitch, C.D. (1982). The antimalarial drug mefloquine binds to membrane phospholipids. *Antimicrob. Agents Chemother.* *21*, 581–586.

Comaniciu, D., and Meer, P. (2002). Mean shift: a robust approach toward feature space analysis. *IEEE Trans. Pattern Anal. Mach. Intell.* *24*, 603–619.

Cruikshank, S.J., Hopperstad, M., Younger, M., Connors, B.W., Spray, D.C., and Srinivas, M. (2004). Potent block of Cx36 and Cx50 gap junction channels by mefloquine. *Proc. Natl. Acad. Sci. U. S. A.* *101*, 12364–12369.

- Davie, J.T., Kole, M.H.P., Letzkus, J.J., Rancz, E.A., Spruston, N., Stuart, G.J., and Häusser, M. (2006). Dendritic patch-clamp recording. *Nat. Protoc.* *1*, 1235–1247.
- Dayan, P., and Abbott, L.F. (2001). *Theoretical neuroscience: computational and mathematical modeling of neural systems* (Cambridge, Mass: Massachusetts Institute of Technology Press), 203–206.
- Delvendahl, I., Straub, I., and Hallermann, S. (2015). Dendritic patch-clamp recordings from cerebellar granule cells demonstrate electrotonic compactness. *Front. Cell. Neurosci.* *9*.
- Devor, A., and Yarom, Y. (2002). Electrotonic coupling in the inferior olivary nucleus revealed by simultaneous double patch recordings. *J. Neurophysiol.* *87*, 3048–3058.
- Dobrunz, L.E., and Stevens, C.F. (1997). Heterogeneity of Release Probability, Facilitation, and Depletion at Central Synapses. *Neuron* *18*, 995–1008.
- Dugué, G.P., Brunel, N., Hakim, V., Schwartz, E., Chat, M., Lévesque, M., Courtemanche, R., Léna, C., and Dieudonné, S. (2009). Electrical Coupling Mediates Tunable Low-Frequency Oscillations and Resonance in the Cerebellar Golgi Cell Network. *Neuron* *61*, 126–139.
- Eggermann, E., Bucurenciu, I., Goswami, S.P., and Jonas, P. (2012). Nanodomain coupling between Ca<sup>2+</sup> channels and sensors of exocytosis at fast mammalian synapses. *Nat. Rev. Neurosci.* *13*, 7–21.
- Ester, M., Kriegel, H.-P., Sander, J., and Xu, X. (1996). A Density-based Algorithm for Discovering Clusters a Density-based Algorithm for Discovering Clusters in Large Spatial Databases with Noise. In *Proceedings of the Second International Conference on Knowledge Discovery and Data Mining*, (Portland, Oregon: AAAI Press), pp. 226–231.
- Fortier, P.A., and Bagna, M. (2006). Estimating conductances of dual-recorded neurons within a network of coupled cells. *J. Theor. Biol.* *240*, 501–510.
- Freund, T.F., and Buzsáki, G. (1996). Interneurons of the hippocampus. *Hippocampus* *6*, 347–470.
- Frey, B.J., and Dueck, D. (2007). Clustering by Passing Messages Between Data Points. *Science* *315*, 972–976.
- Gentet, L.J., Stuart, G.J., and Clements, J.D. (2000). Direct measurement of specific membrane capacitance in neurons. *Biophys. J.* *79*, 314–320.
- Gleeson, P., Steuber, V., and Silver, R.A. (2007). neuroConstruct: A Tool for Modeling Networks of Neurons in 3D Space. *Neuron* *54*, 219–235.
- Golding, N.L., Mickus, T.J., Katz, Y., Kath, W.L., and Spruston, N. (2005). Factors mediating powerful voltage attenuation along CA1 pyramidal neuron dendrites: Voltage attenuation in CA1 dendrites. *J. Physiol.* *568*, 69–82.

- Grael, M.K., Maglione, M., Reddy-Alla, S., Willmes, C.G., Brockmann, M.M., Trimbuch, T., Rosenmund, T., Pangalos, M., Vardar, G., Stumpf, A., et al. (2016). RIM-binding protein 2 regulates release probability by fine-tuning calcium channel localization at murine hippocampal synapses. *Proc. Natl. Acad. Sci. U. S. A.* *113*, 11615–11620.
- Guzman, S.J., Schlögl, A., Frotscher, M., and Jonas, P. (2016). Synaptic mechanisms of pattern completion in the hippocampal CA3 network. *Science* *353*, 1117–1123.
- Haas, J.S., Zavala, B., and Landisman, C.E. (2011). Activity-Dependent Long-Term Depression of Electrical Synapses. *Science* *334*, 389–393.
- Harnett, M.T., Makara, J.K., Spruston, N., Kath, W.L., and Magee, J.C. (2012). Synaptic amplification by dendritic spines enhances input cooperativity. *Nature* *491*, 599–602.
- Hoffman, D.A., Magee, J.C., Colbert, C.M., and Johnston, D. (1997). K<sup>+</sup> channel regulation of signal propagation in dendrites of hippocampal pyramidal neurons. *Nature* *387*, 869–875.
- Holderith, N., Lorincz, A., Katona, G., Rózsa, B., Kulik, A., Watanabe, M., and Nusser, Z. (2012). Release probability of hippocampal glutamatergic terminals scales with the size of the active zone. *Nat. Neurosci.* *15*, 988–997.
- Hu, H., and Jonas, P. (2014). A supercritical density of Na<sup>+</sup> channels ensures fast signaling in GABAergic interneuron axons. *Nat. Neurosci.* *17*, 686–693.
- Hubert, L., and Arabie, P. (1985). Comparing partitions. *J. Classif.* *2*, 193–218.
- Indriati, D.W., Kamasawa, N., Matsui, K., Meredith, A.L., Watanabe, M., and Shigemoto, R. (2013). Quantitative Localization of Cav2.1 (P/Q-Type) Voltage-Dependent Calcium Channels in Purkinje Cells: Somatodendritic Gradient and Distinct Somatic Co-clustering with Calcium-Activated Potassium Channels. *J. Neurosci.* *33*, 3668–3678.
- Izhikevich, E.M. (2010). *Dynamical systems in neuroscience: the geometry of excitability and bursting* (Cambridge, Mass.: MIT Press), 27–29.
- Jones, T.R., Kang, I., Wheeler, D.B., Lindquist, R.A., Papallo, A., Sabatini, D.M., Golland, P., and Carpenter, A.E. (2008). CellProfiler Analyst: data exploration and analysis software for complex image-based screens. *BMC Bioinformatics* *9*, 482.
- Kerti, K., Lorincz, A., and Nusser, Z. (2012). Unique somato-dendritic distribution pattern of Kv4.2 channels on hippocampal CA1 pyramidal cells: Somato-dendritic distribution of Kv4.2 on CA1 PCs. *Eur. J. Neurosci.* *35*, 66–75.
- Kirizis, T., Kerti-Szigeti, K., Lorincz, A., and Nusser, Z. (2014). Distinct axo-somato-dendritic distributions of three potassium channels in CA1 hippocampal pyramidal cells. *Eur. J. Neurosci.* *39*, 1771–1783.

Larkum, M.E., Nevian, T., Sandler, M., Polsky, A., and Schiller, J. (2009). Synaptic Integration in Tuft Dendrites of Layer 5 Pyramidal Neurons: A New Unifying Principle. *Science* 325, 756–760.

Levet, F., Hosy, E., Kechkar, A., Butler, C., Beghin, A., Choquet, D., and Sibarita, J.-B. (2015). SR-Tesseler: a method to segment and quantify localization-based super-resolution microscopy data. *Nat. Methods* 12, 1065–1071.

Li, Y., Majarian, T.D., Naik, A.W., Johnson, G.R., and Murphy, R.F. (2016). Point process models for localization and interdependence of punctate cellular structures: Spatial Point Process Models for Puncta Localization and Interdependence. *Cytometry A* 89, 633–643.

London, M., Meunier, C., and Segev, I. (1999). Signal Transfer in Passive Dendrites with Nonuniform Membrane Conductance. *J. Neurosci.* 19, 8219–8233.

Lőrincz, A., and Nusser, Z. (2010). Molecular Identity of Dendritic Voltage-Gated Sodium Channels. *Science* 328, 906–909.

Lőrincz, A., Notomi, T., Tamás, G., Shigemoto, R., and Nusser, Z. (2002). Polarized and compartment-dependent distribution of HCN1 in pyramidal cell dendrites. *Nat. Neurosci.* 5, 1185–1193.

Magee, J.C. (1998). Dendritic hyperpolarization-activated currents modify the integrative properties of hippocampal CA1 pyramidal neurons. *J. Neurosci. Off. J. Soc. Neurosci.* 18, 7613–7624.

Magee, J.C., and Johnston, D. (1995). Characterization of single voltage-gated Na<sup>+</sup> and Ca<sup>2+</sup> channels in apical dendrites of rat CA1 pyramidal neurons. *J. Physiol.* 487, 67–90.

Malik, R., and Johnston, D. (2017). Dendritic GIRK Channels Gate the Integration Window, Plateau Potentials, and Induction of Synaptic Plasticity in Dorsal But Not Ventral CA1 Neurons. *J. Neurosci.* 37, 3940–3955.

Mann-Metzer, P., and Yarom, Y. (1999). Electrotonic coupling interacts with intrinsic properties to generate synchronized activity in cerebellar networks of inhibitory interneurons. *J. Neurosci. Off. J. Soc. Neurosci.* 19, 3298–3306.

Maroso, M., Szabo, G.G., Kim, H.K., Alexander, A., Bui, A.D., Lee, S.-H., Lutz, B., and Soltesz, I. (2016). Cannabinoid Control of Learning and Memory through HCN Channels. *Neuron* 89, 1059–1073.

Megías, M., Emri, Z., Freund, T.F., and Gulyás, A.I. (2001). Total number and distribution of inhibitory and excitatory synapses on hippocampal CA1 pyramidal cells. *Neuroscience* 102, 527–540.

Nevian, T., Larkum, M.E., Polsky, A., and Schiller, J. (2007). Properties of basal dendrites of layer 5 pyramidal neurons: a direct patch-clamp recording study. *Nat. Neurosci.* 10, 206–214.

- Norenberg, A., Hu, H., Vida, I., Bartos, M., and Jonas, P. (2010). Distinct nonuniform cable properties optimize rapid and efficient activation of fast-spiking GABAergic interneurons. *Proc. Natl. Acad. Sci.* *107*, 894–899.
- O’Rourke, N.A., Weiler, N.C., Micheva, K.D., and Smith, S.J. (2012). Deep molecular diversity of mammalian synapses: why it matters and how to measure it. *Nat. Rev. Neurosci.* *13*, nrn3170.
- Pedregosa, F., Varoquaux, G., Gramfort, A., Michel, V., Thirion, B., Grisel, O., Blondel, M., Prettenhofer, P., Weiss, R., Dubourg, V., et al. (2011). Scikit-learn: Machine Learning in Python. *J Mach Learn Res* *12*, 2825–2830.
- Pennacchietti, F., Vascon, S., Nieuw, T., Rosillo, C., Das, S., Tyagarajan, S.K., Diaspro, A., Del Bue, A., Petrini, E.M., Barberis, A., et al. (2017). Nanoscale Molecular Reorganization of the Inhibitory Postsynaptic Density Is a Determinant of GABAergic Synaptic Potentiation. *J. Neurosci.* *37*, 1747–1756.
- Rall, W. (1959). Branching dendritic trees and motoneuron membrane resistivity. *Exp. Neurol.* *1*, 491–527.
- Rand, W.M. (1971). Objective Criteria for the Evaluation of Clustering Methods. *J. Am. Stat. Assoc.* *66*, 846.
- Roth, A., and Häusser, M. (2001). Compartmental models of rat cerebellar Purkinje cells based on simultaneous somatic and dendritic patch-clamp recordings. *J. Physiol.* *535*, 445–472.
- Rubin-Delanchy, P., Burn, G.L., Griffié, J., Williamson, D.J., Heard, N.A., Cope, A.P., and Owen, D.M. (2015). Bayesian cluster identification in single-molecule localization microscopy data. *Nat. Methods* *12*, 1072–1076.
- Segev, I. (1998). Sound grounds for computing dendrites. *Nature* *393*, 207–208.
- Shepherd, G.M.G. (2004). *The Synaptic Organization of the Brain* (Oxford, New York: Oxford University Press), 271–278, 455-463.
- Shepherd, G.M.G., and Harris, K.M. (1998). Three-Dimensional Structure and Composition of CA3→CA1 Axons in Rat Hippocampal Slices: Implications for Presynaptic Connectivity and Compartmentalization. *J. Neurosci.* *18*, 8300–8310.
- Shinoda, Y., Sugiuchi, Y., Futami, T., and Izawa, R. (1992). Axon collaterals of mossy fibers from the pontine nucleus in the cerebellar dentate nucleus. *J. Neurophysiol.* *67*, 547–560.
- Sotelo, C., and Llinás, R. (1972). Specialized membrane junctions between neurons in the vertebrate cerebellar cortex. *J. Cell Biol.* *53*, 271–289.
- Spruston, N. (2008). Pyramidal neurons: dendritic structure and synaptic integration. *Nat. Rev. Neurosci.* *9*, 206–221.

Stuart, G., and Spruston, N. (1998). Determinants of voltage attenuation in neocortical pyramidal neuron dendrites. *J. Neurosci. Off. J. Soc. Neurosci.* *18*, 3501–3510.

Sun, Q., Srinivas, K.V., Sotayo, A., and Siegelbaum, S.A. (2014). Dendritic Na(+) spikes enable cortical input to drive action potential output from hippocampal CA2 pyramidal neurons. *ELife* *3*.

Szoboszlay, M., Lőrincz, A., Lanore, F., Vervaeke, K., Silver, R.A., and Nusser, Z. (2016). Functional Properties of Dendritic Gap Junctions in Cerebellar Golgi Cells. *Neuron* *90*, 1043–1056.

Szoboszlay, M., Kirizs, T., and Nusser, Z. (2017). Objective quantification of nanoscale protein distributions. *Sci. Rep.* *7*, 15240.

Tamás, G., Buhl, E.H., Lőrincz, A., and Somogyi, P. (2000). Proximally targeted GABAergic synapses and gap junctions synchronize cortical interneurons. *Nat. Neurosci.* *3*, 366–371.

Tang, A.-H., Chen, H., Li, T.P., Metzbower, S.R., MacGillavry, H.D., and Blanpied, T.A. (2016). A trans-synaptic nanocolumn aligns neurotransmitter release to receptors. *Nature* *536*, 210–214.

Veatch, S.L., Machta, B.B., Shelby, S.A., Chiang, E.N., Holowka, D.A., and Baird, B.A. (2012). Correlation Functions Quantify Super-Resolution Images and Estimate Apparent Clustering Due to Over-Counting. *PLoS ONE* *7*, e31457.

Vervaeke, K., Lőrincz, A., Gleeson, P., Farinella, M., Nusser, Z., and Silver, R.A. (2010). Rapid Desynchronization of an Electrically Coupled Interneuron Network with Sparse Excitatory Synaptic Input. *Neuron* *67*, 435–451.

Vervaeke, K., Lorincz, A., Nusser, Z., and Silver, R.A. (2012). Gap Junctions Compensate for Sublinear Dendritic Integration in an Inhibitory Network. *Science* *335*, 1624–1628.

Williams, S.R., and Mitchell, S.J. (2008). Direct measurement of somatic voltage clamp errors in central neurons. *Nat. Neurosci.* *11*, 790–798.

## 11 BIBLIOGRAPHY OF CANDIDATE'S PUBLICATIONS

### Publications related to the Ph.D. dissertation

- Szoboszlay, M.\*, Lőrincz, A.\*, Lanore, F.\*, Vervaeke, K., Silver, R.A., and Nusser, Z. (2016). Functional Properties of Dendritic Gap Junctions in Cerebellar Golgi Cells. *Neuron* 90, 1043–1056.
- Szoboszlay, M.\*, Kirizs, T.\*, and Nusser, Z. (2017). Objective quantification of nanoscale protein distributions. *Sci. Rep.* 7, 15240.

\*equal contribution

### Other publications

- Oláh, V.J., and Szoboszlay, M. (2017). CA2 Pyramidal Neurons: Biophysically and Anatomically Predisposed Integrators of Cortical Sensory Information. *J. Neurosci. Off. J. Soc. Neurosci.* 37, 7564–7566.



## 12 ACKNOWLEDGEMENTS

First of all, I would like to thank to Zoltan Nusser for the opportunity to work in his lab and the support and mentorship he provided during my undergraduate and graduate years. I would also like to thank to Andrea Lőrincz, Frederic Lanore, Koen Vervaeke and Angus Silver for letting me work with them on the Golgi project and to Tekla Kirizs, with whom we worked on quantification of nanoscale protein distributions. The help of Noémi Holderith and Mark Eyre was invaluable during my electrophysiological experiments as well as the technical assistance of Dóra Bánsághiné Rónaszéki and Éva Dobai. I would also like to thank to the remainder of the Nusser lab for the pleasant atmosphere and for the Makara and Szabadics labs for the exciting scientific discussions at the joint journal clubs.

I am thankful to Szabolcs Káli, Gergő Orbán and Gábor Petheő for in the in-house and official reviews of my Ph.D. thesis, Miklós Geiszt, Csaba Barta and Zsolt Borhegyi for being members of the final examination committee and Attila Mócsai, Péter Barthó and Gergő Szanda for accepting my invitation as members of the reviewing committee of my Ph.D. dissertation.

I would also like to thank to József Bóna and Attila Villányi, who first showed me the beauty of science.

I cannot be grateful enough to my friends for being with me and tolerating me during the hard times as well.

Finally, I would like to express my gratitude to my family for the endless patience and support during my whole life enabling me to chase my dream.